SPECTROSCOPY OF ^{12}BE USING THE (^{7}LI, ^{7}BE) REACTION IN INVERSE KINEMATICS

By

Rhiannon Meharchand

A DISSERTATION

Submitted to
Michigan State University
in partial fulfillment of the requirements
for the degree of

DOCTOR OF PHILOSOPHY

Physics

2011

ABSTRACT

SPECTROSCOPY OF ^{12}BE USING THE (^{7}LI, ^{7}BE) REACTION IN INVERSE KINEMATICS

By

Rhiannon Meharchand

The quenching of the $N = 8$ shell gap has been under investigation for more than 40 years, yet there remains significant controversy over the extent of mixing between $0\hbar\omega$ and $2\hbar\omega$ configurations in ^{12}Be. Recent neutron knockout and transfer measurements have helped quantify $2\hbar\omega$ contributions to the ground and excited 0^+ states. The current study measures the $0\hbar\omega$ component of the 0^+ wavefunctions for the first time.

The Gamow-Teller strength (B(GT)) of transitions from the ground state of ^{12}B to the 0^+ states in ^{12}Be has been measured using the (^{7}Li, ^{7}Be) charge-exchange reaction in inverse kinematics. Since the ground state of ^{12}B is dominated by $0\hbar\omega$ configurations, Gamow-Teller (ΔL=0, ΔS=1) transitions to 0^+ states in ^{12}Be selectively probe the $0\hbar\omega$ component of the wavefunction.

The extracted B(GT) to the 0^+ states in ^{12}Be were compared with shell model calculations, performed using the code OXBASH and employing a modified WBP interaction in the $spsdpf$ model space. To reproduce the observed B(GT) distribution, a $0\hbar\omega$ admixture of 25.48±5.49% is required in the ground state of ^{12}Be, and a $0\hbar\omega$ admixture of 59.83±4.78% is required in the the 2.24 MeV 0^+ state. These results are compared with the wavefunctions extracted from neutron knockout and transfer measurements, and the theoretical predictions of Fortune and Sherr, Barker, and Romero-Redondo et $al.$

To Natalia - dream big, work hard, and you can do ANYTHING.

ACKNOWLEDGMENTS

building a phenomenal graduate program; and the recruitment committee, especially Micha Kilburn, and the non-official members who made MSU seem like the most fun place on earth (even in the dead of winter), David (Floyd) Miller, Brian Martin, and Davitt Driscoll.

I've been fortunate to be surrounded by people who made my time here easy. Debbie Barratt and the NSCL administrative assistants, who patiently answered all of my questions, and took care of travel, reimbursement, and other administrative hurdles so that I could focus on my studies and research. The NSCL operators and staff, who worked around the clock to get my thesis experiment up and running (twice). For that matter, everyone on Team 08017, who kept a close eye on the data and were patient with my micro-managing requests. John Yurkon, who spent hours teaching me how to roll targets, and Jon Bonofiglio, the best maintenance group leader/tiramisu maker/landlord ever. George Perdikakis and Dirk Weisshaar, for professional and personal mentoring. The entire charge-exchange group, Sam Austin, and Daniel Bazin, for weekly feedback and advice. The WaMPS 2009-2010 executive board, who put their time and heart into the organization and made everything run smoothly.

When things weren't so easy, it was the people at NSCL who made it all worth it. I have to thank the graduate students and postdocs who moved on too soon: Wes Hitt, for setting a great example; Jeremy Armstrong, for being easily persuadable; Arnau Rios, for Olè, London, and tomato bread; Carol Guess, for food, hiking, and all the advice; The Germans, for being great sports and great hosts; the lunch crew, for the best hour of the day; Phil Voss, for teaching me "my bad"; and Heather Crawford, an officemate for years but a friend for life. Also the graduate students who make it hard to move on: Andrew Ratkiewicz, for your loyal friendship and sympathetic ear; Shawna Valdez, for bringing your bright spirit to

TABLE OF CONTENTS

LIST OF TABLES

LIST OF FIGURES

Chapter 1

Introduction

1.1 The Atomic Nucleus

The idea that everything in our universe can be described in terms of fundamental particles was first developed by the Ancient Greeks and has persisted to the present day, evolving into its current form through advances in technology and the contributions of visionary scientists. Atoms, thought indivisible by the earliest scholars, are now known to be made up of negatively charged electrons orbiting a nucleus of positively charged protons and neutral neutrons, where the nucleons in the nucleus are made up of quarks. The field of nuclear physics is dedicated to understanding the structure and reactions of atomic nuclei, and in the past century nuclear physicists have made significant strides in this direction. More than 3000 different isotopes have been discovered, and models explaining the behavior of the most abundant, stable species have reached remarkable levels of accuracy. Yet there remains work to be done - particularly with respect to rare isotopes, which only exist for short periods of time before decaying into more stable species.

The two- and three-nucleon forces derived from stable isotope data have difficulty reproducing and predicting properties of rare isotopes, which indicates a lack of understanding of the fundamental forces at play in nuclear systems. Fortunately, a revolution in rare isotope research is underway: scientists are studying more exotic isotopes than ever before, producing data that can test and inform theoretical descriptions. The present study aims to improve the understanding of the evolution of nuclear structure away from stability, using a novel experimental technique to study the structure of the rare isotope Beryllium-12 (^{12}Be).

1.2   The Shell Model of Nuclear Structure

One of the foundations of chemistry is that the observed elemental properties can be well-described by a model in which the electrons of the atom are arranged in orbitals, or shells, around the atomic nucleus. In nuclear physics an analogous model is used to describe the structure and properties of isotopes - the Nuclear Shell Model. Developed in the mid-twentieth century, the Nuclear Shell Model helped nuclear scientists explain the experimental observations of the time - specifically, why it is more energetically expensive to remove a nucleon from some nuclei than others. To illustrate this property, Figure 1.1 (1.2) plots differences in in one-neutron (proton) separation energies ΔS_n (ΔS_p) as a function of neutron number. Maxima in ΔS correspond to closed-shell configurations, occuring in nuclei with 2, 8, 20, 28, 50, 82 or 126 neutrons and/or protons. These are referred to as "magic" or "semi-magic" nuclei. Other properties of "magic" nuclei are small ground-state quadrupole moments, and for even-even nuclei, relatively high-lying first 2^+ excited states and small electric quadrupole transition strengths B(E2, $2^+ \rightarrow 0^+$) [1]. The last two properties are shown in Figure 1.3.
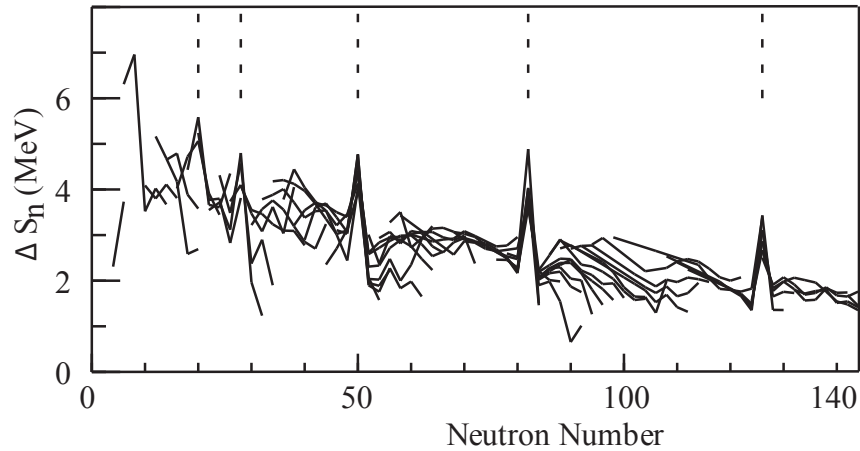
Figure 1.1: Differences in one-neutron separation energies as a function of neutron number. Solid lines connect nuclei with constant proton number. The magic numbers are indicated by dashed lines. Figure taken from Ref. [2].
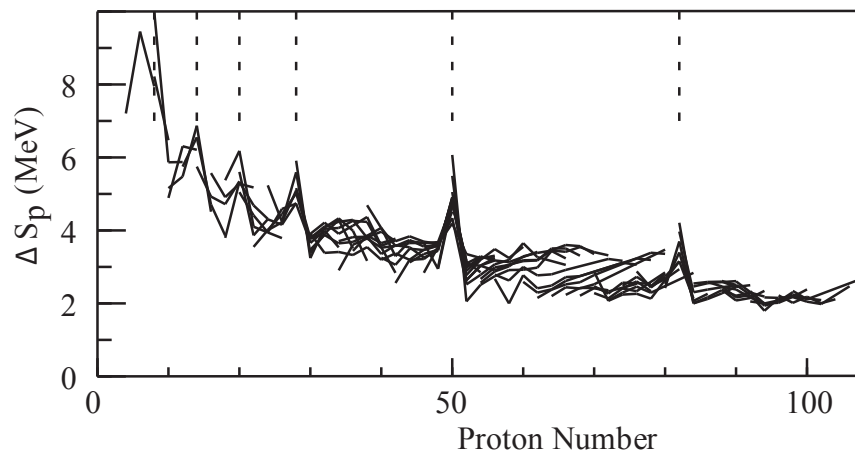
Figure 1.2: Differences in one-proton separation energies as a function of proton number. Solid lines connect nuclei with constant neutron number. The magic numbers are indicated by dashed lines. Figure taken from Ref. [2].

The simplest form of the Nuclear Shell Model is the Independent Particle Model, in which the behavior of one nucleon in the nucleus is modeled as a single particle inside an average potential, created by the mean field of all the other nucleons. A typical potential consists of the Coulomb potential, a central term, and a spin-orbit term

$$V = V_C(r) + V_O(r) + V_{SO}(r)\ \vec{l} \cdot \vec{s} \quad . \tag{1.1}$$

3
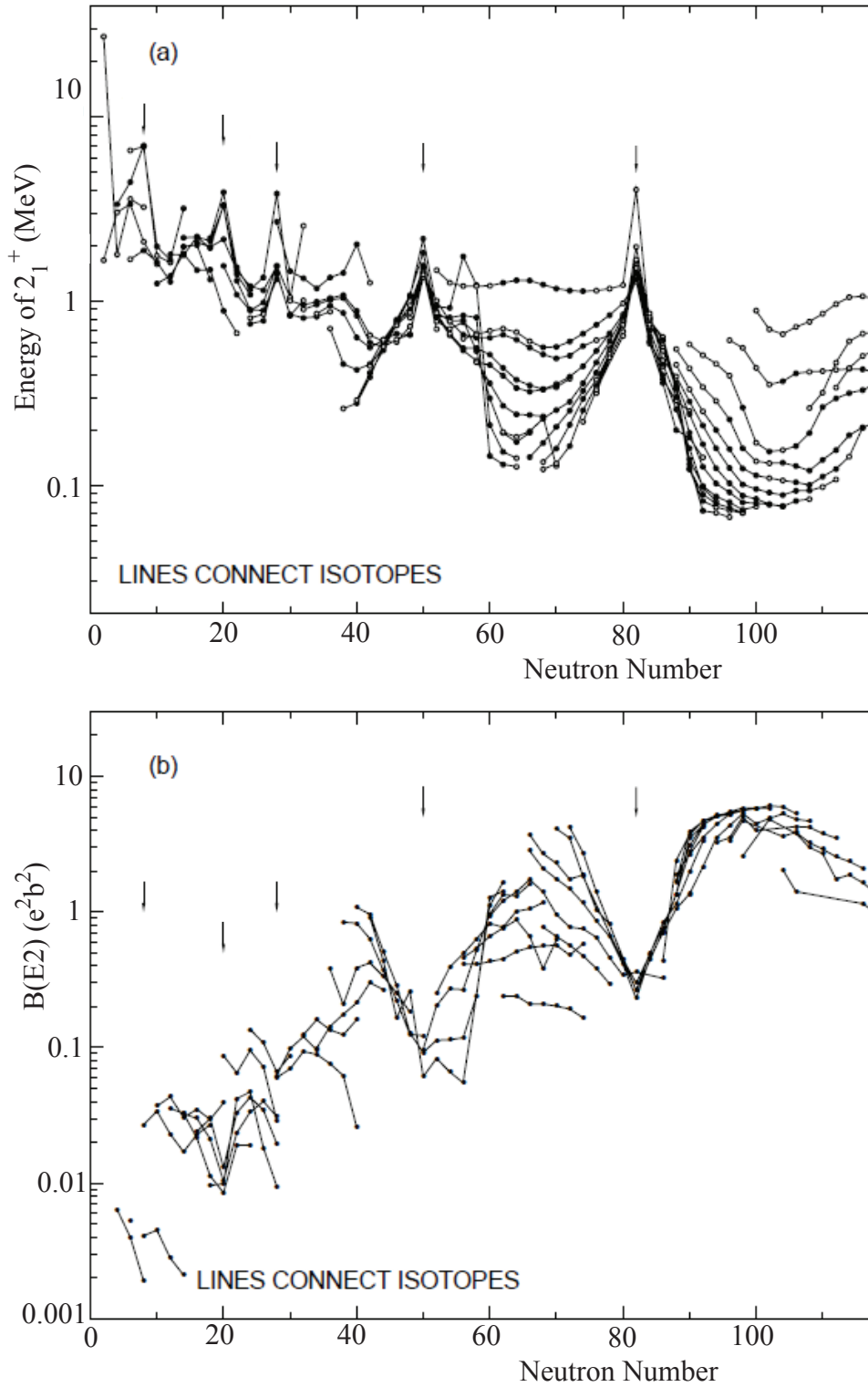
Figure 1.3: Energy of first 2^+ state and B(E2) strength, for even-even nuclei, as a function of neutron number. Arrows indicate magic numbers. Figure taken from Ref. [3].

The solution of the one-body Schrödinger equation using this potential has four good quantum numbers: the radial quantum number n_r, indicating the number of nodes in the wavefunction; the orbital angular momentum quantum number l; the total angular momentum quantum number j, corresponding to the addition of orbital angular momentum l and nucleon spin s; and the z-projection of the total angular momentum j_z [2].

Using the notation of Ref. [2], and looking at each of the terms in Equation 1.1.

- The Coulomb term has the form of a Coulomb potential for a sphere of charge Ze and radius R_C

$$
\begin{aligned}
V_C(r) &= \frac{Ze^2}{r} && \text{for } r \geq R_C \\
&= \frac{Ze^2}{R_C}\left[\frac{3}{2} - \frac{r^2}{2R_C^2}\right] && \text{for } r \leq R_C \ .
\end{aligned}
\tag{1.2}
$$

- The central term is most often one of two forms: a harmonic oscillator

$$
V_O(r) = \frac{1}{2}m\omega^2 r^2 \ ,
\tag{1.3}
$$

which has the advantage of being completely analytically solvable, and for which the energy eigenstates are characterized by the major quantum number $N = 2n_r + l$; or a Woods-Saxon potential

$$
\begin{aligned}
V_O(r) &= V_O f_O(r) \\
f_O(r) &= \frac{1}{1 + \exp[(r - R_0)/a_0]} \ ,
\end{aligned}
\tag{1.4}
$$

which has the advantage of better representing the short-ranged nature of the nuclear force, and removing the l-degeneracy present in the harmonic oscillator basis.

- The radial part of the spin-orbit term takes the form of a derivative of a Woods-Saxon potential

$$
V_{so}(r) = \frac{V_{so}}{r}\frac{df_{so}(r)}{dr} \ ,
\tag{1.5}
$$

where f_{SO} has the same form as f_O in Equation 1.4, but with diffuseness and radius a_{SO} and R_{SO}. The addition of the spin-orbit term removes all remaining degeneracies [4,5], and produces large differences in energy between single-particle orbitals for magic numbers of nucleons, shown in Figure 1.4.

In Equations 1.2 - 1.5, the radii are expressed as $R_i = r_i A^{1/3}$ and r_i is typically taken to be 1.25 fm.

The Independent Particle Model can predict many of the properties of nuclei with one nucleon more or less than a magic number. However, when several valence nucleons occupy orbits outside of a magic number "core" or when considering very light (no-core) nuclei, the problem becomes significantly more complex due to strong forces between valence nucleons. Modern shell model codes like OXBASH [6], NuShell [7], and NuShellX [8] account for valence nucleon interactions by solving the Schrödinger equation

$$H\Psi = E\Psi \tag{1.6}$$

as a matrix equation, diagonalizing the many-body Hamiltonian H. The diagonalization procedure is often performed in a reduced model space, since the dimensionality of H depends on the number of particles and orbits included in the calculation, which can be quite large for medium and heavy nuclei. Off-diagonal elements result in mixing of many-body configurations. While there is no exact expression for the nuclear Hamiltonian H, it can be conveniently written as a combination of single-particle energies (SPEs) and two-body matrix elements (TBMEs)

$$H = SPE + \langle \alpha\beta | V | \alpha\beta \rangle \ , \tag{1.7}$$

where α and β are single-particle states and V is an effective interaction obtained by fitting SPEs and TBMEs such that experimental observables are reproduced.

Figure 1.4: Neutron single-particle states in ^{208}Pb with three potential models, harmonic oscillator (left), Woods-Saxon without spin-orbit (middle) and Woods-Saxon with spin-orbit (right). The numbers in square brackets are the maximum number of neutrons in that each level can contain, the major quantum number $N = 2n + l$, the Woods Saxon is labeled by n, l and the Woods-Saxon with spin-orbit is labeled by $n, l, 2j$. Figure and caption taken exactly from [2].

Despite its many successes, the Nuclear Shell Model has difficulties predicting the properties of unstable nuclei. The experiment and result presented here will provide information about the $N = 8$ "semi-magic" nucleus ^{12}Be, shedding light on the evolution of shell structure in light, unstable systems.

1.3 Charge-Exchange Reactions

In a nuclear charge-exchange reaction, participating nuclei change proton number by one ($\Delta Z = \pm 1$) but keep their mass number constant ($\Delta A = 0$). These are isovector transitions, meaning there is a unit change of isospin ($\Delta T = 1$). Charge-exchange reactions can proceed with or without spin transfer ($\Delta S = 1$ or 0), and with any transfer of angular momentum (ΔL). The charge-exchange processes discussed here involve direct conversion of a proton into a neutron - or vice versa - via meson exchange (as opposed to indirect multi-nucleon exchange processes).

Charge-exchange reactions have long been used to study the spin-isospin response of nuclei (see e.g. Refs. [9, 10] and references therein). They are a particularly useful tool for measuring Gamow-Teller strengths (B(GT)), where a Gamow-Teller transition is characterized by no transfer of orbital angular momentum and a unit transfer of spin ($\Delta L = 0$, $\Delta S = 1$). The isovector spin-transfer operator for charge-exchange reactions is written as

$$O_{JM}^{\pm} = \sum_k r_k^{\Delta L} \left[Y_{\Delta L} \otimes \sigma_k \right]_M^J \tau_{\pm k} \ , \tag{1.8}$$

where σ refers to the nucleon spin operator, $Y_{\Delta L}$ to the spherical harmonics, and the cross symbol $\otimes$ denotes a Clebsh-Gordan product coupling to the total angular momentum J and absorbing all M dependence of the spherical harmonics. $\tau_{\pm}$ refers to the isospin rais-

ing/lowering operator, and the sum over k represents the sum over all nucleons in the nucleus. When $\Delta L = 0$, this operator is identical to the Gamow-Teller operator for β-decay

$$O(GT_\pm) = \sum_k \sigma_k \tau_{\pm k} \ .\tag{1.9}$$

In β-decay, the B(GT) is the square of the reduced matrix element involving the Gamow-Teller operator and connecting the initial i and final f states of the nucleus

$$B(GT_\pm) = \frac{|<f||O(GT_\pm)||i>|^2}{(2J_i + 1)} \ ,\tag{1.10}$$

where the matrix element has been reduced in orbital space following the convention of Ref. [2]. The B(GT) can be directly related to the β-decay partial half-life (t), historically written in terms of an ft-value

$$ft = \frac{C}{B(F) + (g_A/g_V)^2 B(GT)} \ ,\tag{1.11}$$

which incorporates a phase-space factor f. In Equation 1.11, C is a combination of fundamental constants constrained by super-allowed β-decays [11], and the ratio of the axial and vector coupling constants g_A/g_V is empirically determined by the decay of the neutron [12]. One major limitation of β-decay studies is that they are limited by the decay Q-value to a small excitation energy window, and as a result they are unable to extract the full B(GT) distribution. B(GT) distributions obtained in charge-exchange measurements are not subject to this limitation.

1.3.1 Proportionality Relationship

Although β decay is governed by the weak force and charge-exchange by the strong force, the operators for the two processes are similar, connecting the same final and initial states. A

phenomenological proportionality has been established relating the differential cross-section measured in charge-exchange reactions (at the limit of vanishing momentum transfer) and the Gamow-Teller strength:

$$\frac{d\sigma}{d\Omega}\bigg|_{q=0} = \hat{\sigma}B(GT) \ .$$

(1.12)

This proportionality was established with (p,n) reaction data and is described in detail in Ref. [13]. The unit cross-section $\hat{\sigma}$ can be parameterized using direct reaction theory into a kinematic term (K), a term describing distortion effects due to the mean field of the nuclei involved (N_D), and a term related to the effective nucleon-nucleon interaction $(J_{\sigma\tau})$

$$\hat{\sigma} = KN_D|J_{\sigma\tau}|^2 \ .$$

(1.13)

The last term consists of a direct (D) and exchange (E) component

$$J_{\sigma\tau} = J_D + J_E$$

(1.14)

where the exchange term is due to the antisymmetrization of target and projectile nucleons and typically interferes destructively, reducing the total cross-section (compared to calculations where only the direct component is considered) [13].

In most cases it is not necessary to rely on reaction theory to calculate the terms K, N_D, and $J_{\sigma\tau}$. For $(t,^3\text{He})$ and $(^3\text{He}, t)$ reactions, an empirical mass-dependent formula for the unit cross-section $\hat{\sigma}$ has been established [14]. For cases in which there are several Gamow-Teller transitions, the unit cross-section can be extracted locally and model-independently, by calibrating Equation 1.12 with a known B(GT) (i.e. from a β-decay measurement). The unit cross-section obtained from this calibration can be applied to all other Gamow-Teller transitions, providing a direct link between the differential cross-sections measured in charge-exchange experiments and B(GT)s of interest for nuclear structure.

The validity of Equation 1.12 relies on several approximations, described in detail in Ref [13]. These include:

- the Eikonal approximation, where collisions are assumed to occur at high beam energies and scattered particles follow straight-line trajectories, which greatly simplifies the distortion contribution to the unit cross-section; and

- the factorization of the cross section into K, N_D, $|J_{\sigma\tau}|$, and B(GT), meaning that the kinematic, distortion, interaction, and structure terms are independent.

In practical terms, for Equation 1.12 to hold, the linear momentum transfer q needs to be approximately equal to zero (validating the use of the Eikonal approximation), and the incident beam energy needs to be $\geq$80 MeV/u (to largely eliminate contributions from multi-step processes and to reduce the effect of distortion).

The proportionality between differential cross-section and B(GT) allows one to measure B(GT) distributions without the Q-value limitations of β-decay studies. Despite the fact that Equation 1.12 was derived for (p,n) charge-exchange probes, it appears to hold for composite probes as well, and as a result over the past quarter-century many other charge-exchange probes have been developed.

1.3.2   History of Charge-Exchange Probes

The first charge-exchange experiment took place in the late 1950s at the University of California Radiation Laboratory, where a low-energy proton beam was impinged upon deuterium gas [15]. Since then, (p,n) reaction studies have been carried out at many different laboratories, resulting in several significant achievements including: a deeper understanding of collective spin-isospin modes in nuclei [16–20]; development of a nucleon-nucleon inter-

action for use in Distorted Wave Born Approximation (DWBA) calculations [21–24]; and the derivation of the linear relationship between (p,n) cross-sections at forward angles and Gamow-Teller strengths [13, 25, 26].

As the usefulness of charge-exchange reactions became apparent, new probes were developed to excite other isospin modes and to achieve better energy resolution than (p,n) reactions (which could only reach energy resolutions of approximately 300 keV FWHM). At present, in the isospin-raising ($\Delta T_z = 1$) direction, probes include: $(t,{}^{3}\text{He})$, developed in the 1970s [27]; (n,p) and $({}^{7}\text{Li}, {}^{7}\text{Be})$, developed in the 1980s [28–30]; and $(d,{}^{2}\text{He})$, developed in the 1990s [31–33]. In the isospin-lowering ($\Delta T_z = -1$) direction, the $({}^{3}\text{He},t)$ probe was developed in the mid-1980s [34–36]. More recently, heavy-ion charge-exchange probes such as $({}^{12}\text{C}, {}^{12}\text{N})$ and $({}^{13}\text{C},{}^{13}\text{N})$ were developed, used primarily to investigate giant resonances [37–40].

Each charge-exchange probe has advantages and limitations. (p,n) and (n,p) probes benefit from a (relatively) simple nucleon-nucleus reaction mechanism, but yield significantly worse resolution than $({}^{3}\text{He},t)$ and $(t,{}^{3}\text{He})$ measurements. Composite probes can provide improved resolution (approximately a factor of 10), but the reaction mechanism is significantly more complicated and less experimental data is available. Perhaps most importantly, all probes mentioned here share one major limitation: until recently, charge-exchange studies using these probes were limited to transitions from stable nuclei - these probes could not be used to study rare isotopes.

The $({}^{7}\text{Li}, {}^{7}\text{Be})$ probe is the first $\Delta T_z = +1$ charge-exchange probe to be developed for use in inverse kinematics experiments at intermediate beam energies, expanding charge-exchange studies to rare isotopes. The first inverse kinematics charge-exchange experiment

utilizing a rare isotope beam took place at the National Superconducting Cyclotron Laboratory (NSCL) in 2002. In the experiment, a beam of ^{56}Ni was impinged upon a thick ^{7}Li target and the exciation energy spectrum of ^{56}Co was reconstructed from Doppler-corrected gamma rays. Unfortunately, this inaugural experiment was largely unsuccessful. In 2007, a second attempt was made, this time aimed at extracting the B(GT) distribution of ^{34}Si. The combination of a lighter projectile, much thinner target, and use of a high-resolution spectrometer to reconstruct the ^{34}Si excitation energy spectrum (rather than Doppler-corrected gamma rays) yielded success, demonstrating the feasibility of the (^{7}Li, ^{7}Be) reaction for inverse kinematics experiments [41].

1.3.3   (^{7}Li, ^{7}Be) Charge-Exchange in Inverse Kinematics

The (^{7}Li,^{7}Be) reaction has a long history of use in forward kinematics experiments [42–46]. As a result, at ^{7}Li energies of 65 MeV/u, the proportionality between B(GT) and cross-section at forward angles has been established at the ~20% level [46]. This is expected to improve at higher beam energies, due to a reduction of multi-step contributions and of the tensor-τ component of the effective nucleon-nucleon interaction [23] (see Section 3.4).

The (^{7}Li, ^{7}Be) probe is spin-selective; that is, it is possible to isolate spin-transfer ($\Delta S = 1$) events from all others. To illustrate how this works, Figure 1.5 shows the possible transitions from the ground state of ^{7}Li to states in ^{7}Be. If a transition is made to the ^{7}Be ground state, the reaction contains a mixture of spin-transfer and non-spin-transfer components ($\Delta S = 1$ and $\Delta S = 0$). If the transition is made into the ^{7}Be excited state at 429 keV, the reaction is purely $\Delta S = 1$ (for $\Delta L = 0$ transitions). This means one can isolate or "tag" the $\Delta S = 1$ charge-exchange reaction channel, by measuring the reaction ejectile in

4.57 MeV   7/2⁻

1587 keV   α+³He

429 keV   1/2⁻

ΔS=1

B(GT) =1.07   g.s.   γ   3/2⁻

g.s.   3/2⁻   ⁷Be

ΔS=0,1

⁷Li   B(GT)=1.2
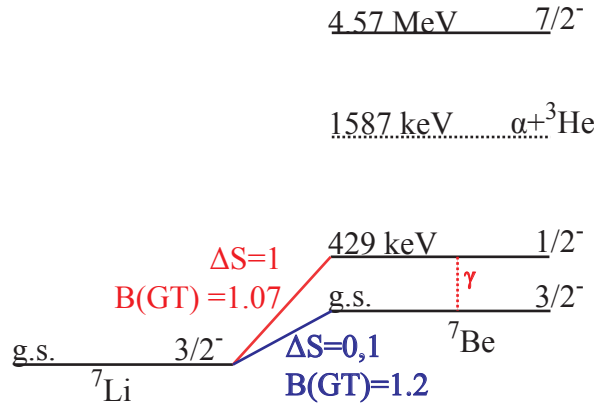
Figure 1.5: Transitions from the ground state of ^{7}Be to states in ^{7}Be. The particle decay threshold is indicated by the black dotted line, and the red dotted line refers to the de-excitation gamma-ray emitted from the 429 keV ^{7}Be excited state. For interpretation of the references to color in this and all other figures, the reader is referred to the electronic version of this dissertation.

coincidence with the 429 keV gamma ray emitted during the de-excitation of ^{7}Be. Events registering a reaction ejectile *and* a 429 keV ^{7}Be de-excitation gamma ray are referred to as "coincidence" events. Events that do not require a coincident 429 keV gamma ray are referred to as "singles" events, and could involve transitions into the ground or excited states of ^{7}Be.

In inverse kinematics experiments, coincidence data can be extremely useful for isolating charge-exchange events from those produced via other reaction channels. It can also provide better energy resolution than the singles data, because of an inherent 429 keV ambiguity in the singles data excitation energy reconstruction (depending on whether the ground or 429 keV state in ^{7}Be is populated). That said, the limited detection efficiency for gamma rays and the branching ratio to the 429 keV state make the overall count rate for coincidence data lower than for singles data, and since rare isotope beam rates are already significantly lower than those obtained in stable beam experiments, this additional reduction can be prohibitive.

14

Fortunately, in the current study, the Gamow-Teller transitions of interest in ^{12}Be are located at low excitation energies (less than 3 MeV), making it possible to distinguish singles events transitioning through the ground and 429 keV states in ^{7}Be from those transitioning through the 4.57 MeV (and higher) excited states. Although the transition through the ground state of ^{7}Be is associated with both $\Delta S = 1$ and $\Delta S = 0$, the magnitude of the $\Delta S = 0$ operator is small compared to that of the $\Delta S = 1$ operator at the beam energies under consideration here [23]. Additionally, the transitions of interest for the present study are from the 1^+ ground state of ^{12}B to the 0^+ states of ^{12}Be. Since the total change of angular momentum $\Delta J = \Delta L + \Delta S = 1$, the $\Delta L = 0$ component of the cross-section for these transitions is guaranteed to involve spin-transfer $\Delta S = 1$, satisfying the requirements for Gamow-Teller transitions. Consequently, for the study of the ^{12}B(^{7}Li, ^{7}Be)^{12}Be reaction, the singles data is as useful as the coincidence data, and much improved statistics are achievable.

1.4 Outline

This chapter has introduced the atomic nucleus, the Nuclear Shell Model, and the basics of charge-exchange reactions. It has provided an historical overview of charge-exchange studies, and has introduced the general principles of (^{7}Li,^{7}Be) charge-exchange experiments in inverse kinematics. Chapter 2 will motivate the study of ^{12}Be, and Chapter 3 will discuss (^{7}Li, ^{7}Be) reaction theory in the Distorted Wave Born Approximation framework. Chapter 4 will detail the experiment itself, Chapter 5 will describe the data analysis procedure, and Chapter 6 will present the result and compare to previous work. Chapter 7 will summarize this dissertation and provide a brief outlook for possible future studies.

Chapter 2

Motivation

In the Independent Particle Model, ^{12}Be, with four protons and eight neutrons, is a "semi-magic" nucleus, and the ground state configuration consists of neutrons completely filling the $0s$ and $0p$ shells, as depicted in Figure 2.1. In reality, the situation is much more complicated, and more than forty years of experimental and theoretical work have gone in to understanding the structure of this light, unstable nucleus. This chapter will give a brief overview of the reasons for configuration mixing in ^{12}Be. It will place the current study in an historical context, and highlight the benefits of gaining a better understanding of the Gamow-Teller strength distribution in ^{12}Be.

2.1 Nuclear Structure Away from Stability

One of the main goals of nuclear physics is to understand the evolution of nuclear structure away from stability. In unstable systems, the ordering of the single particle orbitals shown in Figure 1.4 changes, quenching the major shell gaps and creating new, smaller gaps at different proton and neutron numbers. This rearrangement of single-particle orbitals can
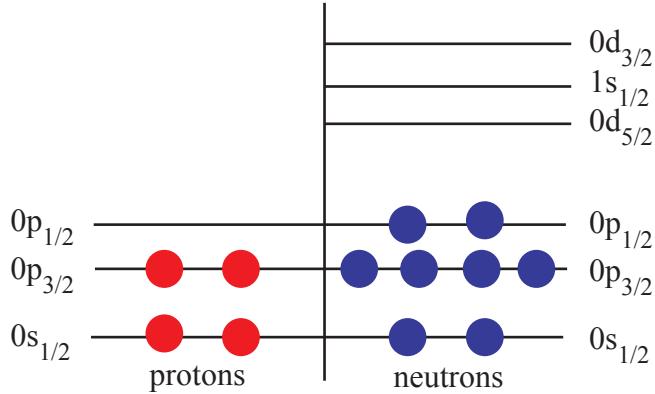
Figure 2.1: Simplest ground-state configuration for ^{12}Be.

lead to complications when trying to predict nuclear structure, and as a result calculations involving unstable systems often require large configuration spaces to reproduce experimentally observed properties[1].

Light unstable nuclei provide a fertile testing ground for nuclear structure models, as exotic phenomena (neutron halos, borromean systems, parity inversion of low-lying states) can be found in isotopes with only a few nucleons more or less than stable species. The configuration spaces for light nuclei are relatively small, and calculations are less computationally taxing than those for medium or heavy isotopes. The configuration space of interest for ^{12}Be includes the $0p$, $1s$, and $0d$ orbitals. The $0s$ and $1p0f$ orbitals were included in all of the calculations presented here, but for the most part these orbitals can be ignored for Gamow-Teller transitions, as excitations into the pf shell are impossible and transitions involving the $0s$ nucleons are Pauli-blocked.

When contemplating the structure of ^{12}Be, it helps to consider the systematics of neighboring nuclei. Tensor and central components of the proton-neutron monopole interaction

---

[1]While this single-particle description is illustrative and is often used to describe the evolution of shell structure away from stability, the complete many-body problem is actually much more complicated - for interested readers, a more robust description can be found in Refs. [47, 48].

are stronger in ^{14}C and ^{16}O than in ^{12}Be, because more protons occupy the $0p_{3/2}$ orbital [49, 50]. This results in a higher energy $0p_{1/2}$ neutron orbit in ^{12}Be than in the more stable $N = 8$ isotones [50, 51]. In the exotic Beryllium isotopes, the $1s_{1/2}$ and $0d_{5/2}$ orbits are inverted, due to the smaller kinetic energy of the loosely-bound $1s_{1/2}$ orbital [52]. Together, these single-particle orbital shifts act to bring the $1s_{1/2}$ and $0p_{1/2}$ neutron orbitals closer together, making configurations in which neutrons occupy $1s$ or $0d$ orbitals more energetically favorable for ^{12}Be than for stable isotopes in the region.

Using the notation of the harmonic oscillator basis, we can describe many-body configurations in terms of the number of nucleons occupying the single-particle orbitals. For ^{12}Be, $(0s)^4(0p)^8$ configurations are referred to as "$0\hbar\omega$" configuration. "$2\hbar\omega$" configurations are those in which two nucleons are excited into the next harmonic oscillator shell, or one nucleon is excited up two oscillator shells. Examples of $2\hbar\omega$ configurations in ^{12}Be include $(0s)^4(0p)^6(1s0d)^2$, $(0s)^3(0p)^8(1s0d)^1$, and $(0s)^4(0p)^7(1p0f)^1$. Due to the structure systematics discussed in the previous paragraph, $(0s)^4(0p)^6(1s0d)^2$ is the most probable $2\hbar\omega$ configuration, where the two nucleons in the $1s0d$ orbitals are neutrons.

The $0\hbar\omega$ configuration and most probable $2\hbar\omega$ configuration are shown in Figure 2.2. Naïvely, one would expect $0\hbar\omega$ configurations to have a lower total energy than $2\hbar\omega$ configurations. However, because of pairing and alpha correlation effects [52], $0\hbar\omega$ and $2\hbar\omega$ configurations in ^{12}Be are approximately degenerate in energy. As a result, the physical ground and excited 0^+ states in ^{12}Be consist of a mixture of these two configurations. If the two configurations were exactly equal in energy, the ground and excited 0^+ state would consist of equal parts $0\hbar\omega$ and $2\hbar\omega$ configurations. The precise configuration mixing in ^{12}Be is still under debate.
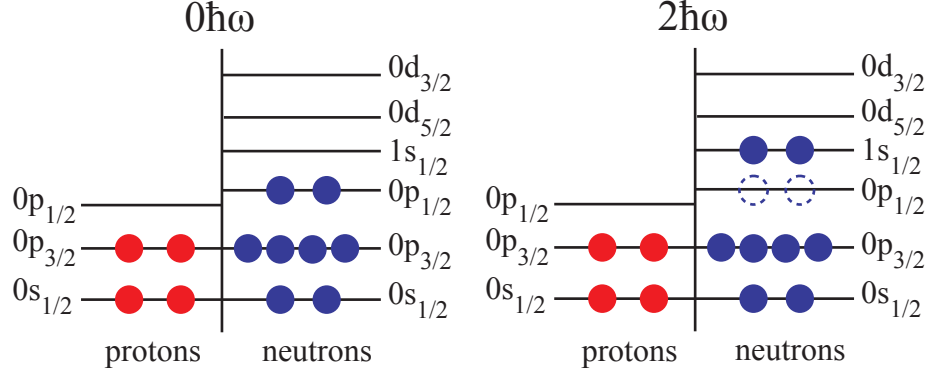
Figure 2.2: Example of $0\hbar\omega$ and $2\hbar\omega$ configurations in ^{12}Be.

2.2 History of ^{12}Be

^{12}Be was first discovered in 1965 in proton-irradiation experiments on ^{15}N [53]. Ten years later, noting "considerable discrepancies" between calculated and experimental masses, excitation energies, and widths, F.C. Barker proposed a model for the T=2 states of A=12 nuclei in which only small components of the states belong to $0\hbar\omega$ configurations [54]. Based on Talmi and Unna's description of ^{11}Be as a ^{10}Be core plus a $1s_{1/2}$ neutron [51], Barker predicted that low-lying 0^+ states in ^{12}Be should be formed with the same ^{10}Be core and a pair of neutrons in the $1s_{1/2}$, $0p_{1/2}$, or $0d_{5/2}$ orbit. Support for this hypothesis came just two years later, when the β-decay half-life and excitation energy of the first 2^+ state were measured and found to be longer and lower than that predicted by a pure $0\hbar\omega$ calculation [55].

Over the next two decades, theorists strived to gain a more complete understanding of ^{12}Be, driven by experimental data. By the early 1980's, three states in the ^{12}Be level scheme had been confirmed: a 0^+ ground-state, 2^+ first excited state at 2.11 MeV, and another state at 2.68 MeV [56] (later determined to have spin-parity 1^- [57]). Interpreting ^{10}Be(t,p) experimental data, H.T. Fortune *et al.* predicted that the low-lying states of ^{12}Be would

be dominated by $2\hbar\omega$ configurations, but emphasized the need for more serious shell-model calculations with proper accounting for $0\hbar\omega+2\hbar\omega$ configuration mixing [58]. Other models developed during this time described the observed ^{12}Be ground state properties in terms two neutrons coupled to an excited ^{10}Be core, requesting (p,t) reaction measurements [59], and attempted to understand the quenching of the $N=8$ shell gap in terms of its effect on β-decay half-lives and Gamow-Teller strength [60]. The latter work stressed "it would be extremely interesting to measure the Gamow-Teller strength distribution in ^{12}Be".

Near the turn of the century, inverse kinematics experiments employing rare isotope beams brought a flurry of experimental activity studying ^{12}Be. Inelastic proton scattering and inelastic ^{12}Be scattering measurements performed by Iwasaki *et al.* demonstrated that the neutron-rich beryllium isotopes exhibited a tendency towards strong quadrupole deformation [61] and identified unambiguiously the spin and parity of the 2.68 MeV 1^- state [57]. These observations supported the hypothesis that the $N=8$ shell closure in ^{12}Be was significantly smaller than in stable $N=8$ isotopes. The first *direct* evidence for the breakdown of the $N=8$ shell closure came from a (^{12}Be,^{11}Be+γ) neutron-knockout measurement performed at NSCL [62], which suggested a ^{12}Be ground state configuration that was 32% $0\hbar\omega$ and 68% $2\hbar\omega$. This experiment also indicated a reduced role for ^{10}Be core excitation than previous proposed [63]. A subsequent knockout experiment, designed to measure the $(0s)^4(0p)^6(0d)^2$ component of the wavefunction independently, verified the NSCL results [64]. With the discovery of an isomeric 0^+ state at 2.24 Mev [65], the spectrum of ^{12}Be below the neutron decay threshold was completed. The ^{12}Be level scheme is shown in Figure 2.3.

During this experimental renaissance, controversy over the extent of configuration mixing
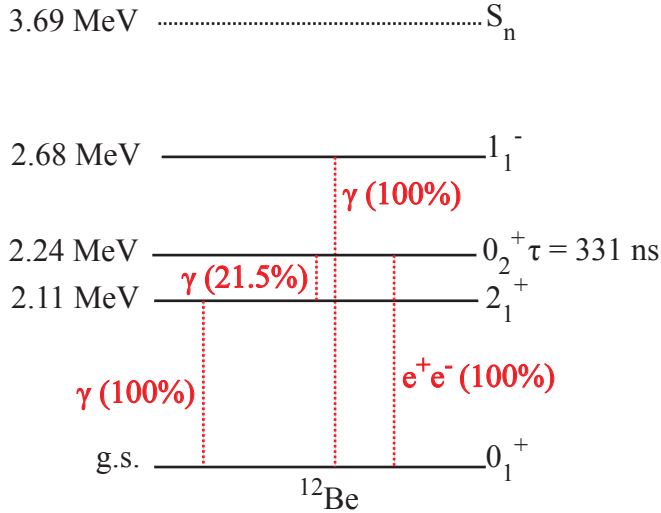
Figure 2.3: Level scheme, ^{12}Be.

in the 0^+ states of ^{12}Be was escalating. Citing instabilities with the available shell-model calculations, in 1999 R. Sherr and H.T. Fortune developed a "relatively simple" model for the $T = 2$, 0^+ states of $A = 12$ nuclei based on Coulomb shifts. Using a Woods-Saxon nuclear potential and a uniform sphere Coulomb potential, Sherr and Fortune calculated the binding energies of the $T = 2$, 0^+ states for three configurations: a $0p_{1/2}$, $1s_{1/2}$, or $0d_{5/2}$ neutron coupled to the appropriate $A = 11, T = 3/2$ state $(1/2^-, 1/2^+, 5/2^+)$. Finding that the $(0s)^4(0p)^8$ and $(0s)^4(0p)^6(0d)^2$ contributions to the ^{12}Be ground state were approximately equal, they performed a one-parameter fit to the experimental binding energies to estimate the $(0s)^4(0p)^6(1s)^2$ fraction of the wavefunction (55%) [66]. The exact $0p : 1s : 0d$ ratio in ^{12}Be was then determined by assuming the physical ground state must be a mixture of the lowest energy $0\hbar\omega$ and $2\hbar\omega$ configurations, yielding a final ground state configuration of 32% $0\hbar\omega$, 68% $2\hbar\omega$. The wavefunction for the excited 0^+ state was estimated by assuming the two 0^+ states sum to 100%: the 0_2^+ wavefunction consists of 68% $0\hbar\omega$ and 32% $2\hbar\omega$. Fortune and Sherr claimed calculations using these wavefunctions reproduced experimental cross-sections, excitation energies, and widths better than the original shell-model calcula-

21

tions performed by Barker in 1976 [67].

In 2009 Barker responded, arguing that Fortune and Sherr had interpreted the data incorrectly, leaving out weak states and making assumptions about spins and parities of states in ^{12}C that were not yet definitively proven. Making minor modifications to his 20-year old calculation, Barker claimed that a correct interpretation of the data in fact supported his model, in which the ground state of ^{12}Be is still 32% $0\hbar\omega$ and 68% $2\hbar\omega$, but the excited 0^+ state is made up of 42% $0\hbar\omega$ and 58% $2\hbar\omega$ configurations [68]. Fortune and Sherr then reitterated their beliefs that Barker's interpretation was flawed and suggested that improved experimental data could easily settle the issue [69]. During this period, several other models for ^{12}Be were developed, including a ^{10}Be$+n+n$ three-body calculation that compared well with the discrete and continuum energy spectrum of ^{12}Be, and measured electric transition strengths (which were not considered by Fortune and Sherr or Barker) [70].

As recently as 2010, ^{11}Be$(d, p)^{12}$Be transfer measurements explored the $(0s)^4(0p)^6(1s)^2$ $2\hbar\omega$ configurations of the 0^+ levels in ^{12}Be [71]. The extracted $2\hbar\omega$ component of the ground state is smaller than most models predict, and a recent paper by Fortune and Sherr has questioned the result [72]. Clearly, the structure of the 0^+ states in ^{12}Be remains an open question, despite knockout, transfer, (t,p), and inelastic scattering experiments. A charge-exchange study of ^{12}Be could prove a valuable addition to the existing body of knowledge, helping clear up some of the controversy.

2.3 ^{12}B$(^7$Li, ^{7}Be$)^{12}$Be

Much of the direct evidence for $N = 8$ shell quenching obtained to date has been based on spectroscopic factors deduced from knockout and transfer experiments. Spectroscopic

factors can be defined as either an overlap of the many-body wave functions of the initial and final states (theoretical spectroscopic factors), or as the ratio of the experimental cross-section to that of a particular reaction model (experimental spectroscopic factors). Knockout and transfer measurements yield experimental spectroscopic factors, which are, by definition, dependent upon the reaction model employed, and can have relatively large errors that should be factored into any final conclusions. The spectroscopic factors from the neutron knockout experiment performed at NSCL, for example, had errors of approximately 20% - and since the *ratio* of these spectroscopic factors was used to deduce the ground state configuration of ^{12}Be, the uncertainty in the wavefunction - not cited in Ref. [62] - would likely be large. Since both knockout and transfer measurements probe the $2\hbar\omega$ component of the 0^+ states wavefunctions, an experimental technique should be developed that can selectively probe the $0\hbar\omega$ configurations of ^{12}Be. This measurement would provide a complement to the knockout and transfer measurements, and may be able to confirm or exclude the previous results.

As described in Chapter 1, the Gamow-Teller transitions probed in charge-exchange experiments are $\Delta L = 0$, $\Delta S = 1$ transitions. The 1^+ ground state of ^{12}B is dominated by $0\hbar\omega$ configurations. Gamow-Teller transitions into ^{12}Be, therefore, are: (1) restricted to the 0^+ and 2^+ states in ^{12}Be, as $\Delta J = \Delta L + \Delta S = 1$; and (2) capable of probing only the $0\hbar\omega$ component of the wavefunction. This selectivity makes these reactions an ideal tool for exploring the $0\hbar\omega$ component of the ground and 0_2^+ state wavefunction in ^{12}Be.

The sensitivity of the B(GT) distribution to configuration mixing in ^{12}Be can be seen in Figure 2.4. Shown are predicted B(GT) values for transitions to 0^+ states in ^{12}Be, calculated using the shell-model code OXBASH [6] with the WBP interaction [73] in the *spsdpf* model space. On the left is a calculation in which only $0\hbar\omega$ configurations are allowed. All 0^+

strength is concentrated in the ^{12}Be ground state. Since the WBP interaction was not originally derived for mixed $n\hbar\omega$ configurations (i.e. $0\hbar\omega$ mixed with $2\hbar\omega$), it must be altered slightly to account for the mixing of high-lying $(n+2)\hbar\omega$ configurations with low-lying $n\hbar\omega$ states. In terms of energy, written explicitly, $2\hbar\omega$ admixtures push down $0\hbar\omega$ states, but in addition $4\hbar\omega$ admixtures push down $2\hbar\omega$ states, and $6\hbar\omega$ admixtures push down $4\hbar\omega$ states - one would need to go to 8-$10\hbar\omega$ for a consistent calculation. Instead, as described in Refs. [73–75], one can use the change in the ground state energy for $0\hbar\omega$ and $0\hbar\omega+2\hbar\omega$ calculations (ΔE) to estimate the effect of higher-lying admixtures on the $2\hbar\omega$ states, and lower the energy of all $2\hbar\omega$ configurations by this estimate. This procedure has been performed for the calculations shown in the right panel of Figure 2.4 - all $2\hbar\omega$ configurations have been shifted by $\Delta E = -3$ MeV. Clearly, when $0\hbar\omega+2\hbar\omega$ mixing is included in the calculation, the 0^+ strength distribution is significantly altered, and the strength formerly concentrated in the ground state is now fragmented amongst the two 0^+ states. The total strength of each state, and also the ratio of Gamow-Teller strength of the two 0^+ states

$$R = \frac{B(GT)(0_2^+, 2.24 \text{ MeV})}{B(GT)(0_1^+, \text{g.s.})} \tag{2.1}$$

is very sensitive to the amount of $0\hbar\omega+2\hbar\omega$ configuration mixing in ^{12}Be. The aim of the current work is to measure the 0^+ B(GT) distribution in ^{12}Be, compare the results to shell-model predictions to determine the appropriate shift for $2\hbar\omega$ configurations (ΔE), and compare the $0\hbar\omega$ component of the wavefunction in the ground and 2.24 MeV 0^+ state from these (shifted) calculations to those obtained in previous experimental and theoretical work.

The next three chapters will focus on the details of the theoretical cross-section calculations, experiment, and analysis - further discussion of the B(GT) distribution in ^{12}Be and
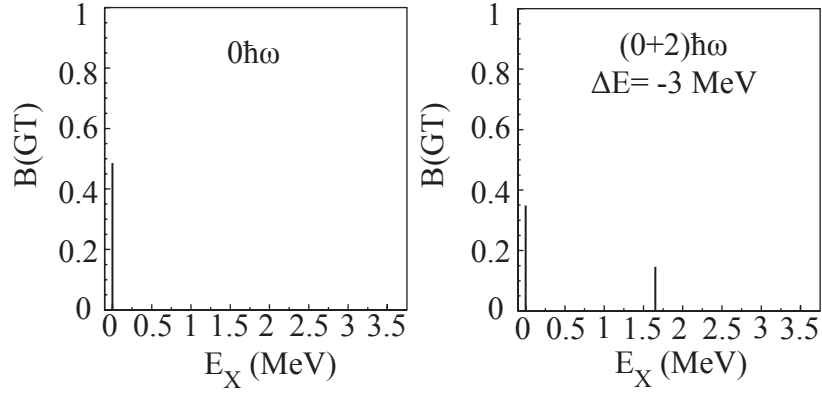
Figure 2.4: Calculated B(GT) distribution, for transition to 0^+ states in ^{12}Be below the neutron decay threshold (3.69 MeV). Values have been quenched according to Ref. [76]. $0\hbar\omega$, $2\hbar\omega$, and ΔE refer to the restrictions and shifts in the calculation - see text for details.

implications for the existing models will be continued in Chapter 6.

Chapter 3

Theory

The proportionality between differential cross-sections measured in charge-exchange experiments and Gamow-Teller strength (Equation 1.12) requires the isolation of transitions with no transfer of orbital angular momentum ($\Delta L = 0$). To extract the $\Delta L = 0$ component from the measured differential cross-section, a Multipole Decomposition Analysis (MDA) was performed using theoretical angular distributions. The MDA will be described in detail in Chapter 6. This chapter will discuss the calculation of theoretical angular distributions in the Distorted Wave Born Approximation (DWBA).

3.1 Distorted Wave Born Approximation

Nuclear reactions are modeled as one nucleus scattering off another - the projectile nucleus is treated as an incoming wave, and the outgoing (scattered) wave is characterized by a scattering amplitude $f(\theta, \phi)$. This scattering amplitude is directly related to the differential

cross-section:

$$\frac{d\sigma}{d\Omega} \propto \frac{k_f}{k_i}|f(\theta, \phi)|^2 \ , \tag{3.1}$$

where k_i and k_f refer to the momentum of the incoming and outgoing wave. The scattering amplitude (written in terms of momentum vectors) can also be expressed in terms of a transition amplitude between initial and final states T_{fi}

$$f(\vec{k}_f, \vec{k}_i) = -\frac{\mu}{2\pi\hbar}T_{fi}(\vec{k}_f, \vec{k}_i) \ , \tag{3.2}$$

where μ is the reduced energy of the incoming projectile (1) and the target (2)

$$\mu = \frac{E_1 E_2}{E_1 + E_2} \ . \tag{3.3}$$

These transition amplitudes are calculated in the Distorted Wave Born Approximation (DWBA).

The starting point for calculating transition amplitudes in DWBA is the Schrödinger equation, where the Hamiltonian contains standard kinetic and potential terms K and V

$$H\Psi = (K + V)\Psi = E\Psi \ . \tag{3.4}$$

For many cases, the potential V can be described as a combination of two terms: one term (U_1) that describes the distortion of incoming and outgoing waves due to the mean field of the target nucleus, and another term (U_2) that describes the interaction between individual nucleons

$$V = U_1 + U_2 \ . \tag{3.5}$$

With a potential of this form, the transition amplitude T_{fi} can also be written as a combination of two terms [77]

$$T_{fi} = T^1 + T^{2(1)} \ , \tag{3.6}$$

27

where T^1 describes all effects of the distorting potential U_1 and $T^{2(1)}$ describes all residual effects after distortion has been accounted for. For this reason U_2 is sometimes referred to as the residual interaction. Since the initial and final states in a charge-exchange reaction aren't directly connected by U_1, the effect of the distorting potential can be factored into the calculation by treating the incoming beam as already distorted by U_1. In terms of the transition amplitude, the first term of Equation 3.6 drops out, leaving the residual term only

$$T_{fi} = T^{2(1)} \ . \tag{3.7}$$

Switching to bra-ket notation, this transition amplitude can be written in the *prior form*, in terms of the initial (already distorted by U_1) wave $\langle \chi^- |$, the residual interaction U_2, and the outgoing scattered wave $| \Psi \rangle$

$$T_{fi} = \langle \chi^- | U_2 | \Psi \rangle \tag{3.8}$$

Then, using Green's function methods and the Lippmann-Schwinger equation for the exact wavefunction solution Ψ (see e.g. [77,78])

$$\Psi = \chi + \hat{G}_1 U_2 \Psi$$

$$\hat{G}_1 = [E - K - U_1]^{-1} \ , \tag{3.9}$$

one can expand the transition amplitude to obtain the Born Series

$$T_{fi} = \langle \chi^- | U_2 | \chi \rangle + \langle \chi^- | U_2 G_1 U_2 | \chi \rangle + ... \tag{3.10}$$

Since the residual interaction (U_2) is weak relative to the distorting potential (U_1), the transition amplitude can be truncated to the first term in the series

$$T_{fi} = \langle \chi^- | U_2 | \chi \rangle \ . \tag{3.11}$$

This approximation is known as (first order) DWBA.

The expression for the transition density given in Equation 3.11 is deceptively simple in appearance. In practice, to calculate T_{fi} one needs both nuclear structure and reactions input including: transition densities, which describe the overlap between the initial and final states of both the projectile/ejectile and target/recoil systems; the effective nucleon-nucleon interaction, which will ultimately be folded over the transition densities to account for the composite nature of all particles involved, yielding form factors; and an optical model to describe distortion effects and calculate distorted waves. Here, each of these components of the transition amplitude is discussed separately, in the context of the WSAW/FOLD/DWHI code package [79] used to obtain theoretical cross-sections for this study.

3.2 Theoretical Cross-Section Calculations

Theoretical cross-sections calculations were performed with the WSAW/FOLD/DWHI code package [79], designed for charge-exchange studies with composite probes. First, one calculates transition densities for the projectile/ejectile and target/recoil systems using single particle radial wavefunctions generated in WSAW and one-body transition densities (OBTDs) obtained from OXBASH [6]. Then, the program FOLD generates form factors, which are combined with an optical potential in the code DWHI to calculate transition amplitudes and separate angular distributions for each allowed value of total angular momentum transfer J.

3.2.1 Transition Densities

Transition densities describe the overlap between the initial and final states in the projectile/ejectile and target/recoil system. Essentially a way to connect single-particle wave-

functions and operators to a many-body problem, they have two major components: radial wavefunctions for the one-particle and one-hole single-particle orbits, and one-body transition densities (OBTDs) that weigh the one-particle one-hole contributions.

The radial wavefunctions were generated in the program WSAW, which fits solutions to the Schrödinger equation such that they match binding energies. The WSAW potential contains Coulomb, Woods-Saxon and spin-orbit terms. The binding energies were calculated using the Skx interaction [80] in the DENS subroutine of the OXBASH shell model code [6].

The OBTDs contain all information about couplings and spins and serve as a weighting factor for each one-particle, one-hole excitation, summed to construct the many-body transition densities:

$$\langle f||O(GT_{\pm})||i\rangle = \sum_{k_\alpha, k_\beta} OBTD(fik_\alpha k_\beta)\langle k_\alpha||O(GT_{\pm})||k_\beta\rangle \qquad (3.12)$$

(here, k_i refer to one-particle one-hole states and f, i, to many-body states). OBTDs used in this analysis were calculated using the code OXBASH [6]. The CKII interaction [81] was used in the p model space for the $^7\text{Li} \rightarrow {}^7\text{Be}$ OBTD calculation. The WBP [73] interaction was used in the $spsdpf$ model space for the $^{12}\text{B} \rightarrow {}^{12}\text{Be}$ OBTD calculation. The WBP interaction was intended for "pure $\hbar\omega$" calculations (i.e. no configuration mixing between major oscillator shells), but the $0\hbar\omega$ and $2\hbar\omega$ states in ^{12}Be are known to be degenerate in energy [62], and therefore matrix elements that mix n and $(n+2)\hbar\omega$ configurations are required. The interactions were changed to accurately calculate these mixed matrix elements, by shifting all $(n+2)\hbar\omega$ configurations by $\Delta E=$ -3 MeV, following the procedure described in Chapter 2.

3.2.2 Form Factors

Using the transition densities described in the previous section, separate form factors are calculated for each allowed transition, characterized by the relative transfer of total angular momentum (ΔJ_r), and the change in total angular momentum of the target and projectile $(\Delta J_p$ and $\Delta J_t)$. For each combination of ΔJ_r, ΔJ_p and ΔJ_t, the effective interaction V_{eff} is *double-folded* over the transition densities for the projectile/ejectile and target/recoil systems. This double-folding is necessary due to the composite probes involved - if the charge-exchange reaction involved a single-nucleon probe, only a single-folding procedure would be necessary.

The effective interaction is a sum of two-body terms involving nucleons in the target and projectile

$$V_{eff} = \sum_{p,t} v_{pt}(\vec{s})(1 - P_{pt}) \ . \tag{3.13}$$

Here, $\vec{s}$ refers to the separation between the target and projectile nucleon and P_{pt} is an antisymmetrization operator. A short-range approximation is used for exchange terms, as discussed in Ref. [23]. The nucleon-nucleon (NN) interaction v_{pt} was derived via a phase shift analysis of NN scattering data - the 100 MeV parameterization was used in the calculations presented here [23,24]. This interaction was chosen for its factorization into spin- and isospin-transfer terms, convenient for charge-exchange studies. The NN interaction contains central, spin-orbit and tensor terms

$$v_{pt} = v^C(\vec{s}) + v^{LS}(\vec{s}) + v^T(\vec{s})$$

$$v^C = v_\tau(\vec{s})(\vec{\tau_p} \cdot \vec{\tau_t} + v_{\sigma\tau}(\vec{s})(\vec{\sigma_p} \cdot \vec{\sigma_t})(\vec{\tau_p} \cdot \vec{\tau_t})$$

$$v^{LS} = v_{LS\tau}(\vec{s})(\vec{L} \cdot \vec{S})(\vec{\tau_p} \cdot \vec{\tau_t}) \tag{3.14}$$

$$v^T = v_{TT}(\vec{s})S_{pt}(\vec{\tau_p} \cdot \vec{\tau_t})$$

$$S_{pt} = \frac{(\sigma_p \cdot \vec{s})(\sigma_t \cdot \vec{s})}{s^2} - \sigma_p \cdot \sigma_t \ ,$$

Angular Momentum Selection Rules
$\Delta J_t = J_{ti} \oplus J_{tf}$
$\Delta J_p = J_{pi} \oplus J_{pf}$
$\Delta J_r = \Delta J_p \oplus \Delta J_t$
$(-1)^{\Delta L_t} = (\pi_i \pi_f)_t$
$(-1)^{\Delta L_p} = (\pi_i \pi_f)_p$
$\Delta L_r = \Delta L_p \oplus \Delta L_t$
$\Delta J_r = \Delta L_t$

Table 3.1: Angular momentum selection rules. Subscript r refers to relative transfers of angular momentum. Subscript p refers to projectile/ejectile system, t to target/recoil system, i to initial state and f to final state. Valid for central nucleon-nucleon interaction terms only; tensor terms will be discussed in Section 3.4.

where only terms relevant to isovector transitions have been included. The central isoscalar term (not included explicitly in Equation 3.14 but similar to v^C, without τ components) is responsible for mean field distortions and multistep processes.

The angular momentum selection rules for a each transition are given in Table 3.1, and depend on the initial i and final f total angular momentum J and parity π for the projectile p and target t. Form factors are calculated for each value of relative angular momentum transfer ΔJ_r. The last line of Table 3.1 is only valid for central terms of the effective nucleon-nucleon interaction - spin-orbit terms do not play a significant role [82], and tensor terms will be discussed in detail in Section 3.4. The program FOLD executed the double-folding procedure and produced form factors formatted for input into DWHI.

3.2.3 Cross-Sections

The last step in the transition amplitude calculation involves accounting for the distortion effects of the mean field. Usually, one would obtain an optical model by fitting elastic scattering data measured under the same experimental conditions as the charge-exchange

V(MeV)	r(fm)	a_0(fm)	W_v(MeV)	r_w(fm)	a_w(fm)
108	1.375	0.854	37.9	1.671	0.758

Table 3.2: Optical potential parameters used in DWHI program to calculate distorted waves. Taken from Ref. [83].

experiment (same beam, same target, and same incident energy). When this is not possible, one can use a published optical potential derived from similar data. For the current study, the most suitable optical potential available in the literature was a fit to elastic scattering measurements of ^{7}Li on ^{12}C at 50 MeV/u [83](recall, the current study involves ^{7}Li and ^{12}B at 80 MeV/u). The optical potential contained Coulomb, real and imaginary Woods-Saxon terms

$$U(r) = U_c(r, r_c) - Vf(r, r_0, a_0) - iW_vf(r, r_w, a_w)$$

$$f(r, r_x, a_x) = \frac{1}{1 + exp^{[(r - r_x A_t^{1/3})/a_x]}} \quad . \tag{3.15}$$

The Woods-Saxon optical potential parameters included in the calculation are given in Table 3.2. All three terms were used in the DWHI calculation to calculate distorted waves.

The distorted waves were combined with FOLD form factors to calculate transition amplitudes. The mass and kinematic factors of Equations 3.1 and 3.2 are also input into DWHI, and angular distributions were calculated for each allowed value of total angular momentum transfer. The WSAW/FOLD/DWHI angular distributions are shown in Figures 3.1 through 3.8. The DWBA cross-sections generally do a good job reproducing experimental cross-sections obtained in charge-exchange experiments, but since approximations were used for the optical potential and the energy shift ΔE, the absolute magnitudes of the components are tuned during the MDA procedure described in Chapter 6.

All transitions originate in the ground states of ^{12}B and ^{7}Li. Figures 3.1 through 3.4 are
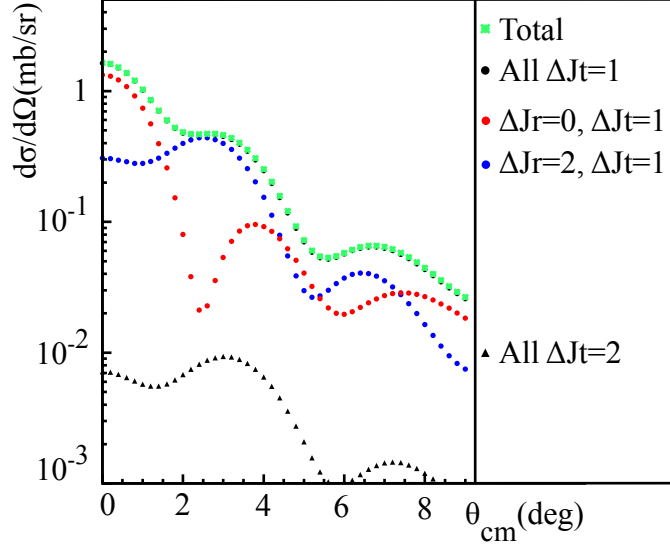
Figure 3.1: Angular distributions produced using the WSAW/FOLD/DWHI code package for the ^{12}B(g.s., 1^+) $\rightarrow$ ^{12}Be(g.s., 0^+), ^{7}Li(g.s., $3/2^-$) $\rightarrow$ ^{7}Be(429 keV, $1/2^-$) transition. Black dots (all $\Delta J_t=1$) are not visible because they are effectively underneath green stars (total cross-section).

for transitions to the 429 keV excited state in ^{7}Be.

- Figure 3.1 shows the theoretical angular distributions for the transition to the ground state of ^{12}Be. One of the simplest angular distributions calculated, it contains just three components, one of which ($\Delta J_r=2$, $\Delta J_t=2$, $\Delta J_p=1$) is negligible. At zero degrees, the $\Delta J_r=0$ term is nearly an order of magnitude larger than any other component.

- Figure 3.2 shows the theoretical angular distributions for the transition to the 2.11 MeV 2^+ state of ^{12}Be. Due to the many possible combinations of $\Delta J_r, \Delta J_p$ and ΔJ_t, there are several more components contributing to the total cross-section, and it is not sufficient at the largest angles to include only $\Delta J_r=0$, $\Delta J_t=1$ components for this case. However, at zero degrees the $\Delta J_r=0$ component is still dominant.

- Figure 3.3 shows the theoretical angular distributions for the transition to the 2.24
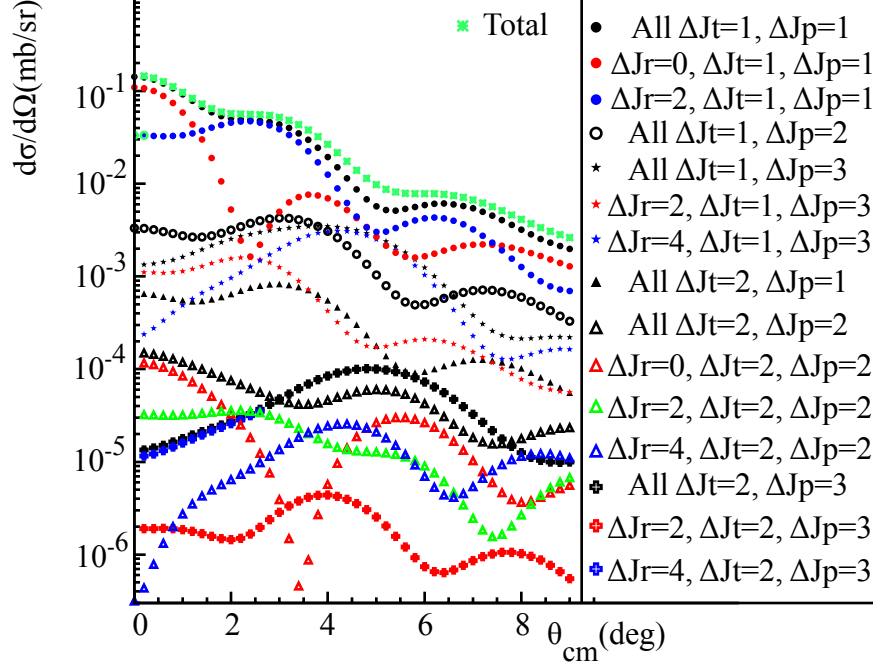
Figure 3.2: Angular distributions produced using the WSAW/FOLD/DWHI code package for the ^{12}B(g.s., 1^+) $\rightarrow$ ^{12}Be(2.11 MeV, 2^+), ^{7}Li(g.s., $3/2^-$) $\rightarrow$ ^{7}Be(429 keV, $1/2^-$) transition.

MeV 0^+ state in ^{12}Be . As with the ^{12}Be ground-state calculation, there are three components, ΔJ_r=2 ΔJ_t=2 ΔJ_p=1 is negligible, and only ΔJ_t=1 terms are needed to adequately reproduce the total cross-section. ΔJ_r=0 is again dominant at zero degrees.

- Figure 3.4 shows the theoretical angular distribution for the transition to the 2.68 1^- state in ^{12}Be. The angular distributions are quite different from those shown in the previous figures - they no longer peak at zero degrees, as expected for dipole states, and the ΔJ_r=1 and ΔJ_r=3 components are now dominant. The total cross-section is well-described using the ΔJ_t=1 and ΔJ_p=2 components only.

Figures 3.5 through 3.8 show transitions to the ground state of ^{7}Be.

- Figure 3.5 shows the theoretical angular distributions for the transition to the ground state of ^{12}Be. There are more components than the coincidence case (transitions
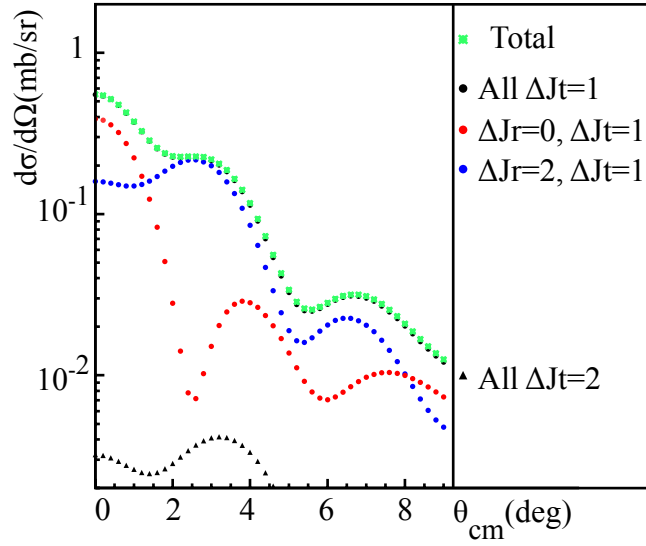
Figure 3.3: Angular distributions produced using the WSAW/FOLD/DWHI code package for the ^{12}B(g.s., 1^+) $\rightarrow$ ^{12}Be(2.24 MeV, 0^+), ^{7}Li(g.s., $3/2^-$) $\rightarrow$ ^{7}Be(429 keV, $1/2^-$) transition.
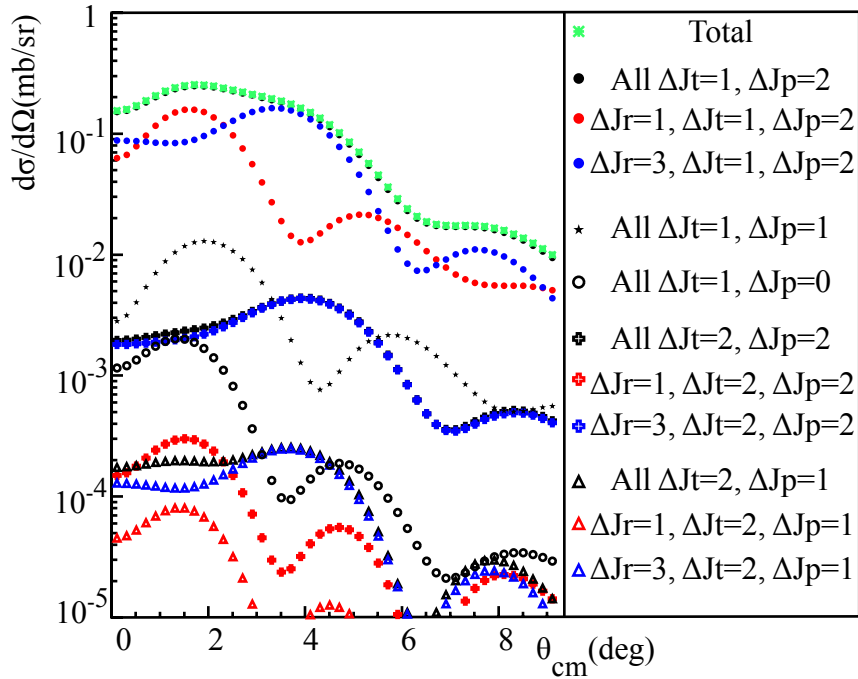
Figure 3.4: Angular distributions produced using the WSAW/FOLD/DWHI code package for the ^{12}B(g.s., 1^+) $\rightarrow$ ^{12}Be(2.68 MeV, 1^-), ^{7}Li(g.s., $3/2^-$) $\rightarrow$ ^{7}Be(429 keV, $1/2^-$) transition.
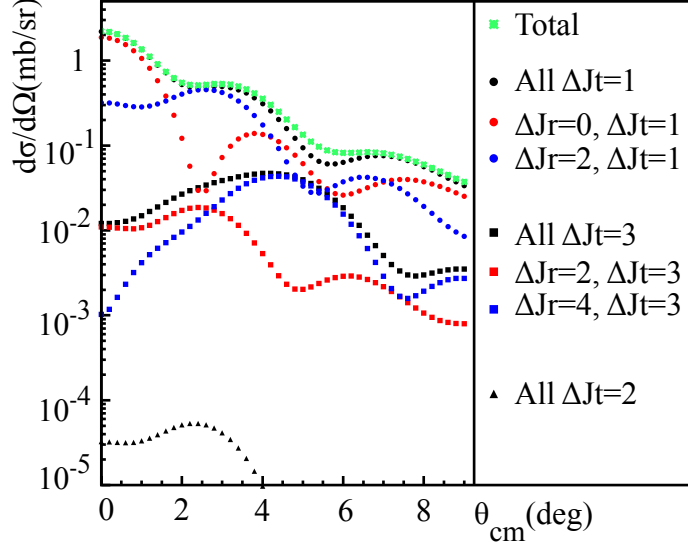
Figure 3.5: Angular distributions produced using the WSAW/FOLD/DWHI code package for the ^{12}B(g.s., 1^+) $\rightarrow$ ^{12}Be(g.s., 0^+), ^{7}Li(g.s., $3/2^-$) $\rightarrow$ ^{7}Be(g.s., $3/2^-$) transition.

through the 429 keV state in ^{7}Be, Figure 3.1), but the same trends are apparent: ΔJ_r=2, ΔJ_t=2 terms are negligible, and with the exception of the angular region between 4 and 8 degrees, the total cross section can almost be reproduced by only including ΔJ_t=1 terms, and at zero degrees the ΔJ_r=0 term is significantly larger than any other component.

- Figure 3.6 shows the theoretical angular distributions for the transition to the 2.11 MeV 2^+ state of ^{12}Be. This is the most complicated case calculated, and as with the analogous case (Figure 3.2) it is not sufficient at large angles to include only ΔJ_r=0, ΔJ_t=1 components. However, at zero degrees the ΔJ_r=0 component is still the largest contribution to the total cross-section.

- Figure 3.7 shows the theoretical angular distributions for the transition to the 2.24 MeV 0^+ state in ^{12}Be. As with the ^{12}Be ground state calculation, ΔJ_r=2, ΔJ_t=2 is negligible, and with the exception of the angular region between 4 and 8 degrees, only ΔJ_t=1 terms are needed to adequately reproduce the total cross-section. ΔJ_r=0 is

37
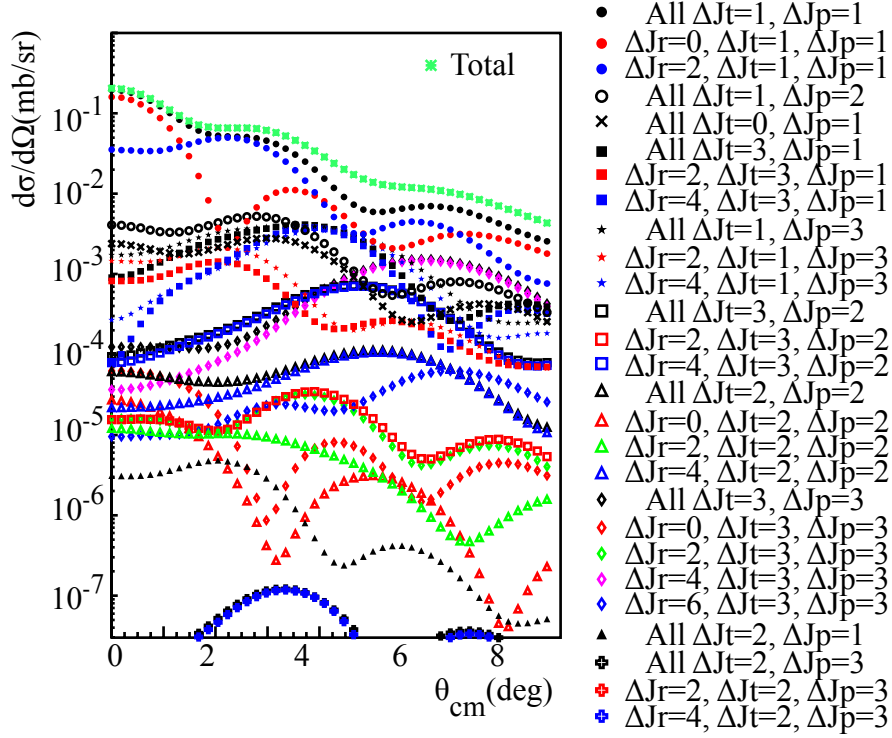
Figure 3.6: Angular distributions produced using the WSAW/FOLD/DWHI code package for the ^{12}B(g.s., 1^+) $\rightarrow$ ^{12}Be(2.11 MeV, 2^+), ^{7}Li(g.s., $3/2^-$) $\rightarrow$ ^{7}Be(g.s., $3/2^-$) transition.
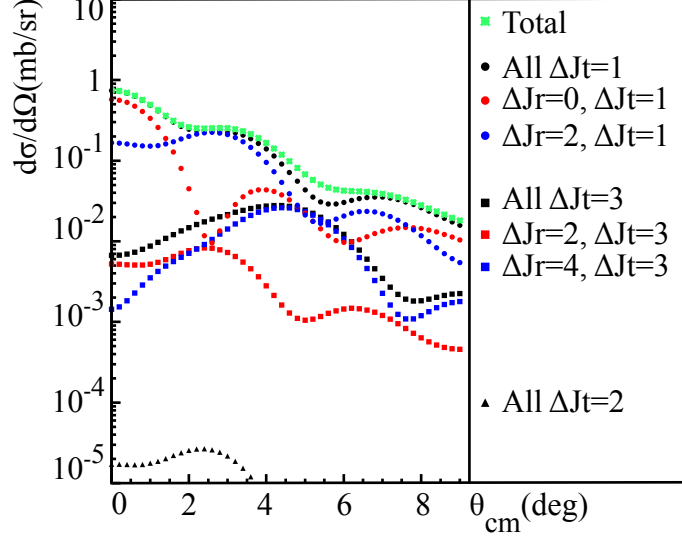
Figure 3.7: Angular distributions produced using the WSAW/FOLD/DWHI code package for the ^{12}B(g.s., 1^+) $\to$ ^{12}Be(2.24 MeV, 0^+), ^{7}Li(g.s., $3/2^-$) $\to$ ^{7}Be(g.s., $3/2^-$) transition.

still dominant at zero degrees.

- Figure 3.8 shows the theoretical angular distribution for the transition to the 2.68 MeV 1^- state in ^{12}Be. As with Figure 3.4, the angular distributions are quite different from those shown in the previous three figures: the $\Delta J_r=0$ component is no longer the largest at zero degrees, but the total cross-section can still be estimated using the $\Delta J_t=1$ and $\Delta J_p=2$ components only.

3.3 Extrapolation to $q=0$

The proportionality relationship between differential cross-section and B(GT) (Equation 1.12) is only valid when there is no transfer of angular momentum ($\Delta L = 0$), at the limit of zero momentum transfer ($q = 0$). To extract the $\Delta L = 0$ component of the differential cross-section, a Multipole Decomposition Analysis (MDA) was performed using cross-sections calculated in the DWBA formalism (Figures 3.1 through 3.8. The MDA procedure and
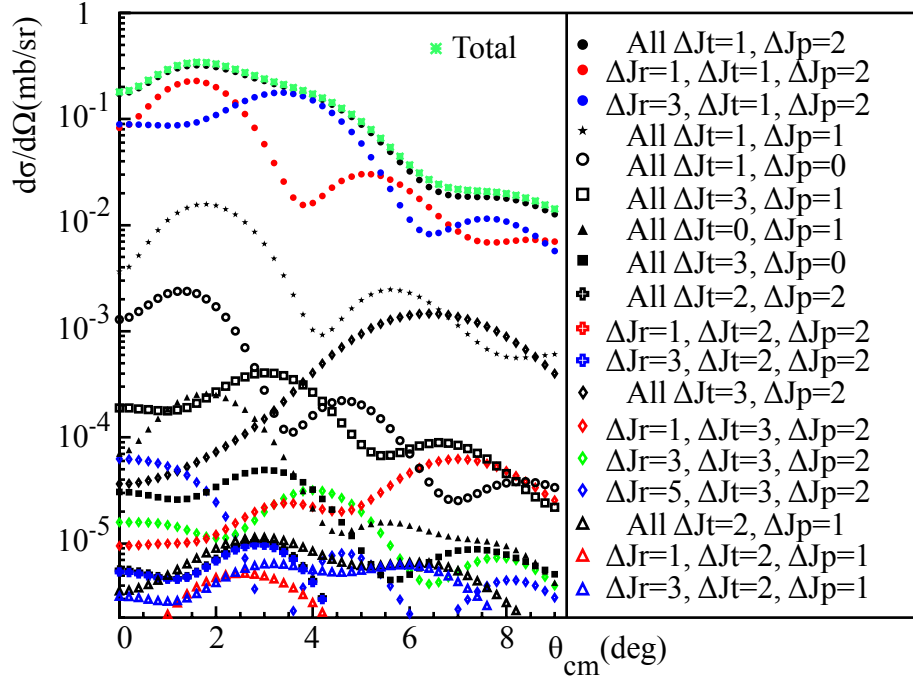
Figure 3.8: Angular distributions produced using the WSAW/FOLD/DWHI code package for the $^{12}\mathrm{B}$(g.s., 1^+) $\to$ ^{12}Be(2.68 MeV, 1^-), ^{7}Li(g.s., $3/2^-$) $\to$ ^{7}Be(g.s., $3/2^-$) transition.

extraction of $\Delta L = 0$ cross-section will be discussed further in Chapter 6. However, as the theoretical cross-sections shown here were used to obtain a scaling factor for the $q \to 0$ extrapolation, the extrapolation process is discussed here rather than in the context of the MDA.

Experimentally, $q = 0$ corresponds to a scattering angle of zero degrees and zero reaction Q-value - therefore, to extrapolate to $q = 0$, the total cross-section is measured at forward angles, and the zero-degree $\Delta L = 0$ cross-section is obtained from the MDA. Then, DWBA cross-sections are used to obtain a scaling factor relating the measured zero-degree $\Delta L = 0$ cross-section to that at zero Q-value:

$$\left[\frac{d\sigma}{d\Omega}\right]_{q=0} = \left[\frac{\frac{d\sigma}{d\Omega}(Q=0, \theta=0)}{\frac{d\sigma}{d\Omega}(Q=Q, \theta=0)}\right]_{DWBA} \times \left[\frac{d\sigma}{d\Omega}(Q=Q, \theta=0)\right]_{measured} \tag{3.16}$$

40

Case	^{7}Li $\rightarrow$ ^{7}Be Transition	^{12}B $\rightarrow$ ^{12}Be Transition	q (fm)$^{-1}$
1	^{7}Li(g.s) $\rightarrow$ ^{7}Be(g.s.)	^{12}B(g.s.) $\rightarrow$ ^{12}Be(g.s.)	0.153
2	^{7}Li(g.s.) $\rightarrow$ ^{7}Be(429 keV)	^{12}B(g.s.) $\rightarrow$ ^{12}Be(g.s.)	0.159
3	^{7}Li(g.s.) $\rightarrow$ ^{7}Be(g.s.)	^{12}B(g.s.) $\rightarrow$ ^{12}Be(2.24 MeV)	0.180
4	^{7}Li(g.s.) $\rightarrow$ ^{7}Be(429 keV)	^{12}B(g.s.) $\rightarrow$ ^{12}Be(2.24 MeV)	0.186

Table 3.3: Definitions and momentum transfer q at zero degrees for four cases relevant to $q=0$ extrapolation procedure (see text).

(all cross-sections refer to $\Delta L = 0$ components only).

The dependence of the DWBA $\Delta L = 0$ cross-section at zero degrees on momentum transfer q is shown in Figure 3.9. To calculate scaling factors, four separate cases needed to be considered, involving transitions to the ground and 429 keV states in ^{7}Be (related to singles and coincidence data sets) and transitions to the ground and 2.24 MeV states in ^{12}Be (the two 0^+ states of interest). These cases are labeled in Table 3.3, and the zero-degree momentum transfer associated with each case is provided for reference. All theoretical cross-sections were adjusted for resolution effects (see Section 6.1) before scaling factors were calculated. The coincidence data set uses the Case 2 scaling factor for transitions to the ground state of ^{12}Be and Case 4 for transitions to the 2.24 MeV state; the singles data uses a weighted average of Case 1 and 2 for transitions to the ground state of ^{12}Be and a weighted average of Cases 3 and 4 for transitions to the 2.24 MeV state (to reflect the population of both ^{7}Be states in the singles data set). The averaging procedure introduces an error of approximately 1%. The scaling factors used for the coincidence and singles data set are given in Table 3.4.
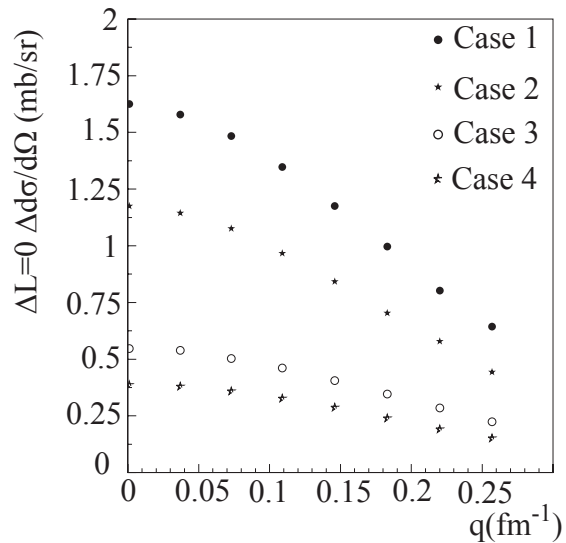
Figure 3.9: Zero-degree ΔL=0 cross-section as a function of linear momentum transfer q. Case labels are given in Table 3.3.

	Coincidences	Singles
^{12}Be(g.s.)	1.428	1.419
^{12}Be(2.24 MeV)	1.620	1.602

Table 3.4: DWBA scaling factors used in Equation 3.16 to extrapolate the zero-degree, ΔL=0 cross-sections to zero Q-value (and therefore zero momentum transfer).

3.4   Tensor Contributions

For a given form factor, the contribution from the central-$\sigma\tau$ and tensor-τ terms of the nucleon-nucleon interaction interfere. The last line of Table 3.1, which is valid for central terms only, changes to

$$\Delta J_r = \Delta L_t + K \qquad (3.17)$$

when tensor terms are present, with K equal to two. This results in Gamow-Teller transitions ($\Delta L_t = 0$) with relative angular momentum transfers $\Delta J_r = 2$, which cannot be isolated from other $\Delta J_r = 2$ components in the data. If the tensor-τ term is relatively strong, such as in the case of very weak transitions or low incident beam energies, the proportionality between cross-section and B(GT) (Equation 1.12) can be significantly affected, and in some cases can break down entirely [84].

To estimate the systematic uncertainty in the extraction of B(GT) due to tensor interference, calculations were performed with the tensor terms of the effective nucleon-nucleon interaction removed. An example of a no-tensor calculation is shown in Figure 3.10, and should be compared with Figure 3.1, which has the tensor term included. Comparing the $\Delta J_r{=}0$ cross-section at zero degrees with (T) and without (NT) inclusion of the tensor allows one to quantify the effect of the interference terms and estimate the possible systematic error in the $\Delta L_t{=}0$ cross-section due to tensor contributions. As with the extrapolation to $q{=}0$, a weighted average was used to estimate the singles data tensor errors.

The percent difference in the ΔL$=0$ cross-section at zero degrees with (T) and without inclusion of the tensor (NT) is given by

$$\%error = \left[1 - \frac{T}{NT}\right] \times 100 \qquad (3.18)$$
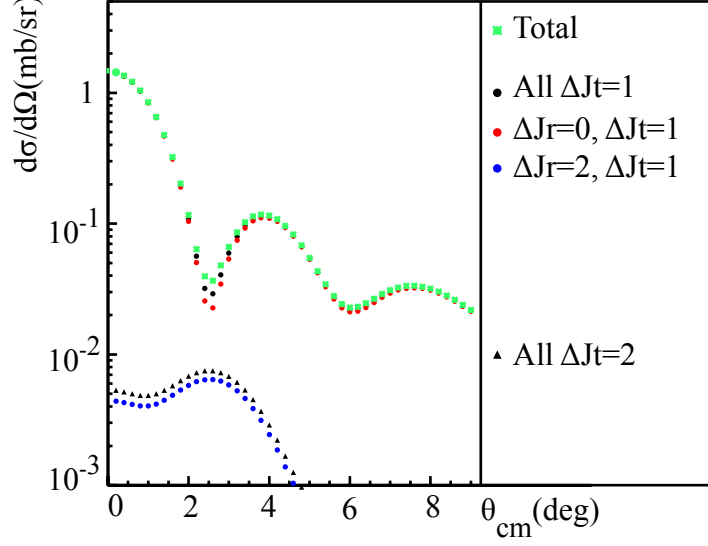
Figure 3.10: Angular distributions produced using the WSAW/FOLD/DWHI code package for the ^{12}B(g.s., 1^+) $\rightarrow$ ^{12}Be(g.s., 0^+), ^{7}Li(g.s., $3/2^-$) $\rightarrow$ ^{7}Be(429 keV, $1/2^-$) transition, with the tensor part of the effective interaction removed from the calculation. Should be compared with Figure 3.1.

	Coincidences	Singles
^{12}Be(g.s.)	+9.22%	+5.25%
^{12}Be(2.24 MeV)	+15.09%	+10.16%

Table 3.5: Systematic error in ΔL=0 cross-section due to interference of tensor components.

These systematic errors are shown in Table 3.5. With the tensor error quantified, all futher discussions regarding theoretical angular distributions will refer to the ΔJ_r=0 and ΔL=0 interchangeably, with $\Delta L = \Delta L_t$ implied.

This chapter has detailed the calculation of theoretical angular distributions in the DWBA framework using the WSAW/FOLD/DWHI code package. These angular distributions will ultimately be used in a Multipole Decomposition Analysis (MDA) to extract the $\Delta L = 0$ component of the measured differential cross-sections (Chapter 6).

Chapter 4

Experiment

Charged with investigating the B(GT) distribution in ^{12}Be, NSCL experiment 08017 - "Spectroscopy of ^{12}Be using the ^{12}B(^{7}Li,^{7}Be + γ) reaction in inverse kinematics" - ran in November 2009. This chapter details the production of ^{12}B and detection of ^{12}Be in experiment 08017.

4.1   Beam Preparation and Delivery

Rare isotope beams at NSCL are produced via fragmentation. In this process, a beam consisting of one stable isotope species is accelerated to semi-relativistic speeds and impinged upon a thick target. The resulting nuclear collisions produce a distribution of isotopes, including some rare species. The fragmentation products then go through a purification procedure, during which a beam consisting primarily of the isotope of interest is selected, tuned to experimenter specifications, and transported to the experiment.

4.1.1 Ion Source

The first step of beam production is the removal of electrons from stable element atoms. At NSCL, this is accomplished using Electron Cyclotron Resonance (ECR) ion sources. ECR ion sources confine plasma of a stable element in a magnetic bottle long enough for the particles to be ionized by collisions with moving electrons. The ionized particles are then extracted with an intermediate charge state and injected into the coupled cyclotrons for acceleration.

This experiment marked the first use of the Superconducting Source for Ions (SuSI) in a non-commissioning experiment. SuSI was designed to improve the intensity of heavy ion beams with medium charge states. It is a fully superconducting system with tunable magnetic fields, low electric power consumption, minimized risk of demagnetization, and an improved design with more room for attaching external devices [85]. For experiment 08017, SuSI was used to ionize ^{18}O atoms to a charge state of 3+.

4.1.2 Coupled Cyclotrons

The Coupled Cyclotron Facility at NSCL [86] currently houses two particle accelerators[1]: the K500 and K1200 cyclotrons, where the numeric designation refers to the maximum extraction energy for protons. In a cyclotron accelerator, an electric field is applied at a given radio frequency to accelerate ions, and a magnetic field is applied to keep the ions on an isochronous path. For ions heavier than protons, the maximum energy achievable depends on the radial size of the cyclotrons, the strength of the magnetic field, and the charge-to-mass (q/m) ratio of the particle - since the first two quantities are restricted by

---

[1]A third accelerator, ReA3, is currently under construction and will ultimately be used to reaccelerate stopped rare isotope beams to low energies (less than 6 MeV/nucleon).
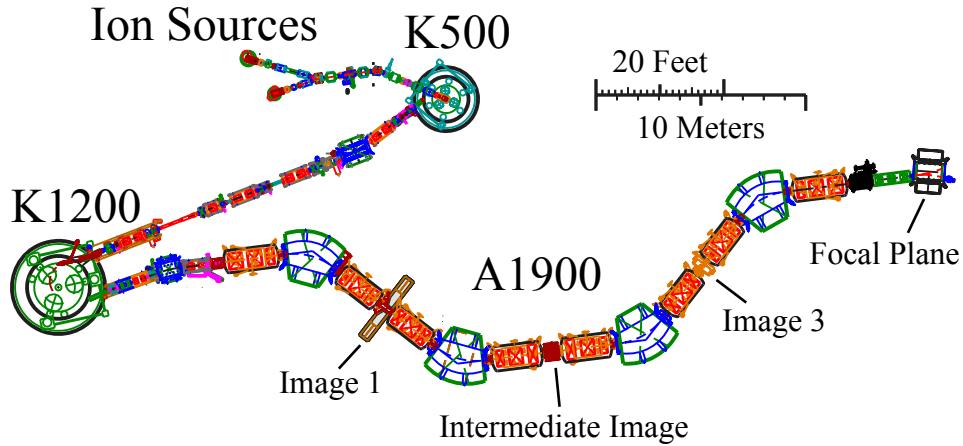
Figure 4.1: Schematic depicting NSCL ion sources, K500 and K1200 cyclotrons, and A1900 fragment separator. The production target is located in the blue box after the exit of the K1200 cyclotron and the before the entrance of the A1900 fragment separator.

the design of the cyclotron, for optimum acceleration high charge states (few electrons per atom) are preferable. To achieve these high charge states, the particles from the ion source are first accelerated in the K500, then extracted at an intermediate energy and impinged upon a thin carbon foil. Passage through this foil strips electrons from the beam particles, resulting in a higher charge-state that is injected into the K1200 for further acceleration.

After acceleration, this "primary beam" is impinged upon a production target, and since relatively little momentum in the direction transverse to the beam axis is transferred in the fragmentation process [87], most of the isotopes produced continue forward into the A1900 Fragment Separator [88]. A schematic of the ion source, coupled cyclotrons, and fragment separator can be found in Figure 4.1.

The ^{18}O primary beam used in experiment 08017 was fully ionized (charge state of 8+) and reached a final energy of 120 MeV/u. A Beryllium production target with a thickness of 1904 mg/cm^2 was used for fragment production.

4.1.3 A1900 Fragment Separator

The A1900 Fragment Separator consists of four dipole magnets and eight quadrupole triplets, and functions as a two-stage selection system. In the first stage, immediately following the production target, the first two dipole magnets are tuned to disperse particles according to their magnetic rigidity $B\rho$:

$$B\rho = p/q \; . \tag{4.1}$$

Here momentum $p = \gamma m/q$ where m refers to the mass of the particle, v the velocity, q the charge, and $\gamma = 1/\sqrt{1 - (v/c)^2}$ accounts for relativistic effects.

In the second selection stage, a wedge is placed in the path of the beam at the intermediate image point of the A1900 (see Figure 4.1). Particles passing through the wedge deposit energy according to the Bethe formula, shown here as given in Ref. [89]:

$$\frac{dE}{dx} = \frac{4\pi e^4 Z^2}{m_0 v^2} n_{abs} z_{abs} \left(ln\frac{2m_0 v^2}{I} - ln\left(1 - \frac{v^2}{c^2}\right) - \frac{v^2}{c^2} \right) \; . \tag{4.2}$$

Here e is the electronic charge, m_0 is the electron rest mass, Z and v refer to the atomic number and velocity of the beam particle, and n_{abs}, z_{abs}, I refer to the number density, atomic number, and average ionization potential of the absorber material, respectively. As it depends on Z^2, the energy lost by the beam introduces an elemental velocity shift. Therefore after passing through the wedge, as the beam particles traverse the remaining two dipole magnets, they are further dispersed according to their new $B\rho$ value. Following this second dispersion, slits located in the A1900 focal plane are closed to isolate the rare isotope of interest for further transmission.

This two-stage selection system is quite powerful, and in many cases the resulting "secondary beam" is nearly isotopically pure. For experiment 08017, a 405 mg/cm^2 Aluminum

wedge was placed at the intermediate image point, and the ^{12}B secondary beam selected was more than 99% pure, with small amounts of contamination from ^{9}Li and ^{11}Be. The beam rate was approximately three million particles per second. The total momentum spread of the beam was reduced to ± 0.25 % using slits placed at the Image 1 position, to allow for unobstructed transmission when dispersion-matching optical elements further downstream (see Section 4.2.1.1).

4.2 ^{12}Be Production and Measurement

The experimental end-station was located in the S3 vault of NSCL and consisted of the S800 Spectrograph [90], a large-acceptance, high-resolution magnetic spectrometer used for particle detection, and the Segmented Germanium Array (SeGA) [91], used to detect gamma rays. Both detection systems were needed to isolate ^{12}Be particles from other sources of background and to select the single-step, spin-transfer charge-exchange events discussed in Chapter 1 from those produced via other reaction mechanisms. The particle identification procedure and gamma analysis will be discussed in the following chapter - this section describes the technical details of particle and gamma ray detection.

4.2.1 S800 Spectrograph

4.2.1.1 Dispersion Matching

The ^{12}B secondary beam selected by the A1900 Fragment Separator was transported through the analysis line of the S800 Spectrograph (Figure 4.2). The analysis line consists of four dipole and five quadrupole triplet magnets, and has two modes of operation. To achieve

Focal Plane

———— Analysis Line ———— Spectrograph
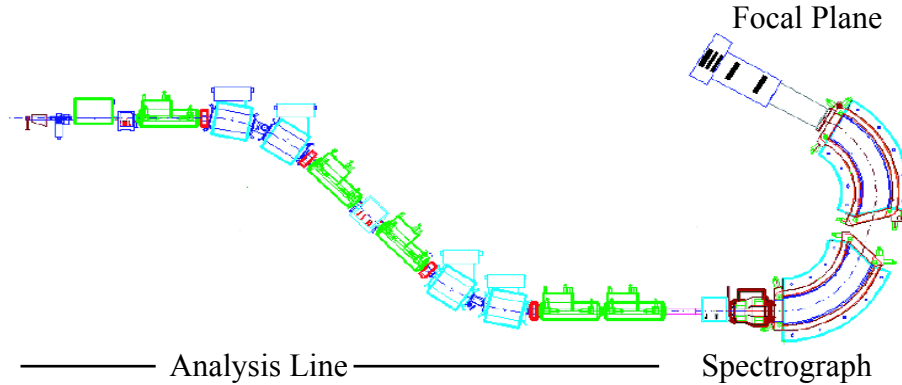
Figure 4.2: Schematic depicting analysis line and spectrograph components of S800 Spectrograph.

the maximum momentum acceptance ($\pm 2\%$), one can operate in focused mode, where the image at the focal plane of the spectrometer is chromatic, and the momentum resolution is determined by folding the intrinsic momentum spread of the beam with the momentum change induced by straggling in the target. This mode of operation provides no information about the incoming momentum of each particle however, and unless the momentum of each beam particle is tracked, the achievable energy resolution is limited to about 1 part in 1000.

Since the experimental method used for experiment 08017 relied solely upon the information from the spectrograph to identify ^{12}Be particles and reconstruct their energy on an event-by-event basis, it was imperative that the maximum energy resolution possible was achieved. Thus the second operation mode - dispersion matching mode - was employed, in which the entire system (analysis line and spectrograph) is tuned achromatically. As shown in Figure 4.3, in this mode the dispersion-matched spectrograph is set to compensate for the momentum dispersion of the beam on the target.

The physical principles of dispersion-matched optics can be described relatively simply if

one considers that in first order, the size of the beamspot at the target position of the spectrograph (s_{ta}) can be written in terms of the magnification (M_{AL}) and dispersion (D_{AL}) of the analysis line, the size of the beamspot at the object of the analysis line (s_0) and the dispersion of the beam itself (δ):

$$s_{ta} = M_{AL} * s_0 + D_{AL} * \delta \ . \tag{4.3}$$

Analogously, the size of the beamspot in the focal plane (s_{fp}) can be written in terms of the spectrograph magnification and dispersion (M_S and D_S):

$$s_{fp} = M_S * s_{ta} + D_S * \delta \ . \tag{4.4}$$

Substituting s_{ta} from Equation 4.3 into Equation 4.4, one can see the size of the beamspot in the focal plane factorizes into two terms: one depending on the object beamspot size and one depending on the dispersion of the beam:

$$s_{fp} = s_0(M_S * M_{AL}) + \delta(M_S * D_{AL} + D_S) \ . \tag{4.5}$$

For perfect dispersion matching, the size of the beamspot in the focal plane should be independent of the dispersion of the beam, requiring

$$D_{AL} = \frac{-D_S}{M_S} \ . \tag{4.6}$$

This can be checked using time-of-flight and position measurements during beam tuning, or by carefully adjusting the magnets to achieve the optimum resolution for a transition to a particular final state. For the S800 Spectrograph $D_S = -9.536$ cm/%, and $M_S = -0.892$, and the analysis line (in dispersion-matched mode) has a dispersion of $D_{AL} = -10.684$ cm/%, so Equation 4.6 holds to better than 0.1%.

The maximum energy resolution achievable also depends on the dispersion of the spec-
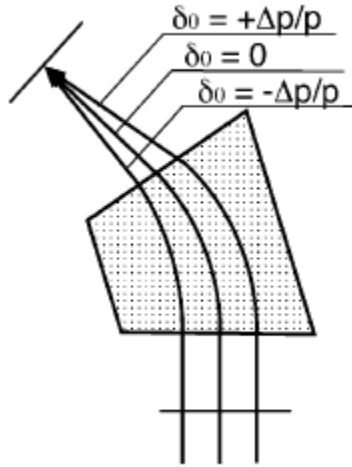
Figure 4.3: Cartoon depiction of lateral dispersion-matching, taken from Ref. [92]. Dispersion of rays with different momenta is compensated by the dispersion of the spectrometer.

trometer and the size of the beamspot at the object position:

$$R_E = \frac{\Delta E}{E} = \frac{2M_S * s_0}{D_S} \tag{4.7}$$

and so for an object beam spot size of 0.05 cm the maximum resolution achievable is 1/10,000. Since the momentum spread of the beam on the target is large in dispersion-matched mode ($D_{AL} = 10.684$ cm/%), the momentum acceptance was limited to $\pm 0.25\%$ to ensure unobstructed transmission of the beam through the beamline. This results in an approximately 5.25 cm tall beamspot on the target.

The target used in experiment 08017 consisted of ^{nat}Li (92.5% ^{7}Li and 7.5% ^{6}Li) and was placed at the pivot point of the S800. The final dimensions of the target were 3.81 cm (wide) by 5.08 cm (tall) by 104 μm (thick).The target was rolled to 5.5 mg/cm^2 (104 μm) from an original thickness of 10.68 mg/cm^2 (200 μm), and was kept in an oxygen-free environment prior to rolling to avoid oxidation. The rolling procedure itself took place in an argon gas environment, and the target was only exposed to air briefly while being placed at the pivot

point of the S800. Due to the short exposure time, oxygen contamination is not considered a significant concern for the experiment. A visual inspection of the target following removal from the beampipe supported this determination, as no discoloration due to oxidation was present. Even if minute quantities of oxygen were present, the large difference in Q-values for the ^{12}B(^{16}O, ^{16}F)^{12}Be reaction (Q=-27.125) and the ^{12}B(^{7}Li, ^{7}Be)^{12}Be reaction (Q= -12.569) would result in all ^{16}O events lying far outside of the excitation energy region of interest for the (^{7}Li, ^{7}Be) study (E_x(^{12}Be)= 0 - 3.169 MeV).

4.2.1.2   Focal Plane Detectors

Following interaction with the target, reaction residues were detected in the focal plane of the S800 [93], equipped with a suite of detectors to measure position, energy loss, and timing information.

The dispersive and non-dispersive positions of the particles were measured by two Cathode Readout Drift Counters (CRDCs) separated in the z (beam) direction by a distance of 1073 mm, as pictured in Figure 4.4. Each CRDC has an active area of 30 cm (in the non-dispersive/y direction) by 59 cm (in the dispersive/x direction) and an active depth of 1.5 cm. The detectors were filled with a mixture of 80% CF_4 gas and 20% C_4H_{10} gas at a pressure of 40.3 Torr. This gas mixture was chosen for its high drift velocity, slow aging characteristics and reduced probability of charge-spreading due to photon creation.

The dispersive position was determined by measuring the induced charges on the segmented cathode lead, integrated on each cathode pad for a finite amount of time following a trigger signal from the Data Aquisition System (DAQ). The center of gravity of the integrated charge distribution, shown in the inset of Figure 4.4, was taken to be the x-position of the event. In the non-dispersive direction the position was inferred from the time difference

(X2, Y2)

Event Trajectory

Central Ray

Integrated Image Charge

5000
4000
3000
2000
1000
0

Pad Number

(X1, Y1)
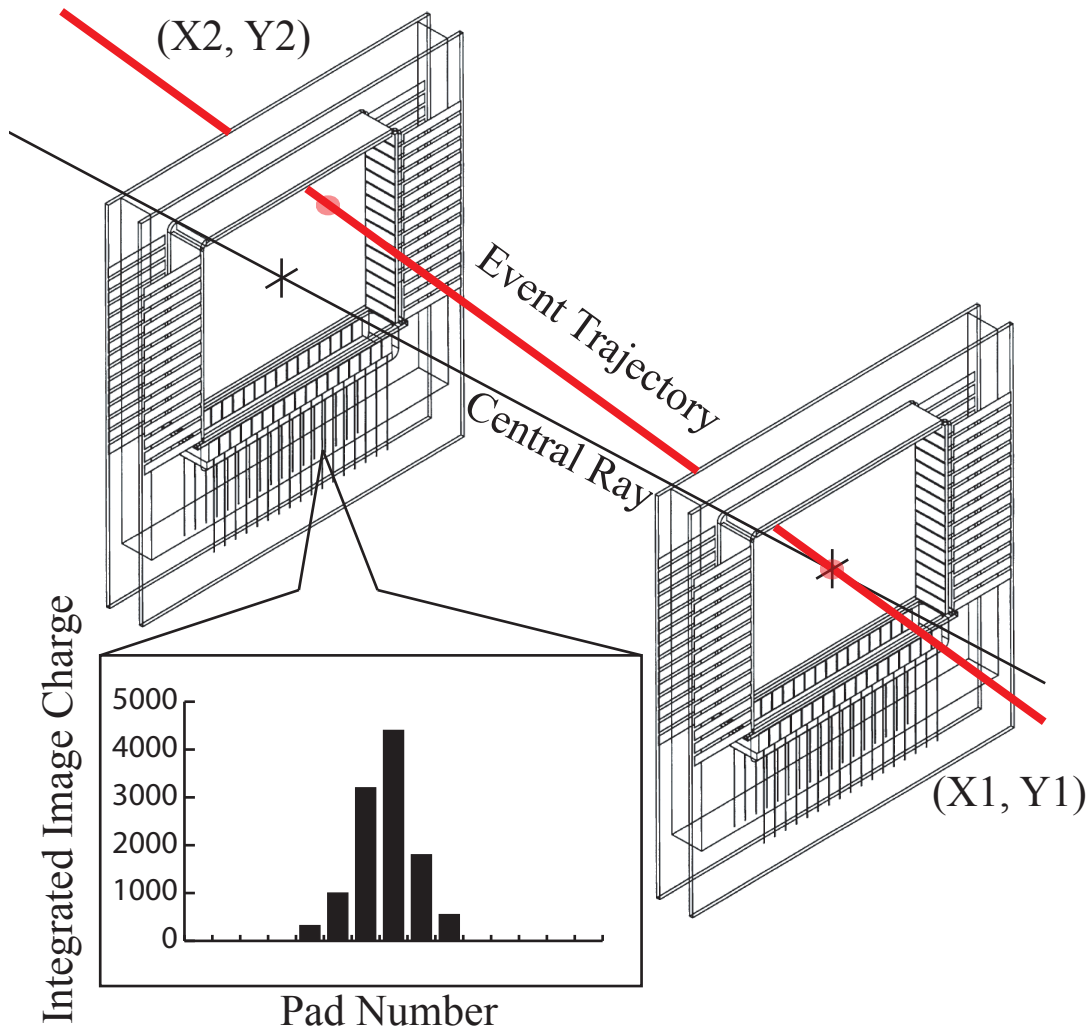
Figure 4.4: Layout of CRDC detectors and cartoon of cathode position determination. Figure taken originally from Ref. [93], modified by Wes Hitt in Ref. [94] .

between the DAQ trigger and the collection of secondary electrons on the anode wire of the CRDCs. The dispersive and non-dispersive angles were calculated by combining the position measurements from both CRDC detectors.

After passing through the CRDCs the particles entered an ionization chamber filled with P-10 gas (90% argon and 10% methane) at 140 Torr. There, direct ionization of the filling gas by the incident particles results in the creation of positive ion-electron pairs. The number of ion pairs produced is strongly correlated with the amount of energy deposited in the gas (energy deposition being governed by Equation 4.2) - on average, one ion pair is produced for every 25-35 eV of energy deposited. The precise energy-ion pair relationship depends on the nature of the incident radiation (velocity and charge) and the species of gas involved, but only weakly - empirical observations have shown the energy needed to create an ion pair is a remarkably constant parameter for many gases and radiation types [89]. Unfortunately, due to the combination of low atomic number for the incident particles ($Z(\mathrm{Be})$=4) and low density of absorber atoms in the fill gas (n_{abs} in Equation 4.2), very little energy was deposited by the reaction residues in the ionization chamber, and the energy loss information from the chamber was not used in the analysis of the experiment.

Upon leaving the ionization chamber the particles impinged upon a suite of plastic scintillator detectors, which provided energy loss, total energy and timing information. Unlike the gas-filled ionization chamber, the solid plastic scintillators had a much higher number density of absorber atoms, and the energy loss information provided by the scintillator suite was crucial for particle identification. In experiment 08017, only two of the scintillators in the focal plane were operational - a 3 mm thick detector attached to the back of the ionization chamber which provided the "start" signal for the DAQ, and a 5 mm thick detector

55

Light Output (% Anthracene)	65
Wavelength of Max Emission (nm)	423
Decay Constant (ns)	2.4
Attenuation Length (cm)	250
Refractive Index	1.581
H/C Ratio	1.103
Density	1.032
Softening or Flash Point (degrees C)	70

Table 4.1: Properties of Bicron^{TM} BC-400 Scintillators, as cited in Ref. [89]

further downstream. Both scintillators were made of commercially available Bicron^{TM} BC-400 plastic (C_9H_{10}), the properties of which are given in Table 4.1.

Charged particles passing through the scintillator deposit kinetic energy according to Equation 4.2, most of which is dissipated via lattice vibrations or heat. A small fraction however, is absorbed by the organic molecules in the scintillator material and excites the electron configuration into an excited state. Transitions back to the ground state configuration result in the emission of scintillation light, which occurs quickly - on the order of nanoseconds - and is therefore often referred to as prompt fluorescence. Each scintillator was equipped with photomultiplier tubes on top and bottom to measure the prompt fluorescence and output a voltage signal proportional to the energy deposited by the reaction residue.

4.2.1.3 Magnetic Field Corrections

Magnetic field aberrations for the S800 Spectrograph are largely due to the fringe fields of the two focusing quadrupole and two large dipole magnets. These aberrations are calculated and corrected for analytically, by modeling the fringe profiles with Enge functions of the form

$$E(z) = \frac{1}{1 + exp^{P(z)}} \quad . \tag{4.8}$$

These functions are fit to the measured magnetic field maps, with z being the direction of a reference path through the center of all magnets and $P(z)$ a fifth-order polynomial. The order is chosen so that the error in the correction is comparable to the resolution of the focal plane detectors of the S800 [90]. The fringe profiles are then input into the code COSY INFINITY [95], which calculates the aberrations, inverts the polynomial matrix and applies corrections event-by-event in the analysis software.

Another benefit of using this analytical approach is that the inverted matrix ("inverse map") can be used to relate the positions and angles measured in the focal plane to the position, energy, and angles at the target - a procedure known as "raytracing" which allows for easy reconstruction of kinematically relevant parameters on an event-by-event basis. In first order, the inverse map equation is:

$$
(dta, yta, ata, bta) = S^{-1}(xfp, yfp, afp, bfp)
$$

$$
= \begin{pmatrix} (dta|xfp) & (dta|yfp) & (dta|afp) & (dta|bfp) \\ (yta|xfp) & (yta|yfp) & (yta|afp) & (yta|bfp) \\ (ata|xfp) & (ata|yfp) & (ata|afp) & (ata|bfp) \\ (bta|xfp) & (bta|yfp) & (bta|afp) & (bta|bfp) \end{pmatrix} \begin{pmatrix} xfp \\ yfp \\ afp \\ bfp \end{pmatrix} \tag{4.9}
$$

where all "$-fp$" variables refer to the focal plane, and "$-ta$" variables refer to the target. x (a) refers to the dispersive position (angle) and y (b) refers to the non-dispersive position (angle). To deduce the energy at the target, one must assume the dispersive beam position at the object of the analysis line is zero, since 1) the entire spectrograph is tuned achromatically; and 2) the beam position in the dispersive plane at the object cannot be calculated. dta therefore refers to the fractional energy at the target:

$$
dta = \frac{E - E_0}{E_0} \, , \tag{4.10}
$$

with E_0 being the energy of a particle traveling along the central path of the spectrometer.

Clearly, the S800 Spectrograph is a powerful tool for particle detection and provides valuable information about the ^{12}Be particles produced in ^{12}B(^{7}Li, ^{7}Be) reactions. To ensure clean identification of charge-exchange events however, a secondary detection system is needed - SeGA.

4.2.2   Gamma Ray Detection

In the ^{12}B(^{7}Li, ^{7}Be)^{12}Be reaction, there are two distinct cases for which gamma-ray detection is relevant. First is the decay of the ^{7}Be recoil, which results in the emission of a 429 keV gamma ray and can be used as a "tag" for spin-transfer only charge-exchange events, as described in Chapter 1. Second is the in-flight decay of excited ^{12}Be particles, which emit gamma rays between 2 and 3 MeV. Detecting the gamma rays from both sources (^{7}Be and ^{12}Be) is important for the analysis and understanding of the data taken in experiment 08017, therefore this section will address not only the techical details of gamma ray detection but also the motivation for choosing SeGA as the detection system.

There are three mechanisms by which gamma rays (photons) interact with material: photoelectric absorption, Compton scattering and pair production. In photoelectic absorption, the photon interacts directly with an atom in the material, removing an electron from a bound atomic shell. The products of this interaction are therefore the electron (a.k.a. "photoelectron"), and an ionized absorber atom with an electron "hole" where the photoelectron was removed. This is the primary mode of interaction for gamma rays with relatively low energy (on the order of hundreds of keV). In Compton scattering, an incident photon is scattered from an electron in the material, yielding in a recoil electron with finite energy

and changing the energy and direction of the original photon. This is the primary mode of interaction for intermediate-energy gamma rays (hundreds of keV to several MeV). Finally, in pair production the incident photon has enough energy to produce an electron-positron pair (at least double the mass of the electron, or 1.022 MeV), and the subsequent annihilation of the positron results in the creation of two annihilation gamma rays with energies of 511 keV each. Pair production is the primary interaction mechanism for high-energy photons (several MeV and higher), and must take place while in the Coulomb field of the atomic nucleus. For all three processes, the probability of interaction increases with the atomic number of the absorber material - for photoelectric absorption and Compton scattering simply because there are more electrons present, and for pair production, because the Coulomb field of the nucleus is extended. For the gamma rays emitted in experiment 08017, from both the target recoil (^{7}Be) and in-flight (^{12}Be) sources, photoelectric absorption and Compton scattering are the dominant interaction mechanisms.

Depending on the source of the gamma ray being detected, there were two technical requirements for gamma ray detection in experiment 08017. For the photons emitted from ^{7}Be, it was important to achieve the maximum efficiency possible, to obtain maximum statistics for the coincidence data set (which requires both a ^{12}Be particle in the focal plane of the S800 *and* a 429 keV photon in the gamma ray detector). The ^{12}Be particles decaying in-flight however, required a detection system with good position resolution, capable of determining a precise angle for the emitted gamma ray. This angle is needed to correct the measured gamma ray energy $E_{\gamma,lab}$ for the Doppler-shift due to the motion of the particle when it emits the photon:

$$E_\gamma = \frac{E_{\gamma,lab}\left(1 - \beta \cos\theta\right)}{1 - \beta^2} \quad .$$

(4.11)

Here, E_γ is the Doppler-corrected energy of the gamma ray, θ is the angle between the emitted gamma ray and the emitting particle, and $\beta = v/c$, where v is the velocity of the emitting particle and c is the speed of light.

When experiment 08017 took place, there were two gamma detection systems readily available for use at NSCL. The Segmented Germanium Array (SeGA), which had been in use for several years, and a new Caesium Iodide Array (CAESAR) that had yet to be used in an NSCL experiment. When efficiency is a priority for gamma-ray detection, and optimal resolution is not required, inorganic scintillators similar to the sodium-doped caesium iodide (CsI(Na)) detectors in CAESAR are used. The density of the material and the relatively high atomic number of iodine ensures that a large fraction of all interactions are photoelectric absorption, and therefore the full photon energy is absorbed and most of the events lie under a clear "photopeak" located at the energy of the incident photon. However this efficiency comes at a price - the resolution of CsI(Na) detectors is approximately 7% for a 1 MeV gamma transition, whereas high-purity germanium detectors such as those in SeGA have intrinsic energy resolutions of just 0.2% at the same energy. Since both efficiency and resolution were priorities for experiment 08017, the decision of which detector array to use had to be carefully considered.

Fortunately, information was available from a previous (^{7}Li, ^{7}Be) charge-exchange experiment, which took place in February of 2007 and investigated the nucleus ^{34}Si [41]. In that experiment, many excited states in ^{34}Si were populated, resulting in a complicated gamma energy spectrum with several photopeaks and Compton edges (lower-energy shoulders indicating incomplete photon energy deposition) contributing to a large continuum at low energies. Were it not for the excellent resolution of the SeGA detectors used in that

experiment, it would have been difficult to identify the 429 keV transition from the continuum and isolate the spin-transfer charge-exchange events. Furthermore, it would have been nearly impossible to perform a Doppler correction and decompose the gamma energy spectrum, since the segmentation of SeGA greatly improves the angular resolution, as described in further detail below. Unsure of whether resolution would play such a significant role in the analysis of expeirment 08017, it was decided to err on the side of caution and employ the germanium array again. To maximize efficiency however, the detectors were placed in a closely-packed configuration near the target, known as Barrel SeGA.

4.2.2.1   Barrel SeGA

As previously mentioned, the SeGA array was chosen as the gamma detection system for experiment 08017 due to its superior energy resolution (as compared to inorganic scintillators such as CsI(Na)). The excellent resolution of germanium detectors can be attributed largely to the response of the material after interaction with a photon. Reminiscent of the ion pairs produced in ionization chambers (described in Section 4.2.1.2), when incident gamma radiation interacts with germanium of semiconductor purity, the energy deposition leads to the creation of electron-hole pairs, caused by excitation of electrons from the valence band to the conduction band. These electron-hole pairs can be guided through the material and collected using an electric field, and the number of pairs created corresponds to the energy deposited in the material. Since semiconductor detectors have small ionization energies (around 3 eV), more charge carriers are created per unit of energy deposited than for gas chambers or scintillating materials.

Additionally, semiconductors can be "doped" with small concentrations of impurities,

which have excess electrons (n-type semiconductors) or holes (p-type semiconductors) compared to the pure semiconductor material. Since the SeGA detectors are n-type semiconductors, we will only describe those here - a complete description of semiconductors and doping is given in [89]. In an n-type superconductor, the addition of an impurity results in an excess of electrons, left after covalent bonds are formed between the impurity and pure atoms. These electrons are very lightly bound to the lattice, and therefore can be easily knocked into the conduction band. The added concentration of electrons in the conduction band increases the rate of electron-hole recombination, altering the equilibrium between electrons and holes and ultimately increasing the total number of charge carriers.

The increased number of charge carriers (as compared to gas chambers and scintillating materials, as well as un-doped semiconductors) has two beneficial effects on the energy resolution [89]: the greater amount of charge per pulse raises the signal/noise ratio, the most important contribution to the resolution at low energies; and the statistical fluctuation in the number of charge carrier pairs per pulse decreases with more charge carriers produced, the most important contribution to the resolution at medium-high energies. However, because of the small band gap in germanium (0.7 eV), the detectors must be cooled to liquid nitrogen temperatures to reduce thermal excitations from the valence to the conduction band, a source of noise that would spoil their excellent energy resolution.

Until now, all mention of resolution has referred to the intrinsic resolution of the germanium detectors. One of the main advantages of using SeGA however, is a significant improvement in the Doppler-corrected energy resolution due to the detector design. Each SeGA detector is a coaxial germanium crystal, with an external diameter of 7 cm and length of 8 cm, electronically segmented into eight 1 cm wide disks along the cylinder axis and

four radial segments perpendicular to the cylinder axis [91]. Since the Doppler-corrected energy resolution depends on three factors - the intrinsic energy resolution of the germanium detector (ΔE_{intr}), the uncertainty in the source velocity due to the slowing down of the projectile in the target ($\Delta\beta$), and the uncertainty in the emission angle of the gamma ray due to the finite opening angle of the gamma-ray detector and ambiguity in the angle of the scattered particle ($\Delta\theta$) - the 32-fold segmentation of the SeGA crystals (and the resulting reduction of $\Delta\theta$ for each gamma ray event) significantly improves the Doppler-corrected energy resolution compared to non-segmented detectors.

For experiment 08017 SeGA was employed in Barrel configuration to optimize efficiency while maintaining adequate energy resolution. Barrel SeGA consists of 15 Germanium crystals arranged in two concentric rings around the target, as shown in Figure 4.5. The forward/downstream ring has one less detector than the backward/upstream ring due to space limitations at the target position of the S800 Spectrograph. The large opening angle coverage and closely-packed arrangement of the Barrel SeGA configuration results in a source efficiency of approximately 11.75% for 429 keV gamma rays (see Section 5.1.2.1 for details of efficiency measurement). However, despite the segmentation of the individual detectors, due to the 5 cm tall beamspot incident on the target in experiment 08017 and the close proximity of the detectors to the target, the angle ambiguities were still quite large, and the Doppler reconstructed energy resolution was limited. Details of the Doppler reconstruction for experiment 08017 can be found in Section 5.1.2.2.

Beam Line

Secondary Beam
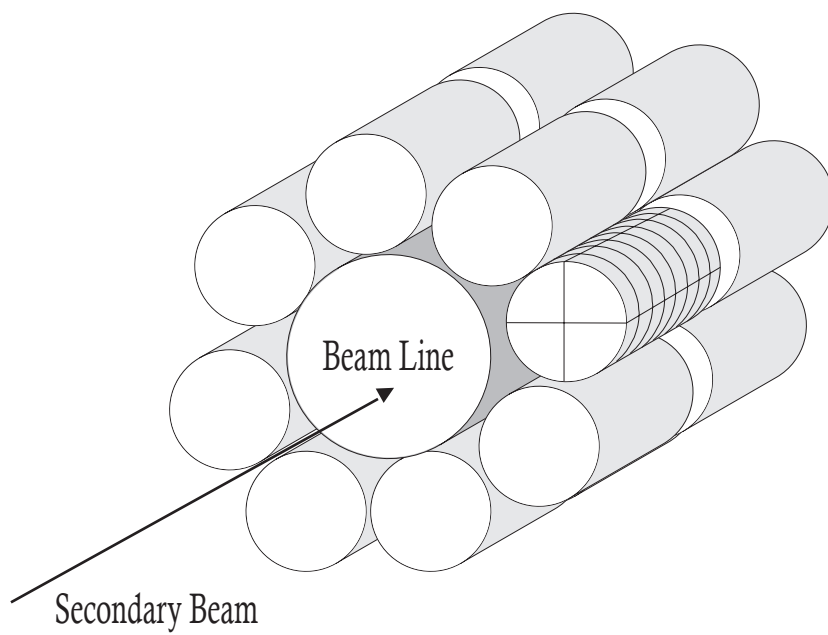
Figure 4.5: Cartoon of Barrel SeGA configuration. Figure modified from Ref. [96].

Chapter 5

Data Analysis

This chapter outlines the transformation from raw experimental observables to calibrated physical quantities, such as excitation energy, scattering angle and differential cross-sections. The analysis was carried out with a combination of three programs: NewSpecTcl [97], an object-oriented C++ framework used mainly for online analysis; tv [98], used solely for fitting gamma peaks in calibration source spectra; and Physics Analysis Workstation (PAW) version 2.14/04 [99], a Fortran based analysis program that executes elementary operations on data using user-defined subroutines. The analysis procedure is divided into four stages: calibrations, describing separately S800 and SeGA calibrations; particle identification, i.e. isolation of ^{12}Be events; reconstruction of the ^{12}Be excitation energy spectrum; and cross-section calculations.

5.1 Calibrations

5.1.1 S800 Calibrations

As described in Chapter 4, two Cathode Readout Drift Counters (CRDCs) were used to determine the positions and angles of reaction products in the focal plane of the S800. Since these positions and angles were ultimately used to reconstruct the excitation energy and scattering angle immediately following the reaction, it is important that the CRDC detectors be carefully calibrated. Since the position measurement can shift over time, three CRDC calibrations were performed during experiment 08017: before the first ^{12}Be production run, during the middle of the experiment after a short facility breakdown, and at the end of the ^{12}Be production period. The CRDC calibration information allows one to reliably combine position data from production runs taken at different times during the experiment.

To perform the CRDC calibration, a Tungsten plate with a well-defined pattern of slits and holes (see Figure 5.1) was inserted remotely into the path of the beam upstream of each CRDC. Particles passing through the plate were detected in the CRDC, leaving an imprint of the plate design on the position spectrum of the detector. A sample imprint from a CRDC calibration run is shown in Figure 5.2 - comparing with Figure 5.1, the hole and slit pattern of the Tungsten plate is visible.

First-order polynomials were used to relate the channel number from the data stream (units of pad, ns) with a physical position (units of mm)

$$x_{1,2}(mm) = m_{1,2}(mm/pad) \times x_{1,2}(pad) + b_{1,2}(mm) \tag{5.1}$$

$$y_{1,2}(mm) = n_{1,2}(mm/ns) \times y_{1,2}(ns) + c_{1,2}(mm) \ . \tag{5.2}$$
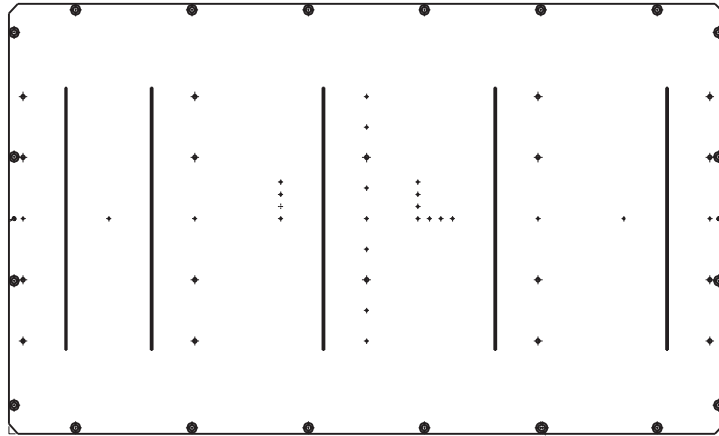
Figure 5.1: Diagram depicting hole and slit pattern of CRDC masks.
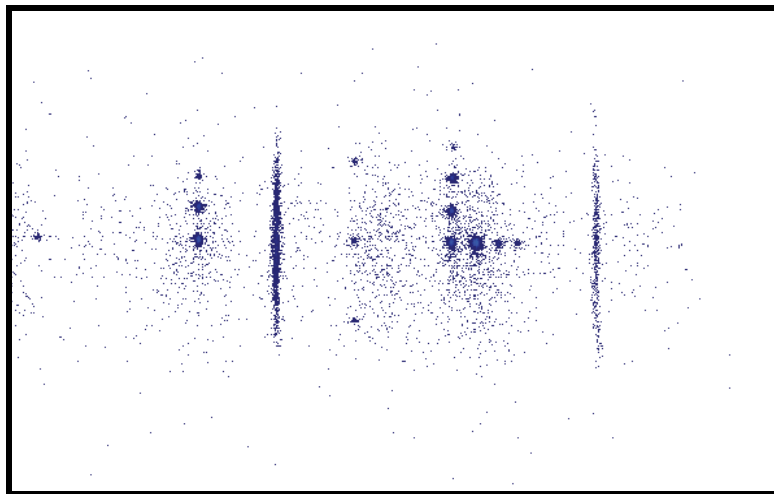
Figure 5.2: Sample spectrum from CRDC2 mask run taken during experiment 08017.

m_1	b_1	m_2	b_2	n_1	c_1	n_2	c_2
2.54	-279.628	2.54	-278.495	-0.068	138.821	0.070	-142.595

Table 5.1: Mask calibration parameter values obtained from first CRDC calibration run of experiment 08017.

This was done separately for each CRDC. In both directions, the offsets $b_{1,2}$ and $c_{1,2}$ were set such that the vertex of the "L" shape seen in Figure 5.1 was located at 0 mm. In the x-direction, where the position is determined from a charge induced on the segmented cathode pads, the slope $m_{1,2}$ was fixed by the geometry of the detector to 2.54 mm/pad. In the y-direction, the slope $n_{1,2}$ depended on the drift velocity of the electrons to the anode wire. The drift velocity depends upon the gas composition and pressure, as well as other parameters that can vary during the course of one experiment. Fortunately, in experiment 08017, $n_{1,2}$ did not change much between each calibration run, indicating that the CRDC environment was stable and a single mask calibration could be applied to all production runs. Therefore, the first calibration was used as a reference and small corrections to x and y were performed on a run-by-run basis. The mask calibration values adopted are given in Table 5.1.

Run-by-run corrections of x and y were performed using the ^{12}B(4+) charge-state, produced when fully ionized ^{12}B beam particles capture electrons from target atoms. Compared to nuclear charge-exchange, the atomic charge-exchange process does not involve significant energy and momentum transfer, so the charge-state measured in the focal plane of the spectrograph designates the beam axis to high accuracy and provides information about properties such as the angular spread of the incoming beam. For each production run, the x and y positions of the charge-state were shifted such that the average position for each run

Parameter	Definition
xfp	x_1^c
yfp	y_1^c
afp	$(x_1^c - x_2^c)/d$
bfp	$(y_1^c - y_2^c)/d$

Table 5.2: Definitions of focal plane position and angles used in Equation 4.9. c superscripts refer to corrected and calibrated parameters, and d is the distance between the two CRDC detectors in the focal plane (1073 mm).

matched that of the first production run after the initial mask calibration. This correction resulted in significantly improved position resolution when production runs were combined.

After completing mask calibrations and run-by-run corrections, it was possible to define the positions and angles in the focal plane $(xfp, yfp, afp, bfp$, in Equation 4.9) that will be "raytraced" back to the target position. The definitions of these parameters are given in Table 5.2.

5.1.2 SeGA Calibrations

5.1.2.1 Source Calibrations

To calibrate the absolute energy and efficiency of the SeGA detectors, measurements were taken with gamma-ray sources ^{152}Eu and ^{226}Ra before and after the experiment. Each source was placed at the target position, 1.75 cm upstream of the center of the detector array, for one hour. The calibration spectra were analyzed using the program tv [98].

For each of the 15 SeGA detectors, the photopeak of the transitions listed in Table 5.3 were fit with a Gaussian function atop a linear background. The centroid from the fit was taken as the channel number for that gamma-ray transition. The energy of the transition

Source	γ transitions used in calibration (keV)
^{152}Eu	224.7 344.3 411.1 444.4 778.9 867.4 964.1 1112.1 1212.9 1299.1 1408.0
^{226}Ra	186.2 241.9 295.2 351.9 609.3 665.5 768.4 806.2 934.1 1120.3 1238.1
	1280.9 1377.7 1509.2 1661.3 1729.6 1764.5 1847.2 2118.5 2204.1 2447.7

Table 5.3: Gamma transitions used for energy and efficiency calibrations.

was then assumed to be quadratically related to the channel x:

$$E_\gamma = a_0 + a_1 x + a_2 x^2 \ . \tag{5.3}$$

The calibration coefficients (a_0, a_1, and a_2) were chosen to minimize the χ^2 of the calculated and known energies:

$$\chi^2 = \sum \frac{(E_\gamma - E_{known})^2}{\sigma^2} \ , \tag{5.4}$$

where σ is the error associated with the peak fit. As shown in Figure 5.3, the ^{152}Eu and ^{226}Ra calibrations for data taken before and after the experiment are in good agreement. Since the ^{152}Eu source has transitions in the immediate vicinity of the 429 keV ^{7}Be 'tag', the calibration coefficients obtained using this source were applied to all subsequent gamma analyses.

For the efficiency calibration, the detectors were split into two groups based on their position relative to the target/source position - "downstream" detectors occupying the ring closest to the spectrograph, and "upstream" detectors occupying the ring closest to the analysis line. The efficiency of each group was calculated using the number of counts in the photopeak N_γ, the activity of the source A, the duration of the calibration run t adjusted for the DAQ deadtime, and the emission probability for the specific transition (ϵ_{emit}, taken
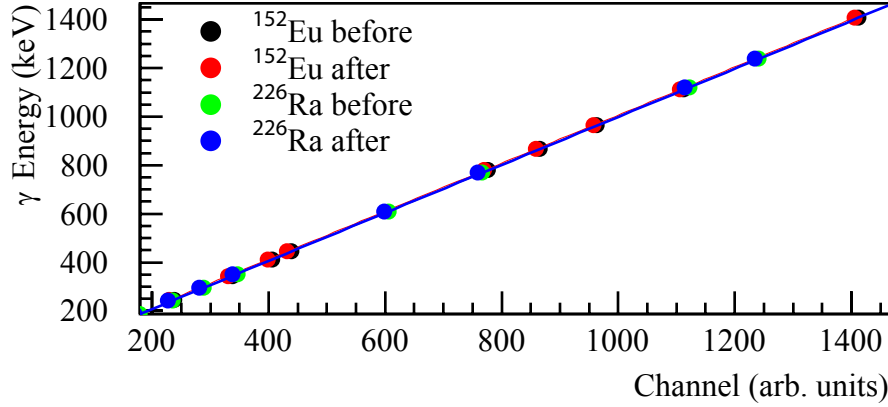
Figure 5.3: Channel-Energy relationship and fits for ^{152}Eu and ^{226}Ra calibrations, taken before and after the experiment.

from [100]):

$$\epsilon(\%) = \frac{N_\gamma}{A \times t \times \epsilon_{emit}} \times 100 \ . \tag{5.5}$$

The efficiency is plotted as a function of the gamma-ray energy for both sources in Figure 5.4. The absolute radioactivity of the ^{152}Eu source was known, as the activity was measured to be 8.46 μCi on May 1, 1978 and ^{152}Eu has a well-established half-life of 13.537 $\pm$ 0.006 years. The absolute activity of the ^{226}Ra source was not known to such high accuracy, so a common scaling factor was applied to the entire efficiency curve to ensure agreement with the ^{152}Eu values in the energy region for which the two sources overlap. To estimate the efficiency for the 429 keV ^{7}Be transition, the ^{152}Eu total efficiency curve was fit with the power-law function

$$\epsilon(E_\gamma) = 749.01 E_\gamma^{-0.685} \ , \tag{5.6}$$

shown as the solid line in Figure 5.4. Based on this fit, the calculated efficiency for the 429 keV ^{7}Be transition was 11.75% $\pm$ 0.05%.
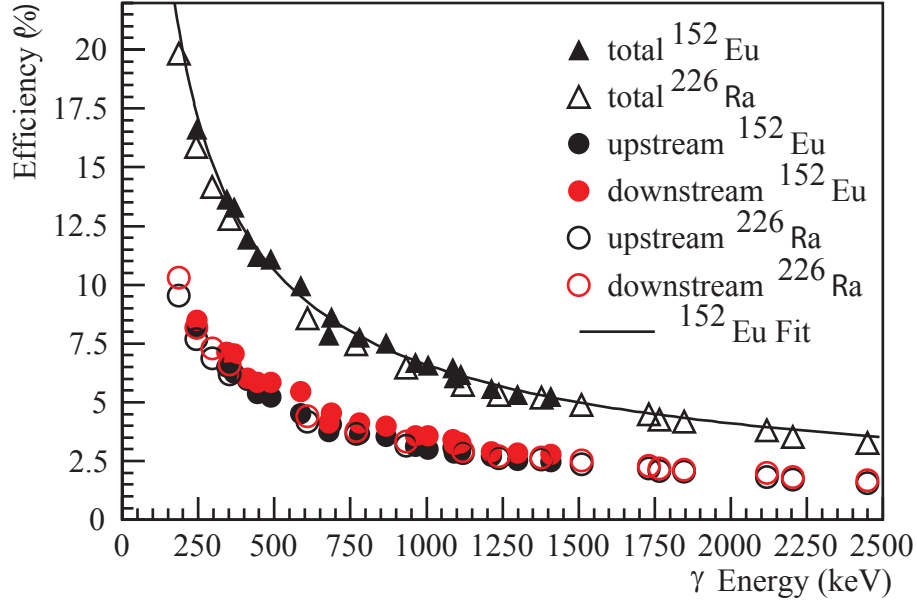
Figure 5.4: Efficiency curves for ^{152}Eu and ^{226}Ra calibration source measurements.

5.1.2.2 In-Flight Calibrations

The ^{12}Be particles exiting the target in experiment 08017 were traveling at approximately 38% of the speed of light. The gamma rays emitted from the moving particles were Doppler shifted in the laboratory frame: for forward (backward) angles, the measured energies were higher (lower) than in the projectile frame. Since the energy in the projectile frame characterizes the nuclear transition, the energies measured with SeGA must be Doppler-corrected through Equation 4.11 to be physically meaningful.

Due to the large beamspot ($\sim$5.25 cm) and close-packed configuration of the detectors, the Doppler-corrected energy resolution was dominated by uncertainties in θ, the detection angle of the gamma ray in the laboratory frame. To mediate this uncertainty, 1.75 hours of data were taken with the spectrograph set to detect ^{11}Be particles. Using the well-known 320 keV transition in ^{11}Be, it was possible to tune the position of the 420 SeGA segments and reduce angle ambiguities. As shown in Figure 5.5, even without tuning the segment

72
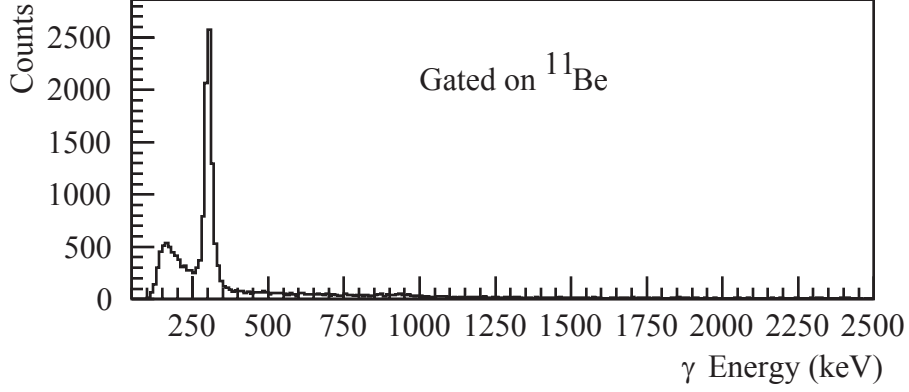
Figure 5.5: Doppler-corrected gamma energy spectrum, gated on ^{11}Be and including all 15 SeGA detectors.

position the 320 keV transition can be clearly identified in the Doppler-corrected gamma energy spectrum.

The $\cos\theta$ in Equation 4.11 depends on all three cartesian coordinates. To simplify the segment position calibration, the x- and y-positions of the segments were assumed to be in exact agreement with those in the "angle file", which defines initial x, y, and z positions for each segment in the Barrel SeGA configuration relative to a target placed at the exact center of the array. Then, an "effective" z-position was calculated for each segment using Equation 4.11, by first calculating the segment angle that would be necessary to force the observed peak in the ^{11}Be spectrum ($E_{\gamma,lab}$) to exactly 320 keV ($E_\gamma = 320$ keV)

$$\cos\theta = \frac{1}{\beta}\left(1 - \frac{320}{(1-\beta^2)E_{\gamma,lab}}\right) \quad , \tag{5.7}$$

then calculating the z-position associated with this "effective" segment angle

$$Z_{\gamma,eff.angle} = \sqrt{\frac{x^2+y^2}{\tan\theta}} \quad . \tag{5.8}$$

A plot of the "effective" z-position $Z_{\gamma,eff.angle}$ vs. the z-position provided by the original angle file $Z_{\gamma,anglefile}$ is shown in the top panel of Figure 5.6. If the segment positions in

73
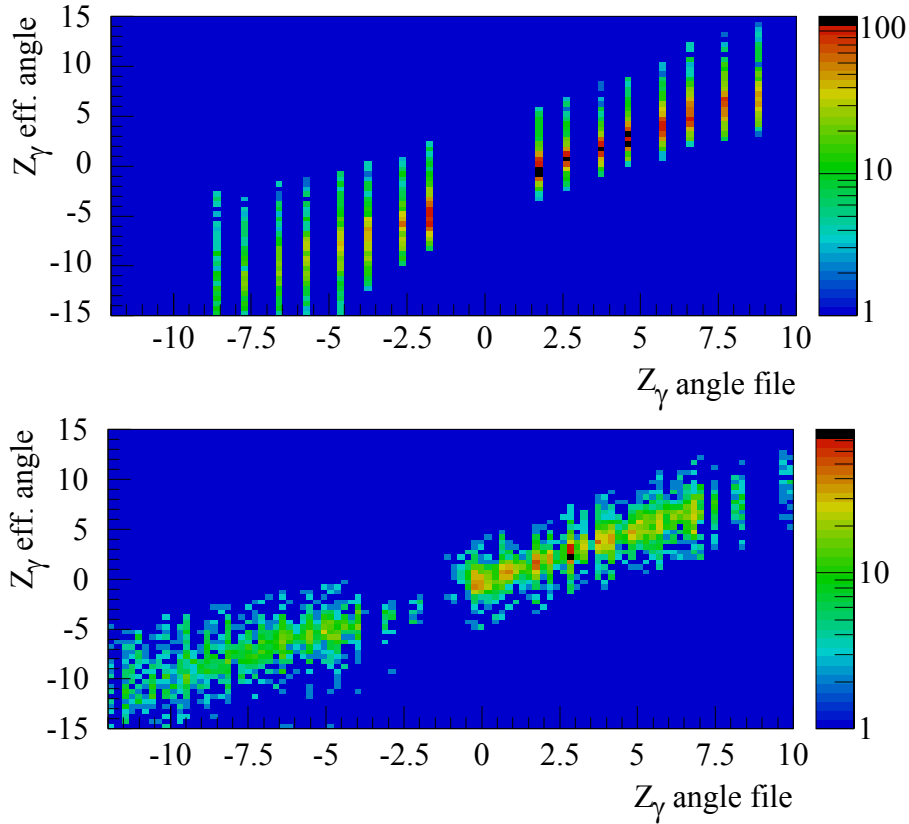
Figure 5.6: "Effective" vs "angle file" z-positions of the 420 segments in the Barrel SeGA array. (Top) Before any position corrections were applied; (Bottom) after position corrections were applied.

the angle file were optimized, this plot would show a line with a slope of unity, with uniform vertical width caused by the size of the beamspot and the finite angular coverage of each segment. Comparing the top panel of Figure 5.6 (before position corrections) to the lower panel (after position corrections were applied) it is clear that the correction procedure results in effective segment positions that more closely resemble the optimization criteria.

To illustrate the corrections applied, spectra before (a,b) and after (c,d) corrections are shown for a single detector in Figure 5.7. Plotted is the *difference* between the "effective" and "angle-file" segment z-positions, henceforth referred to as Z_{diff}. A shift of Z_{diff} of -0.1 cm corresponds to shifting the centroid of the (Doppler-corrected) 320 keV peak by 1
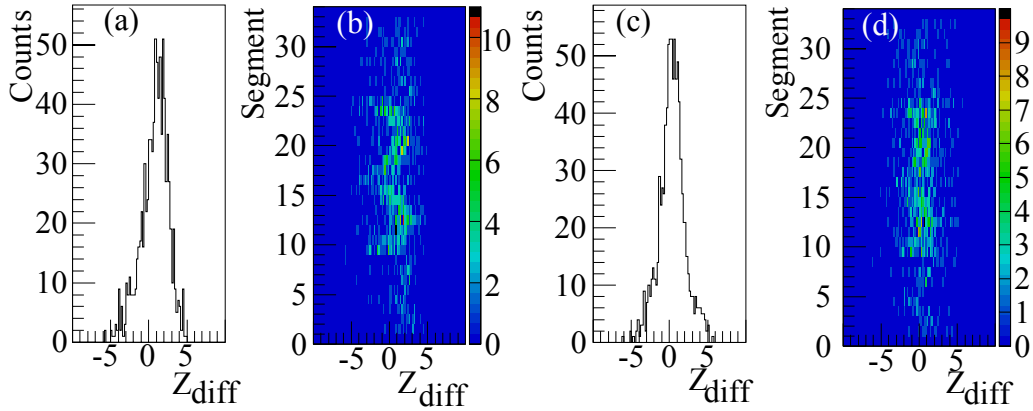
Figure 5.7: Difference between "effective" and "angle file" z-positions, detector 9. (a) Entire detector, prior to corrections; (b) as a function of segment number, prior to corrections; (c) entire detector, after corrections were applied; (d) as a function of segment number, after corrections were applied.

keV. The detector shown is an example of a worst-case scenario - one of three detectors (of fifteen in the array) that required corrections of this magnitude.

Evident in Figure 5.7 (b) is a correlation between Z_{diff} and segment number. This is likely due to the low-energy gamma ray used in the correction procedure. The interaction length in Germanium for a 320 keV photon is approximately 2 cm [101]. The 320 keV gamma rays emitted by ^{11}Be therefore tend to deposit their full energy in the SeGA segments segments closest to the target, skewing the angles observed.

To summarize, small shifts to the effective z-positions of SeGA segments were made using the 320 keV transitions in ^{11}Be as a reference. The magnitude and direction of the shifts were determined by grouping segments together (to aggregate sufficient statistics), and then comparing the z-position calculated from the Doppler-shift of the 320 keV line with the z-position assumed by the gamma angle file. The corrected segment positions reflect *effective angles* for each segment, rather than physical positions. Using these effective angles, the final Doppler-reconstructed energy resolution for the 320 keV transition in ^{11}Be was roughly 7%.

However, since the angle corrections applied depend on the interaction length of the gamma rays in Germanium, and the interaction length is highly energy-dependent, the Doppler-reconstructed energy resolution for the $\sim$2 MeV gamma transitions in ^{12}Be was estimated to be worse - approximately 10% - although making a precise estimate was difficult due to extremely low statistics.

5.2 Particle Identification

The ^{12}B secondary beam used in experiment 08017 was more than 99% pure, containing small amounts of ^{9}Li and ^{11}Be. The ^{nat}Li target consisted of 92.5% ^{7}Li and 7.5% ^{6}Li, and was mounted on a circular plastic frame. Considering the large beamspot, it is probable that some of the beam particles interacted with the frame as well as the target. It is likely therefore, that in addition to the ^{12}B(^{7}Li, ^{7}Be)^{12}Be reaction of interest, several other reaction channels involving the beam and/or target contaminants, or reactions on the target frame, were also populated during the experiment. Fortunately, by first tuning the spectrograph to transport only particles with magnetic rigidities comparable to those of the ^{12}Be charge-exchange ejectiles to the focal plane, and then exploiting energy loss, timing, position, and angle measurements, it was possible to isolate the ^{12}Be particles of interest from other reaction products and contaminants.

The majority of the reaction products from non-charge-exchange channels did not make it into the focal plane due to momentum selection in the S800 ($B\rho$ =3.928 Tm, corresponding to a central-ray energy of 949.96 MeV for ^{12}Be). Based on the magnetic rigidity setting of the analysis line, the ^{12}B beam energy was 959.96$\pm$4.8 MeV. The ground-state Q-value for the ^{12}B(^{7}Li, ^{7}Be)^{12}Be reaction is -12.56 MeV, so the maximum possible energy for

^{12}Be(g.s.) particles produced in this reaction would be 952.20 MeV. The energy acceptance of the spectrograph is 10%, so the range of ^{12}Be energies accepted were 895.47 MeV to 999.81 MeV, which would correspond to ^{12}Be excitation energies up to $E_x =50$ MeV. Since the experiment was only able to resolve to states below the neutron decay threshold in ^{12}Be ($E_x =3.169$ MeV), this energy range encompassed the entire region of interest for experiment 08017.

Recall that the plastic scintillators of the focal plane measure both timing information (time-of-flight TOF, relative to the RF of the cyclotron) and energy-loss information (ΔE). The TOF allows for velocity determination, which combined with Equation 4.1 provides information about the mass-to-charge ratio of the detected species. ΔE is directly correlated to the atomic number Z of the particle, as shown in Equation 4.2. Combined, these two measurements provide all the information needed for unambiguous particle identification, and the ΔE - TOF two-dimensional spectrum is therefore often referred to as a PID (Particle IDentification) plot.

Figure 5.8 shows the PID plot for experiment 08017. In the top panel is the raw data, without any corrections applied. Four cyclotron RF cycles are visible, centered at -1500, -1050, -600 and -150. Since each cycle contains the same reaction products, in the center panel these cycles were combined for ease of viewing and to aggregate statistics. In the bottom panel, corrections have been applied to TOF and ΔE for optical and detector-dependent effects. The TOF corrections account for particles of the same species that have slightly different flight paths through the spectometer. The ΔE corrections account for the β-dependencies of the Bethe formula (Equation 4.2).

It is worth noting that this PID plot is significantly less resolved than most others ob-
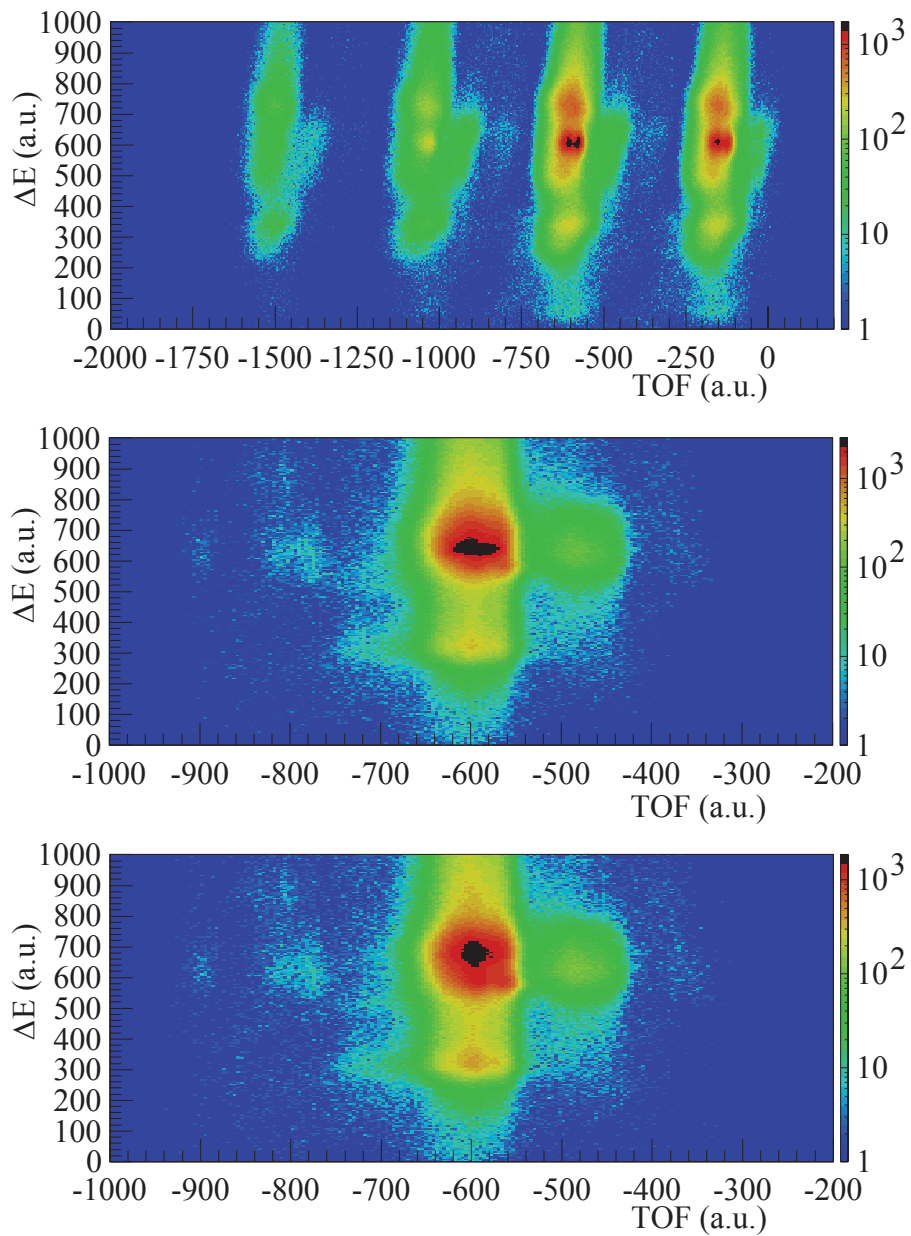
Figure 5.8: (Top) Raw (uncorrected) PID plot for experiment 08017. (Center) PID after four RF cycles have been collapsed. (Bottom) PID after TOF and ΔE corrections have been applied.

tained in NSCL experiments. Since this experiment involved relatively light particles (A=12, whereas most NSCL experiments involving the S800 spectrograph measure A=30-70) the signals from the ionization chamber were not sufficient for ΔE determination, resulting in poor PID resolution. Currently a high-pressure ionization chamber is installed in the S800 focal plane, which has capabilities for lower-mass ΔE measurements. Had this detector been available for experiment 08017, a cleaner PID plot would likely have been possible.

By far, the strongest feature in the PID plot is the ^{12}B(4+) charge-state (TOF$\sim$ -600, $\Delta E \sim 675$). Although useful for calibration purposes, the presence of the charge-state in the PID plot can obscure the charge-exchange events. Traditionally, once the PID plot has been corrected, the charge-state is removed and the particle of interest becomes clearly visible. Unfortunately, in experiment 08017 there was a significant contaminant of unknown origin overlapping with ^{12}Be in the PID plot. Utilizing the full focal plane detector suite and information from SeGA (to identify charge-exchange events) it was possible to create a master gate that consisted primarily of ^{12}Be particles. The limits imposed in this master gate are shown in Table 5.4 and the gate has been applied on the final PID plot shown in Figure 5.9. Examples of the separation possible using this gate and the removal of any remaining background contamination are discussed in the following section.

5.3 Excitation Energy Reconstruction

From the reconstructed energies (dta), and angles (ata, bta) one can determine the excitation energy of ^{12}Be and the scattering angle. The excitation energy was calculated via a missing mass calculation. In the following derivation, the speed of light has been set to 1.

The missing mass is found using the missing energy and missing momentum after recon-

Purpose	Signal	Good Event Gate
Charge-state removal	xfp	xfp < -0.033 AND xfp > -0.02
Background removal	TOF	-620 < TOF < -570
Background removal	ΔE_1	440 < ΔE_1 < 640
Background removal	xfp	xfp > -0.1
Background removal	CRDC1(2) anode	(a1+a2) > 3500 OR
		a1 < 4000 OR a2 < 4000 OR
		a1 > 1500 OR a2 > 1500
Background removal	ΔE_2	700 < ΔE_2 < 900
Background removal	All ΔE	$\Delta E_2 \times \dfrac{\Delta E_1}{500} \times \dfrac{(a1+a2)}{4400} \times \dfrac{IC}{100} > 750$

Table 5.4: Gates applied to remove charge-state and background contamination from PID.
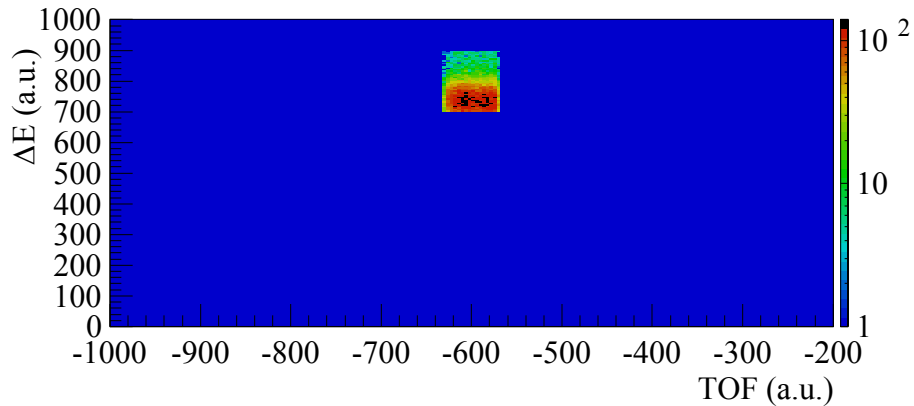
Figure 5.9: PID with master gate applied.

struction:

$$m_{miss} = \sqrt{E_{miss}^2 - p_{miss}^2} \qquad (5.9)$$

and the excitation energy is determined by accounting for the mass of the recoil

$$E_x(^{12}\text{Be}) = m_{miss} - m(^7\text{Be}) \ . \qquad (5.10)$$

For the coincidence case (a ^{12}Be particle detected in the S800 is measured in coincidence with a 429 keV gamma ray detected in SeGA), the recoil excitation should also be subtracted from the missing mass. However, since for the higher-statistics singles data (S800 events only) it is impossible to disentangle excitations through the ground state of ^{7}Be from those through the 429 keV state, the recoil excitation was not explicitly included in the missing mass calculation. The end result is that for the coincidence data the ^{12}Be ground-state calculated via the missing mass calculation will be shifted to 429 keV (rather than zero). For the singles data, there is a 429 keV ambiguity resulting from the population of both states below the neutron threshold in ^{7}Be. Considering each of the terms in Equation 5.9:

- The missing energy is the excess energy in the ^{12}B(^{7}Li, ^{7}Be)^{12}Be reaction:

$$E_{miss} = E_k(^{12}\text{B}) + m(^{12}\text{B}) + m(^7\text{Li}) - E_k(^{12}\text{Be}) - m(^{12}\text{Be}) \ , \qquad (5.11)$$

where E_k refers to kinetic energy. $E_k(^{12}\text{B})$ was estimated using the program LISE++ [102] and then calibrated such that the ground-state of ^{12}Be in the singles data set was centered at 0 MeV. $E_k(^{12}\text{Be})$ was calculated on an event-by-event basis using the energy of a central ray through the spectrograph E_0 (calculated in LISE++ using the Bρ setting of the S800) and the raytraced fractional energy dta:

$$E_k(^{12}\text{Be}) = E_0(1 + dta) \ . \qquad (5.12)$$

81

All masses were taken from Ref. [103].

- The missing momentum is found by first calculating the magnitude of the beam and ejectile momenta from their respective kinetic energies and masses

$$p = \sqrt{E_k^2 + 2E_k m} \ . \tag{5.13}$$

Then, defining the beam axis as the z-axis, the cartesian components of the incoming beam momenta are given by

$$
\begin{aligned}
p_x(^{12}\text{B}) &= 0 \\
p_y(^{12}\text{B}) &= 0 \\
p_z(^{12}\text{B}) &= p(^{12}\text{B}) \ .
\end{aligned}
\tag{5.14}
$$

The outgoing ^{12}Be momenta are found using the raytraced dispersive and non-dispersive angles

$$
\begin{aligned}
p_x(^{12}\text{Be}) &= p(^{12}\text{Be}) \times \sin ata \\
p_x(^{12}\text{Be}) &= p(^{12}\text{Be}) \times \sin bta \\
p_z(^{12}\text{Be}) &= \sqrt{p^2(^{12}\text{Be}) - p_x^2(^{12}\text{Be}) - p_y^2(^{12}\text{Be})} \ ,
\end{aligned}
\tag{5.15}
$$

and then since the x- , y- and z- components of the incoming and outgoing momenta are known, the components of the *missing* momenta can be found by subtraction:

$$p_{x,y,z}^{miss} = p_{x,y,z}(^{12}\text{B}) - p_{x,y,z}(^{12}\text{Be}) \ . \tag{5.16}$$

Calculating the scattering angle in the laboratory frame is simple by comparison:

$$\Theta_{lab} = \sqrt{ata^2 + bta^2} \ . \tag{5.17}$$

The excitation energy of ^{12}Be obtained from the missing-mass calculation is shown in the top panel of Figure 5.10. Clearly visible at the low-energy range of the spectrum is the ^{12}B(4+)

82

Resolution (FWHM)	
E	900 keV
ata	12 mrad
bta	9 mrad

Table 5.5: Intrinsic energy resolution, and dispersive and non-dispersive angular resolutions in experiment 08017.

charge-state, included in the PID gate to provide an estimate for the intrinsic energy and angular resolution of the measurement, given in Table 5.5. In addition to the charge state there are clearly two peaks, likely the ground-state and a superposition of excited states in ^{12}Be. To improve the energy resolution, correlations between the excitation energy of ^{12}Be and the dispersive, non-dispersive, and scattering angle (shown in the center panel of Figure 5.10) were removed. These correlations reflect imperfections in the raytracing procedure. Also in the lower panel, the absolute beam energy was calibrated by shifting the entire spectrum such that the ^{12}Be ground-state was centered at $E_x = 0$. The fact that this overall shift places the charge-state at $\sim$ -13 MeV, corresponding to the ground-state Q-value for the reaction plus minor modification for the energy lost in the target, is additional confirmation that shifting E_x in this way is not unreasonable.

Looking closely at the region between -3 and -11 MeV, it is clear there is background contamination present in the ^{12}Be spectrum. This is likely due to the inability of the master gate discussed in Section 5.2 to remove all contamination in the ^{12}Be region of the PID. Figure 5.11 shows the "All ΔE" gate indicated in the last line of Table 5.4, the most effective of the background gates applied. The "All ΔE" threshold is indicated by the purple line (good events are above the threshold, background events are below). A close examination shows it was impossible to remove all background contamination without significantly reducing the
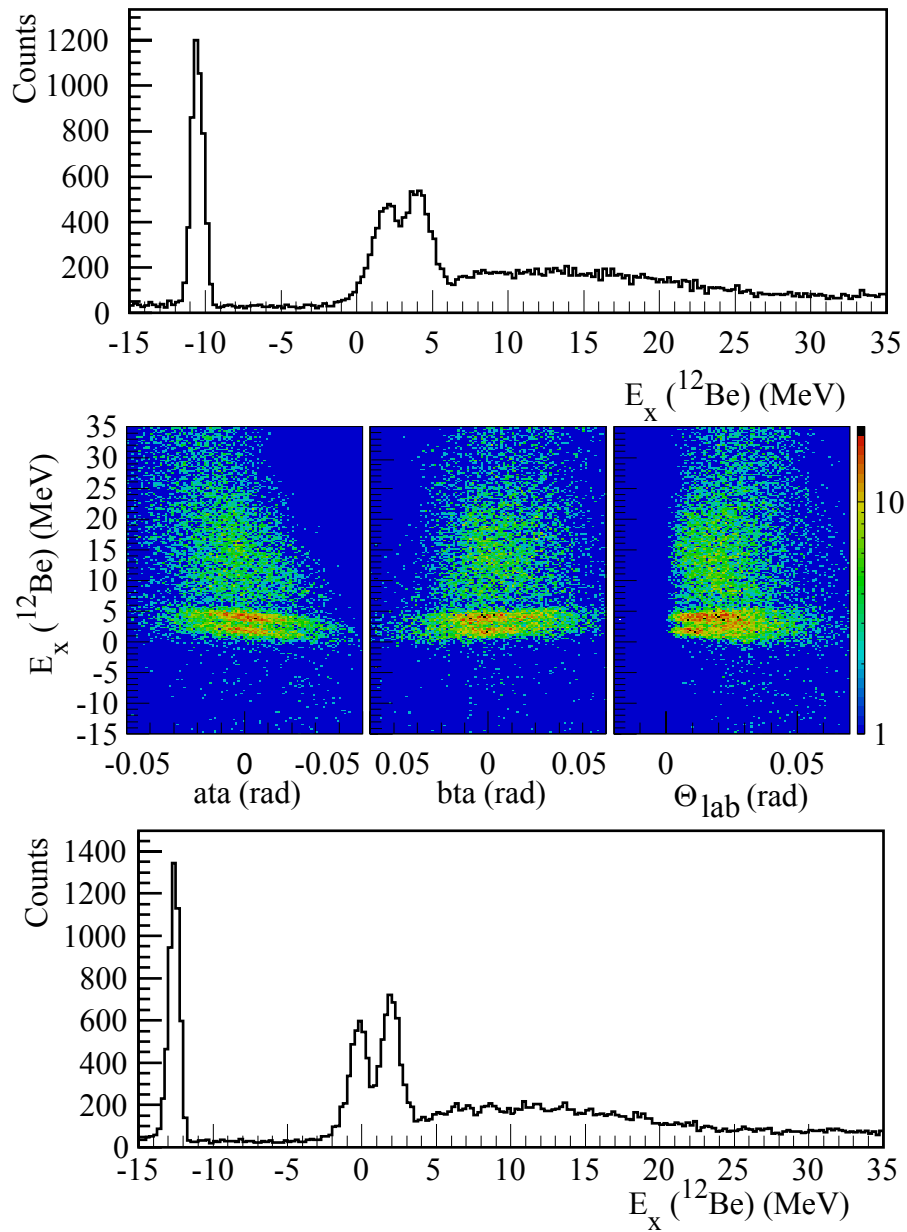
Figure 5.10: (Top) Excitation energy spectrum as generated with missing mass calculation; (middle) Dependence of excitation energy on dispersive, non-dispersive, and scattering angle. The $^{12}B^{4+}$ charge-state has been removed to ease viewing of ^{12}Be events ; (bottom) Angle-corrected excitation energy spectrum.
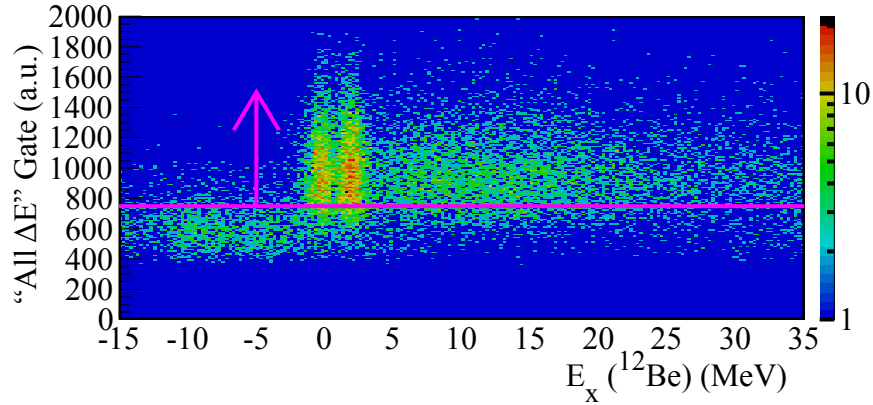
Figure 5.11: "All ΔE" as described in Table 5.4 plotted as a function of ^{12}Be excitation energy. A division between good events and background contamination is visible - the purple line shows the "All ΔE" threshold indicated in Table 5.4.

number of ^{12}Be events as well.

The following procedure was used to remove the remaining (post-master gate) background from the excitation energy spectrum: (1) the counts in the excitation energy spectrum were divided into 10 angular bins of $\Theta_{lab} = 5$ mrad; (2) the "All ΔE" gate was reversed and set so that no signature of ^{12}Be events could be seen in the excitation energy spectrum; (3) in each angular bin the "background-only" excitation energy spectrum was plotted and fit with a fourth-order polynomial, and the fit function was scaled to match the background in the -5 to -10 MeV region of the data; (4) this scaled background function was subtracted from the data in each angular bin. The top panel of Figure 5.12 shows a comparison of the raw data, background, and background-subtracted data for one angular bin ($\Theta_{lab} = 10$-15 mrad). The total background-subtracted excitation energy spectrum including all 10 angular bins (Θ_{lab}=0-50 mrad) is compared with the raw data in the bottom panel of Figure 5.12.

To this point, all excitation energy spectra shown have involved the *singles* data, meaning no coincidence was required with the 429 keV gamma from ^{7}Be. These events include both spin-transfer (ΔS $= 1$) and non-spin-transfer (ΔS $= 0$) contributions. To make sure

85
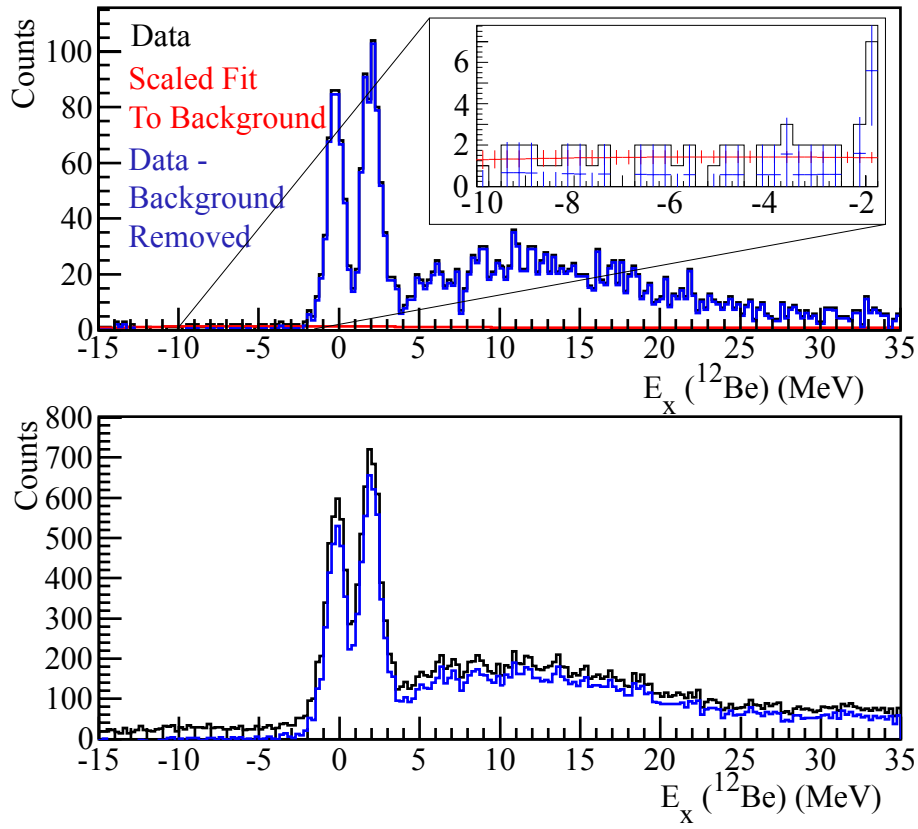
Figure 5.12: (Top) Excitation energy spectrum for ^{12}Be, Θ_{lab} = 10-15 mrad. Raw data shown in black, scaled background function in red, and background-subtracted data shown in blue. Inset shows the region of the excitation energy spectrum used to perform the background scaling. (Bottom) Same, but for Θ_{lab} from 0 to 50 mrad, and not including the scaled background fit.
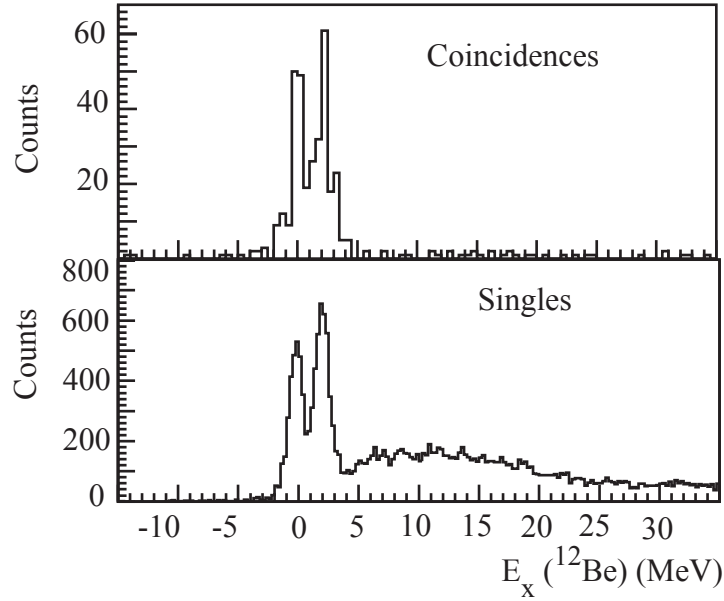
Figure 5.13: ^{12}Be excitation energy spectrum. (Top) Coincidence data; (Bottom) Background-subtracted singles data.

the features of the singles spectrum are be properly interpreted, it is helpful to compare the

singles data with the coincidence data (events where ^{12}Be was detected in the focal plane

and the 429 keV gamma transition was detected in SeGA). These are ensured to be spin-

transfer charge-exchange events, and the excitation energy spectrum for the coincidence data

is shown in the top panel of Figure 5.13. The background-subtracted singles spectrum is

shown for direct comparison in the lower panel of Figure 5.13. Comparing the two spectra it

is clear that the two peaks in the singles data are due predominantly to ^{12}B(^{7}Li, ^{7}Be)^{12}Be

events. The high-energy shoulder visible in the singles data but not in the coincidence data

is mostly due to excitations in ^{7}Be and ^{12}Be above the particle decay threshold, although

minor contributions could be caused by ^{6}Be produced by charge-exchange on the ^{6}Li con-

tamination in the target.

The peak centered at zero is the ground state of ^{12}Be. The peak centered around $\sim$2

MeV could have contributions from three states (labeled by J_x^π, where x=1 for the state of

lowest energy for a specific J^π, $x=2$ for the next-lowest, etc): 2^+_1 (Ex= 2.11 MeV); 0^+_2 (Ex= 2.24 MeV, τ= 331 ns); and 1^-_1 (Ex= 2.68 MeV). Since the 2^+_1 and 1^-_1 states have relatively short lifetimes, information from the Doppler-corrected gamma energy spectrum was used to estimate the contribution of these states to the $\sim$2 MeV peak. Figure 5.14 shows the Doppler-corrected gamma energy spectrum from 1.5 to 4 MeV, gated on different regions of the ^{12}Be excitation energy spectrum, indicated in the figure. The majority of the counts in the gamma spectrum correspond to the higher-lying shoulder region of the E_x spectrum, and these are likely due to transitions through ^{7}Be and ^{12}Be states above the particle decay threshold, or the small background contamination remaining after the master PID gate was applied. Therefore to obtain an accurate estimate of how much the 2^+_1 and 1^-_1 state contribute to the $\sim$2 MeV peak, it is necessary to gate on the 2110 keV and 2680 keV regions of the gamma energy spectrum and look back at their relative contributions to the ^{12}Be excitation energy spectrum, rather than rely solely on the counts in the Doppler-corrected gamma energy spectrum.

The gamma-gated excitation energy spectra are shown in the lower panels of Figure 5.15. The ungated singles spectrum is shown in the top panel for comparison. To estimate the contribution of the 2^+_1 or 1^-_1 states to the $\sim$2 MeV peak, the number of counts in the gamma-gated excitation energy spectra were corrected for the in-beam detection efficiencies for the 2110 keV (2^+_1) and 2680 keV (1^-_1) transitions, 4.1% and 3.2% respectively. The (efficiency-corrected) number of counts in the $\sim$2 MeV peak region was then compared to the number of counts in the same region in the ungated singles data. As previously mentioned, most of the counts in the gamma energy spectrum are not coming from direct population of the 2^+_1 and 1^-_1 states, but rather from states above the decay threshold in ^{7}Be and ^{12}Be,
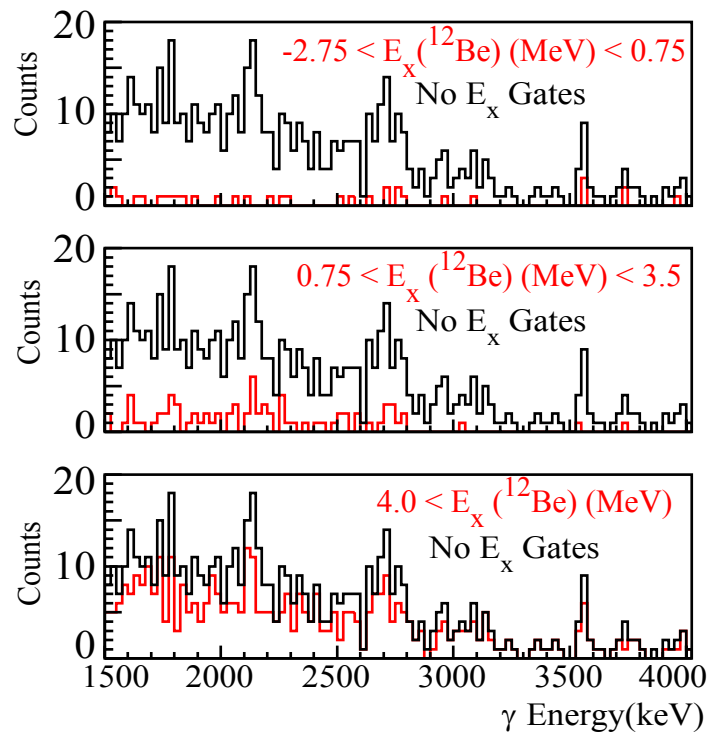
Figure 5.14: Doppler-corrected gamma energy spectrum, gated on ^{12}Be. Black corresponds to all counts (no E_x gates applied). Shown in red are gated spectra, where the E_x (^{12}Be) gates are indicated in the figure.
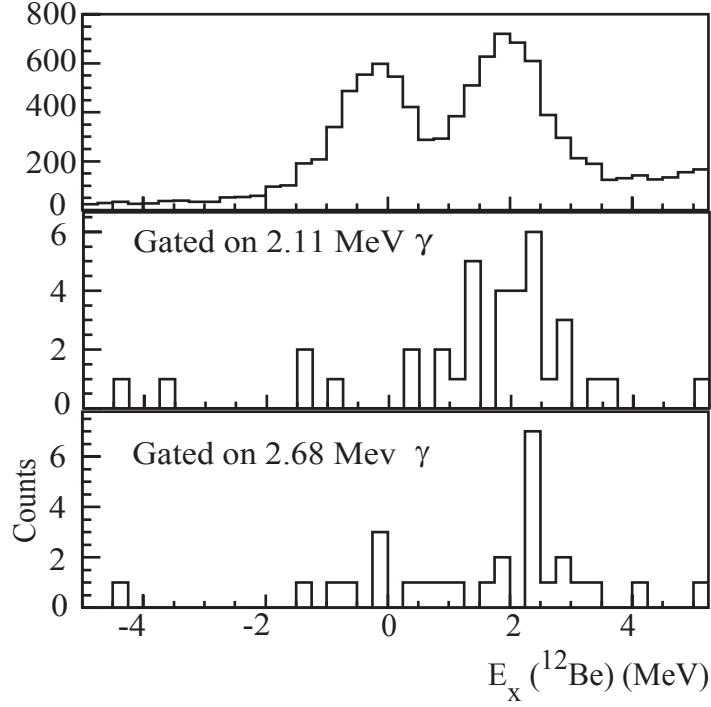
Figure 5.15: ^{12}Be excitation energy spectrum. (Top) Raw Singles Data; (Center) Gated on 2.11 MeV region of gamma energy spectrum; (Bottom) Gated on 2.68 MeV region of gamma energy spectrum.

or from the remaining background contamination in the PID gate applied. The counts in the ground-state peak region of the gamma-gated excitation energy spectrum provide an estimate for the non-direct contributions, as none of the counts in the 2110 keV or 2680 keV gamma energy regions could come from a direct population of the ground state of ^{12}Be. Subtracting the non-direct contribution results in a 10.21% (4.55%) contribution to the $\sim$2 MeV peak from the 2_1^+ (1_1^-) states. The gamma gates used were relatively wide (400 keV), to ensure all the counts from the 2110 keV and 2680 keV peaks would be included, so the percentages listed here should be considered upper limits on the contributions from these states.

Further support for the dominance of the 0_2^+ state in the $\sim$2 MeV region comes from the relatively narrow width of the peak - just 400 keV wider (FWHM) than the ground state

in the singles data. If the ^{12}Be particles were decaying in-flight, the ~2 MeV peak would be significantly broader than the ground state, due to the momentum "kick" experienced when the decay photon is emitted. At the extremes (0 and 180 degree emission angles), this emission of a 2.24 MeV gamma ray would boost the ^{12}Be particle energy by ±940 keV, much more than the 400 keV broadening observed. This suggests most of the nuclei populated in this excited state do not decay in flight before reaching the focal plane, and for the 0_2^+ state, the long lifetime ($\tau = 331$ ns) means only ~33% of nuclei excited to this state in the reaction would decay in flight before detection. This information, combined with the gamma analysis described previously, provides strong evidence that the 0^+ state is likely the dominant component of the ~2 MeV peak in the ^{12}Be excitation energy spectrum. Further discussion of the relative 0_2^+, 2_1^+, and 1_1^- contributions to the ~2 MeV peak can be found in Chapter 6, in the context of the Multipole Decomposition Analysis (MDA).

5.4 Cross-section Calculations

The last step of the data analysis procedure involves calculating differential cross-sections $d\sigma/d\Omega$ to each of the states seen in the ^{12}Be excitation energy spectrum, and generating an angular distribution ($d\sigma/d\Omega$ vs. scattering angle Θ_{com}). To calculate the differential cross-section, counts in the excitation energy spectra for the singles and coincidence data set (shown in Figure 5.13) are divided into discrete angular bins - 10 bins of 5 mrad each for the singles data, and 5 bins of 10 mrad each for the coincidence data. The number of bins and bin size was chosen such that there were sufficient statistics in each bin to identify and fit the ground state and ~2 MeV peaks within reasonable error. The excitation energy spectra for the singles and coincidence data in each angular bin are shown in Figures 5.16 and 5.17.

The differential cross section is given by

$$\frac{d\sigma}{d\Omega_{lab}} = \frac{N_m}{N_i N_t \mathcal{L}} \frac{1}{d\Omega_{lab}} \ ,$$ (5.18)

where N_m refers to the integrated counts in the ground state and $\sim$2 MeV peaks (after background subtraction, for the singles case), N_i refers to the number of incident ^{12}B ions, N_t refers to the number of ^{7}Li atoms in the target, $\mathcal{L}$ is the average live-time of the data acquisition system (0.9), and $d\Omega_{lab}$ is the opening angle subtended by the scattering angle. The efficiency of the focal-plane detectors is assumed to be 100%. For the coincidence data, the efficiency of detection for the 429 keV gamma 'tag' must also be included in the denominator of Equation 5.18.

In the laboratory frame, $d\Omega$ is obtained from a simple geometric interpretation:

$$d\Omega = 2\pi \int_{\Theta_i}^{\Theta_f} \sin\Theta \, d\Theta \ ,$$ (5.19)

where Θ_i and Θ_f are the boundaries of the angular bin. N_t is easily calculated from the target thickness (5.5 mg/cm^2), target composition (92.5% ^{7}Li), and mass of ^{7}Li (1.165 $\times$ 10^{-20} mg):

$$N_t = \frac{5.5 mg/cm^2 \times 0.925}{1.165 \times 10^{-20} mg} = 4.409 \times 10^{20} cm^{-2} \ .$$ (5.20)

N_i was calculated on a run-by-run basis using a periodic rate calibration. Three times during the experiment (at the beginning, after a short facility breakdown, and towards the end of the ^{12}Be production runs), a plastic scintillator located at the object of the analysis line was inserted into the path of the beam and the unreacted beam was directed into the focal plane of the spectrograph. This allowed for simultaneous measurements of the rate on the object scintillator (located at the entrance to the S800 analysis line) and the secondary beam rate (measured in the focal plane of the S800), providing information about
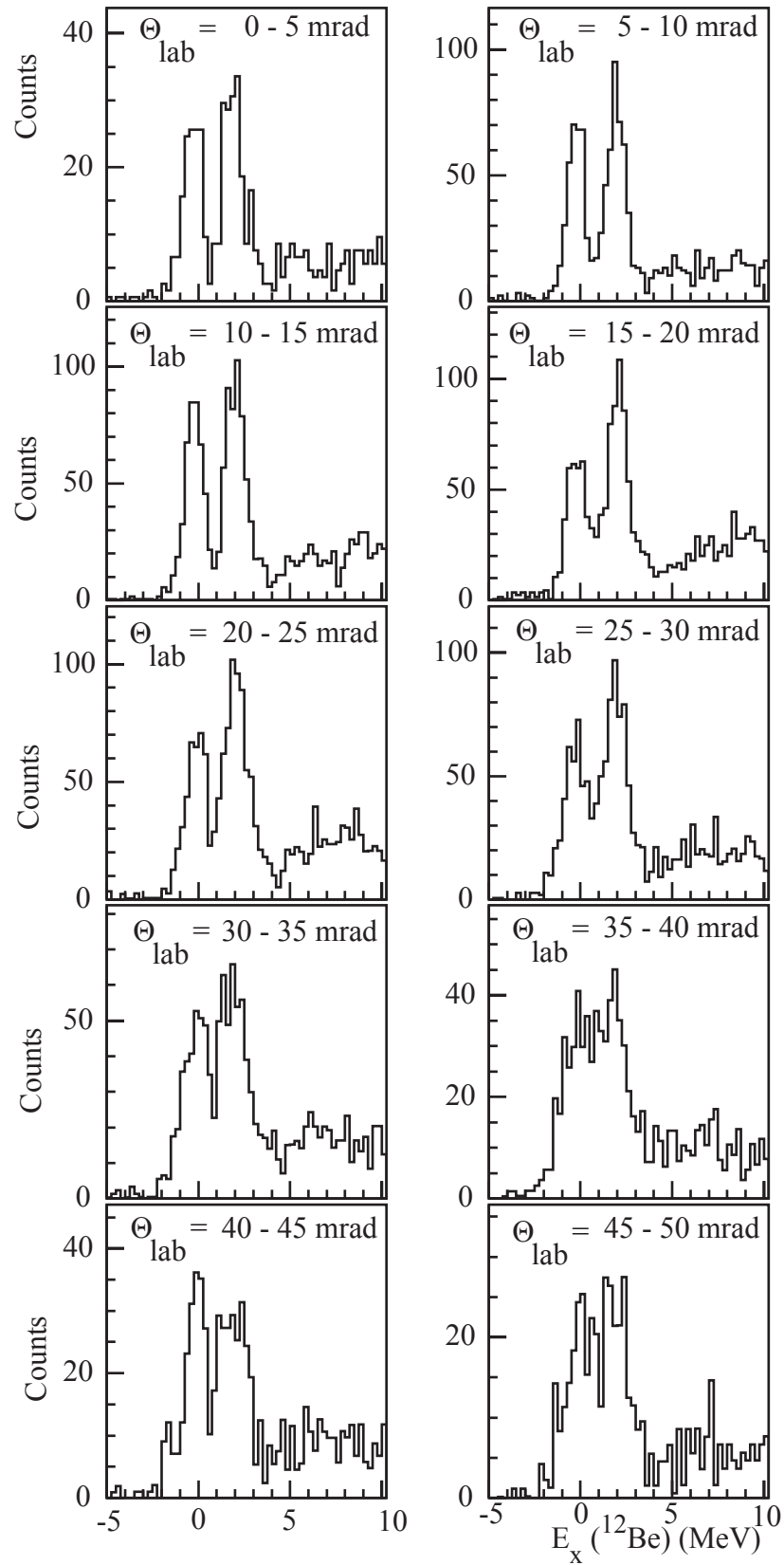
Figure 5.16: Excitation energy spectrum, singles data, divided into angular bins used in cross-section calculation.
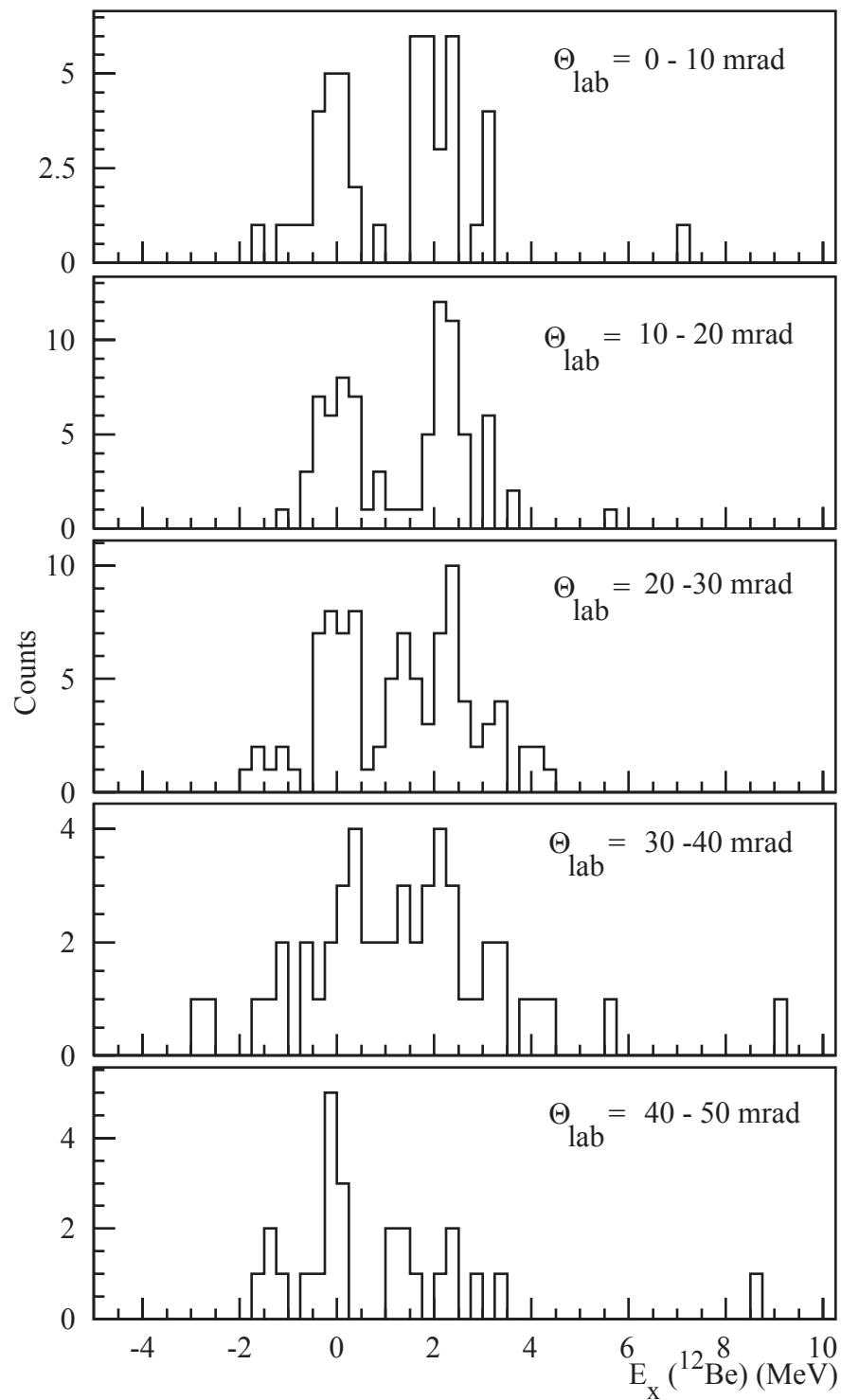
Figure 5.17: Excitation energy spectrum, coincidence data, divided into angular bins used in cross-section calculation.

the transmission through the analysis line ($\sim$33%) and a calibration between the object scintillator rate and the secondary beam rate. Since the object scintillator could not be in the path of the beam during the experiment, it was also necessary to correlate the object scintillator rate to non-intercepting probes located near the exit of the K1200 cyclotron and at the production target position. These probes were continuously monitored throughout the course of the experiment, and the average primary beam current readings were used to estimate the number of incident beam particles during each run. In total, summed over all runs, N_i was determined to be 1.21×10^{12}.

The procedure used to obtain N_m is illustrated in Figure 5.18. Although the figure shown is for one angular bin in the singles data set, the same procedure was followed for both coincidence and singles data, in all angular bins. First, the E_x= -2.5 to 3.57 MeV region was fit using two Gaussian functions representing the ground state and $\sim$2 MeV peaks. Then, the area under the second (first) Gaussian function was subtracted from the histogram and the counts in the first (second) peak were integrated. The limits of integration were set using the Gaussian fit functions (g(x) must be > 0.01 to be included in integration region), with the exception of the upper limit for the $\sim$2 MeV peak, set to 3.57 MeV for all angular bins in the singles data.

To ensure the counts in the $\sim$2 MeV peak in the singles data set aren't overestimated, one must carefully consider (i) higher-lying excitations in ^{7}Be; and (ii) the ^{6}Li present in the $^{\text{nat}}$Li target. To determine whether or not higher-lying excitations in ^{7}Be could be contributing to counts in the $\sim$ 2 MeV peak, it is helpful to calculate where ^{12}Be events populated through these states would lie in the excitation energy spectrum. The first state in ^{7}Be above the $1/2^-$ state at 429 keV is located at 4.57 MeV, and has a width of 175

keV (FWHM). If the charge-exchange reaction producing ^{12}Be in its ground state went through this state, the corresponding peak in the excitation energy spectrum would have a width comparable to that of the coincidence data ($\sim$860 keV, FWHM) plus the width of the unbound state itself (175 keV) and would be centered at 4.57 MeV. Since the upper limit of the $\sim$ 2 MeV peak was set to 3.570, approximately 1.25% of the counts from the ^{12}B(^{7}Li, ^{7}Be(4.57 MeV))^{12}Be reaction could make it into the integration region for the $\sim$2 MeV peak. However, the relative probability of populating the 4.57 MeV state in ^{7}Be (compared to the states below the neutron decay threshold) is unknown, so it is impossible to estimate exactly the number of counts that should be removed from the second peak, and the 1.25% of ^{12}B(^{7}Li, ^{7}Be(4.57 MeV))^{12}Be events that make it into the $\sim$2 MeV peak must be taken as a systematic error in the cross-section calculation. It is possible to get a more definite estimate for the ^{6}Li contamination present in the $\sim$2 MeV peak, following the same logical procedure. The Q-value for the ^{12}B(^{6}Li, ^{6}Be)^{12}Be reaction is -15.996 MeV, placing the ground state ^{12}Be events produced in this reaction at E_x=3.427 MeV, within the summing region for the $\sim$2 MeV peak. With 12.33 times more ^{7}Li than ^{6}Li in the target, and B(GT)$_{^{7}Li\rightarrow^{7}Be}$ 1.45 times stronger than B(GT)$_{^{6}Li\rightarrow^{6}Be}$ [104], ^{6}Li should be populated $\sim$1/18 times as frequently as ^{7}Li. However, only 55% of the ^{6}Li peak width is included in the summing region, and therefore 3.1% of the counts in the $\sim$2 MeV peak were assumed to be due to ^{6}Li contamination and removed from the cross-section calculation.

The differential cross-sections obtained in this manner have to be transformed to the center of mass frame to be compared with theoretical cross-section calculations (see: Chapter 6). This essentially boils down to a transformation of the opening angle from the laboratory
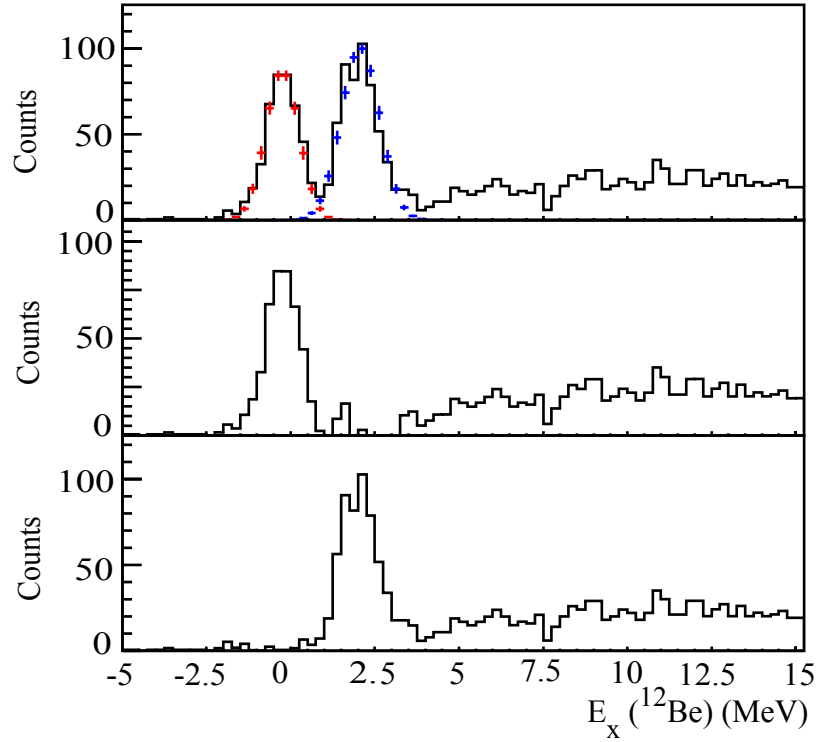
Figure 5.18: Illustration of peak-fitting procedure used to extract N_m.

to center of mass frame, which for small angles is

$$\frac{d\Omega_{com}}{d\Omega_{lab}} = \frac{1 - \beta^2}{(\beta - 1)^2} \quad .$$
(5.21)

The angular distributions for the ground and ~2 MeV states in ^{12}Be for the singles data set are shown in Figure 5.19 and Table 5.6. The coincidence data angular distributions are shown in Figure 5.20 and Table 5.7.
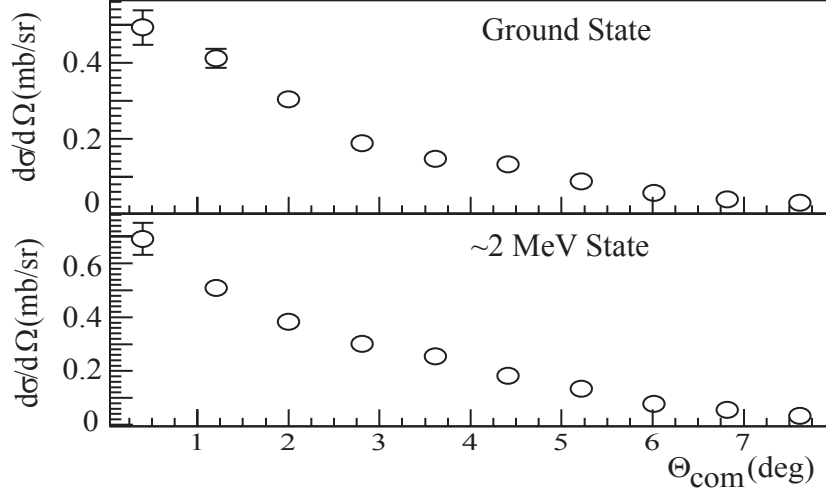
Figure 5.19: Angular distributions, singles data.

Angular Bin (Θ_{lab})	$\frac{d\sigma}{d\Omega}$ (g.s.) (mb/sr)	$\frac{d\sigma}{d\Omega}$ ($\sim$2MeV) (mb/sr)
0 - 5 mrad	0.442 ± 0.041	0.613 ± 0.052
5 - 10 mrad	0.369 ± 0.023	0.452 ± 0.025
10 - 15 mrad	0.272 ± 0.015	0.339 ± 0.018
15 - 20 mrad	0.169 ± 0.012	0.267 ± 0.013
20 - 25 mrad	0.132 ± 0.009	0.225 ± 0.011
25 - 30 mrad	0.118 ± 0.008	0.160 ± 0.009
30 - 35 mrad	0.078 ± 0.006	0.119 ± 0.007
35 - 40 mrad	0.051 ± 0.005	0.069 ± 0.005
40 - 45 mrad	0.036 ± 0.003	0.050 ± 0.004
45 - 50 mrad	0.028 ± 0.003	0.030 ± 0.003

Table 5.6: Angular distributions, singles data.

Angular Bin (Θ_{lab})	$\frac{d\sigma}{d\Omega}$ (g.s.) (mb/sr)	$\frac{d\sigma}{d\Omega}$ ($\sim$2MeV) (mb/sr)
0 - 10 mrad	0.129 ± 0.029	0.150 ± 0.037
10 - 20 mrad	0.077 ± 0.013	0.089 ± 0.015
20 - 30 mrad	0.060 ± 0.010	0.070 ± 0.011
30 - 40 mrad	0.021 ± 0.010	0.020 ± 0.007
40 - 50 mrad	0.010 ± 0.003	0.007 ± 0.002

Table 5.7: Angular distributions, coincidence data.
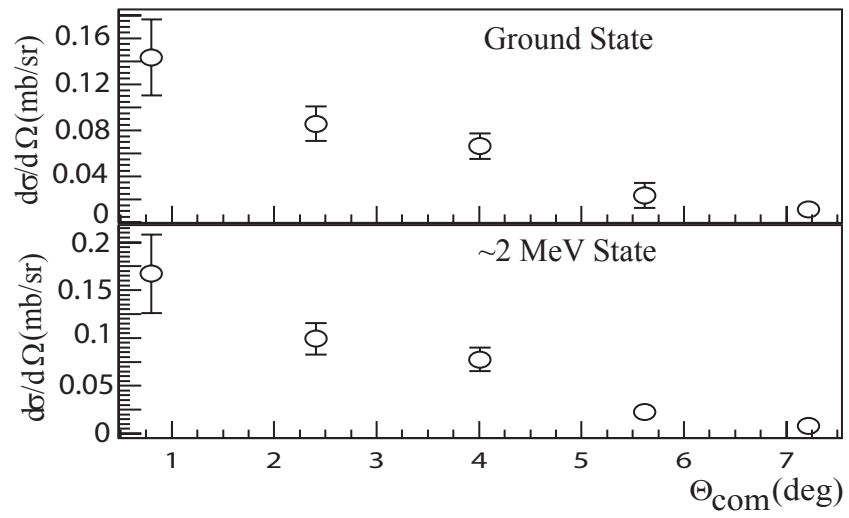
Figure 5.20: Angular distributions, coincidence data.

Chapter 6

Results

Angular distributions in hand, this chapter focuses on the extraction of the Gamow-Teller strength distribution for ^{12}Be. First, the $\Delta L = 0$ component of the cross-section was isolated via a Multipole Decomposition Analysis (MDA) using the theoretical cross-sections described in Chapter 3. Then, the zero-degree $\Delta L = 0$ cross-section was extrapolated to zero momentum transfer using the DWBA scaling factors given in Section 3.3. The $\Delta L = 0$, $q = 0$ cross-section was input into Equation 1.12 to extract the B(GT) distribution for the two 0^+ states in ^{12}Be, with the unit-cross section $\hat{\sigma}$ derived from the ^{12}Be $\rightarrow$ ^{12}B β-decay half-life. Finally, the B(GT)(0_2^+, 2.24 MeV)/B(GT)(0_1^+,g.s.) ratio obtained in the current work was compared with shell-model predictions, and the $0\hbar\omega$ component of the wavefunction deduced is compared with previous measurements and models.

6.1 Multipole Decomposition Analysis

For the ground state and ~ 2 MeV excited state in ^{12}Be, in both the singles and coincidence data set, a Multipole Decomposition Analysis (MDA) was performed to extract the $\Delta L = 0$ component of the cross-section at zero degrees. The angular distributions shown in Figures 5.19 and 5.20 were fit with a linear combination of theoretical (DWBA) cross-sections

$$\left[\frac{d\sigma}{d\Omega}\right]_{total}^{DWBA} = a\left[\frac{d\sigma}{d\Omega}\right]_{\Delta L=0} + b\left[\frac{d\sigma}{d\Omega}\right]_{\Delta L=1} + c\left[\frac{d\sigma}{d\Omega}\right]_{\Delta L=2} + d\left[\frac{d\sigma}{d\Omega}\right]_{\Delta L=3} + ... \quad (6.1)$$

where fitting parameters a, b, c, d, and so on were allowed to vary freely until the total DWBA cross-section best fit the angular distribution from the data. "Best fit" was defined by the lowest reduced χ^2 value (χ^2/N, where N is the number of angular bins less the number of components included in the fit). Recall, that the error due to the tensor force has been quantified (Section 3.4), and therefore ΔJ_r in the theoretical angular distributions will be used synonymously with ΔL in the MDA discussion.

Looking back at the calculations of Chapter 3, it is clear that for both the coincidence case (where there were five angular bins) and the singles data set (ten angular bins), many more ΔL components were calculated than could be included in any reasonably constrained fit. Since the angular distributions produced in DWBA calculations depend strongly on L-transfer and weakly on nuclear structure input, the calculated cross-sections are generally reliable with respect to the order of magnitude of each ΔL component. Therefore the strongest ΔL components of each state below the neutron decay threshold in ^{12}Be (ground state, 2_1^+, 0_2^+, and 1_1^-) were selected for use in the MDA fits - these components are shown in Table 6.1. Different combinations of these multipole components were tested systematically until either: (1) the lowest χ^2/N value was achieved; or (2) it was determined that the χ^2/N

	Coincidences	Singles
Ground State	011, 211, 221	011, 211, 221, 231, 431
~2 MeV State	(2_1^+) 211, 011, 212;	(2_1^+) 211, 011, 212, 202, 231, 431;
	(0_2^+) 011, 211, 221;	(0_2^+) 011, 211, 221, 231, 431;
	(1_1^-) 112, 312, 111	(1_1^-) 112, 312, 111

Table 6.1: Theoretical DWBA cross-sections included in MDA fits. Three-digit labels refer to ΔJ_r, ΔJ_t, and ΔJ_p, as defined in Chapter 3.

was independent of the component choice.

Strictly speaking, the singles data MDA should include multipole components from both the $^7\text{Li} \to {}^7\text{Be}$(g.s., $3/2^-$) and $^7\text{Li} \to {}^7\text{Be}$(429 keV, $1/2^-$) DWBA calculations (Figures 3.1 through 3.8). However, according to total angular momentum selection rules (Table 3.1), all of the ^7Be(429 keV, $1/2^-$) multipole components are included in the ^7Be(g.s., $3/2^-$) calculation, and since the absolute magnitude of each multipole component is tuned in the MDA fitting procedure, it is reasonable to use only the $^7\text{Li} \to {}^7\text{Be}$(g.s., $3/2^-$) multipole components (Figures 3.5 through 3.8) in the MDA of the singles data.

Prior to performing the MDA fits, the DWBA cross-sections were adjusted for two factors: resolution effects, as the experimental angular resolution was comparable to the bin size; and binning effects, as the fine binning used in the DWBA calculations would not be an accurate reflection of the widely binned angular distribution of the data. To account for the experimental angular resolution (12 and 9 mrad in the dispersive and non-dispersive direction, respectively), the following steps were taken: (1) the DWBA cross-sections were fit with an 11th-order polynomial; (2) the polynomial parameters were imported into a FORTRAN code, which generated the angular distribution in the laboratory frame; (3) the laboratory frame angular distribution was smeared with the experimental resolution; and (4)
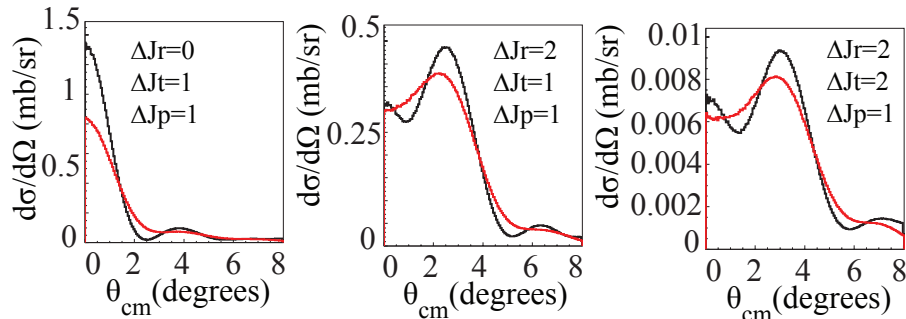
Figure 6.1: Original (black) and smeared (red) DWBA angular distributions for the ^{12}B(g.s., 1^+) $\rightarrow$ ^{12}Be(g.s., 0^+), ^{7}Li(g.s., $3/2^-$) $\rightarrow$ ^{7}Be(429 keV, $1/2^-$) transition. Only states included in the MDA are shown.

the smeared distribution was converted back into the center-of-mass frame. The original and post-smearing angular distributions are shown in black and red in Figures 6.1 through 6.4. Note that the sharp features (peaks, valleys) of the original distributions become washed out, and the smearing procedure has a significant effect on the $\Delta L(\Delta J_r) = 0$ component at zero degrees.The effects of re-binning are not shown explicitly here but can be seen in the MDA fits for the singles and coincidence data to follow.

6.1.1 Extraction of $\Delta L = 0$ cross-section, Singles Data

The angular distributions of the ground and $\sim$2 MeV states in the singles data were best fit with a combination of $\Delta L = 0$, 2, and 4 components, and the final MDA fits are shown in Figure 6.5. A relatively strong $\Delta L = 2$ component was required to fit the angular region between 3 and 5 degrees, and the $\Delta L = 4$ component was needed to fill out the angular distribution at the largest angles. At zero degrees the $\Delta L = 0$ component is strongest. A χ^2/N of 4.27 was achieved for the ground state, and for the $\sim$2 MeV state χ^2/N was 0.59. The MDA scaling factors for the $\Delta L = 0$ (a, Equation 6.1), $\Delta L = 2$ (c, Equation 6.1) and
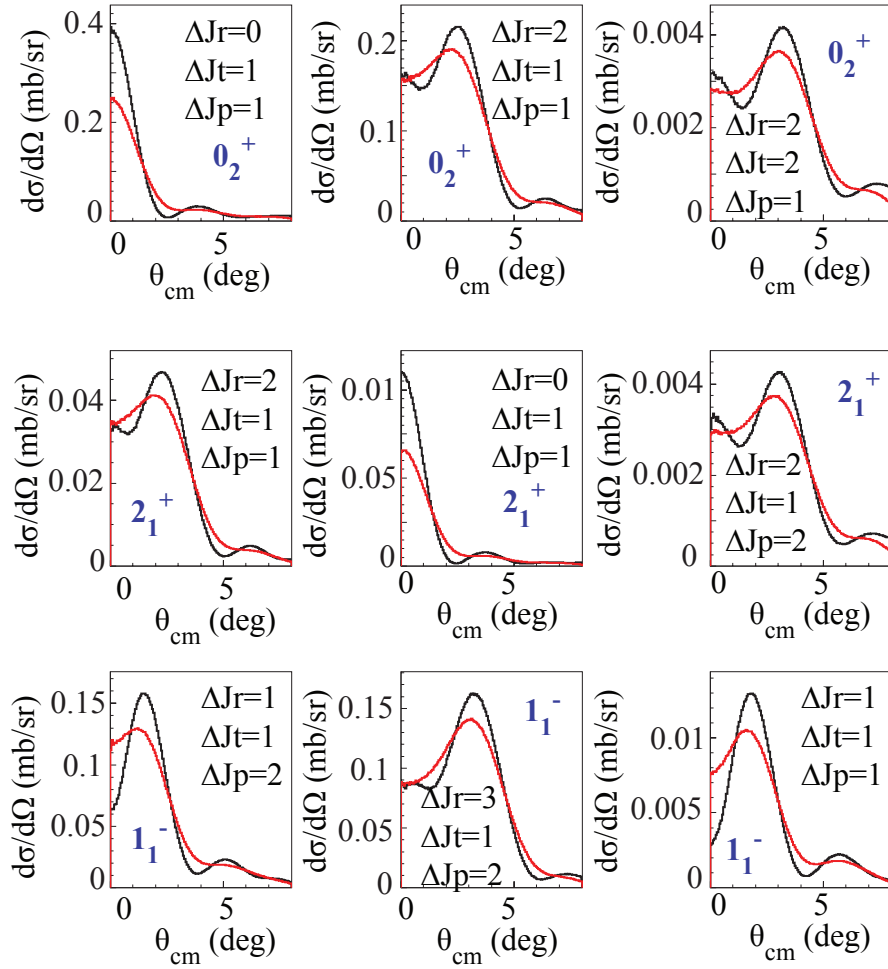
Figure 6.2: Original (black) and smeared (red) DWBA angular distributions for transitions to the ~2 MeV state in ^{12}Be, for the ^{7}Li(g.s., $3/2^-$) $\rightarrow$ ^{7}Be(429 keV, $1/2^-$) transition. Only states included in the MDA are shown.
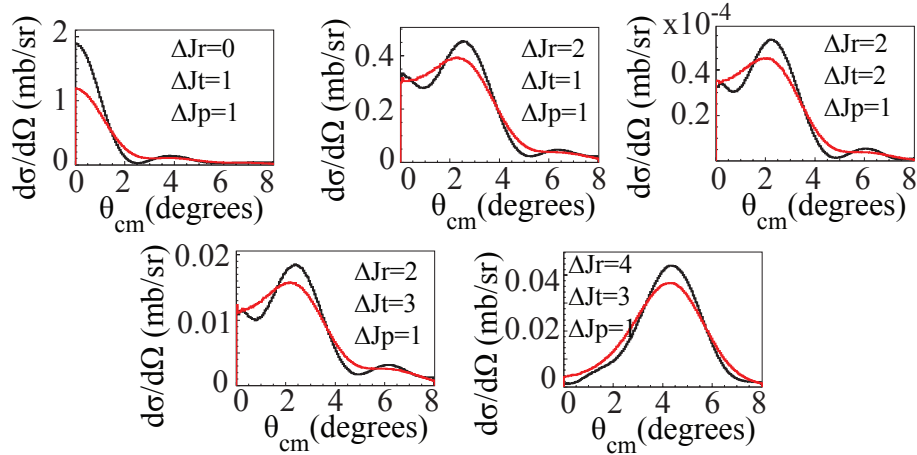
Figure 6.3: Original (black) and smeared (red) DWBA angular distributions for the ^{12}B(g.s., 1^+) $\rightarrow$ ^{12}Be(g.s., 0^+), ^{7}Li(g.s., $3/2^-$) $\rightarrow$ ^{7}Be(g.s., $3/2^-$) transition. Only states included in the MDA are shown.

Multipole Component	Scaling Factor, g.s.	Scaling Factor, $\sim$2 MeV state
$\Delta L = 0$	0.460 ± 0.037	1.529 ± 0.141
$\Delta L = 2$	0.309 ± 0.040	1.091 ± 0.092
$\Delta L = 4$	1.409 ± 0.189	3.205 ± 0.349

Table 6.2: Scaling factors for $\Delta L = 0$, 2, and 4 components, as defined in Equation 6.1, for calculations in which all $2\hbar\omega$ configurations were shifted by ΔE= -3 MeV.

$\Delta L = 4$ (not labeled, Equation 6.1) are given in Table 6.2.

For the ground state, fits were made including two, three, four and five multipole components. Including additional $\Delta L = 2$ components merely fragments the total $\Delta L = 2$ strength, and has no significant impact on the $\Delta L = 0$ cross-section at zero degrees. As the shape of the $\Delta L = 2$ components are similar (see Figure 6.3), exchanging the $\Delta J_r \Delta J_t \Delta J_p$=211 component with the other $\Delta L = 2$ combinations given in Table 6.1 only acts to increase the magnitude of the $\Delta L = 2$ coefficient in Equation 6.1 - as before, there is no significant change in the $\Delta L = 0$ cross-section at zero degrees. Since the choice of $\Delta L = 2$ component was somewhat arbitrary, the $\Delta J_r \Delta J_t \Delta J_p$=211 component was selected, as it was the strongest
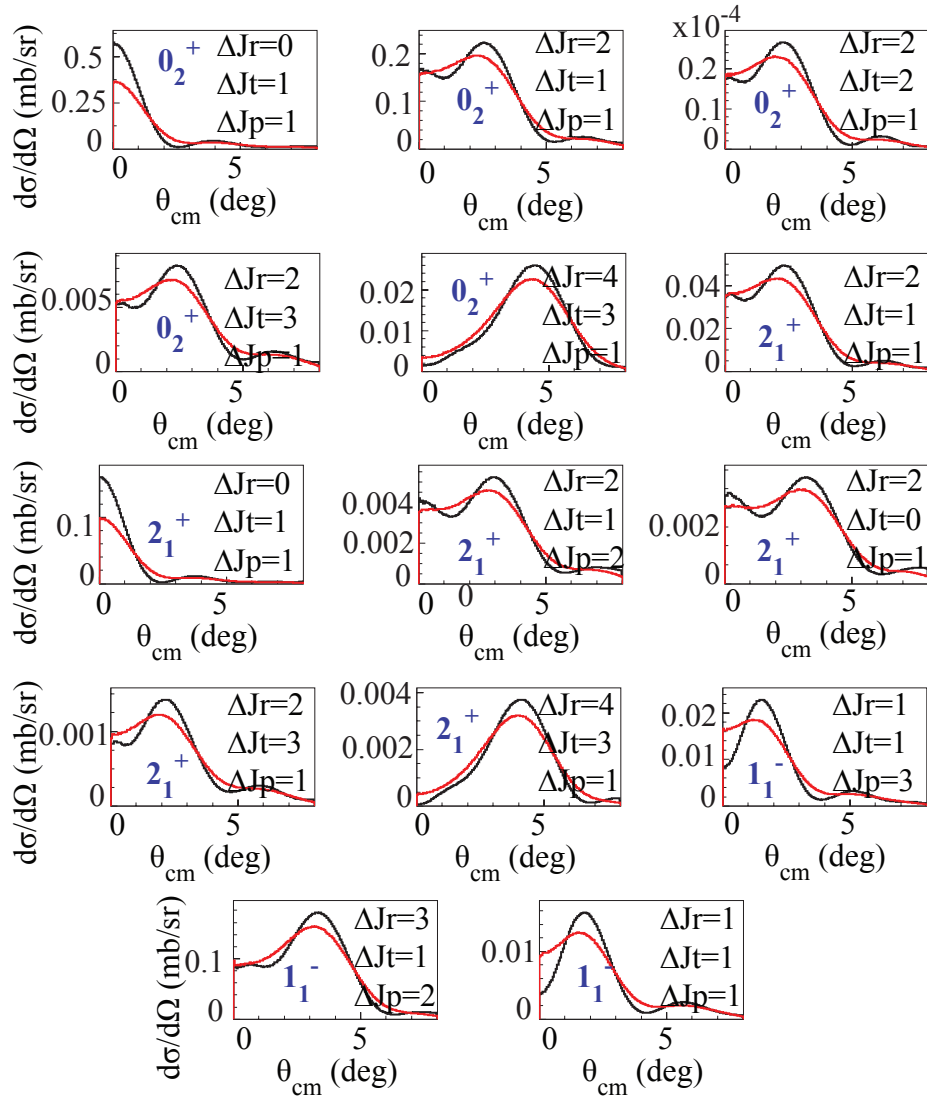
Figure 6.4: Original (black) and smeared (red) DWBA angular distributions for transitions to the ~2 MeV state in ^{12}Be, for the ^{7}Li(g.s., $3/2^-$) $\rightarrow$ ^{7}Be(g.s., $3/2^-$) transition. Only states included in the MDA are shown.
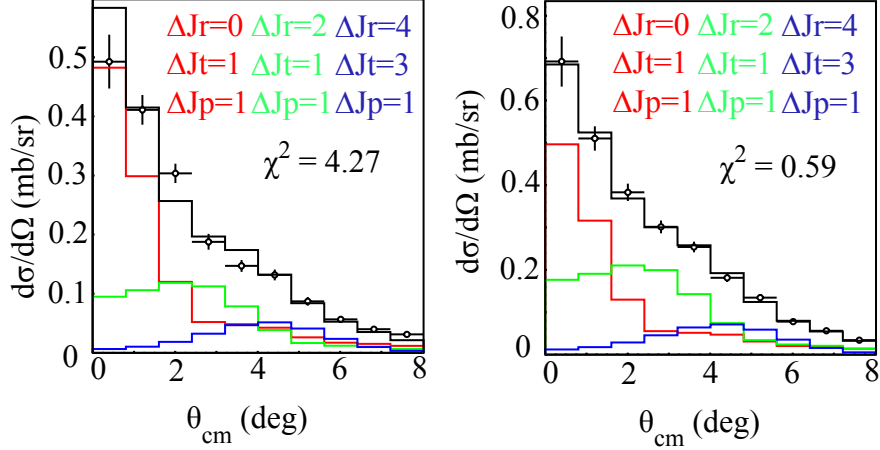
Figure 6.5: MDA fits for the ground state (left panel) and ~ 2 MeV state (right panel), singles data.

of the three $\Delta L = 2$ components calculated.

For the ~ 2 MeV state, the situation is slightly more complicated, as hypothetically components from the 0_2^+, 2_1^+, and 1_1^- states could all contribute to the angular distribution. However, as seen on the right side of Figure 6.5, the $\Delta L = 0$, 2, and 4 components from the 0_2^+ state do an excellent job of reproducing the experimental angular distribution. No fit in which a $\Delta L = 1$ component was included converged, and fits including a $\Delta L = 3$ component converged but yielded $\Delta L = 0$ cross-sections that agreed with the $\Delta L = 2$ and 4 component fits within error bars (difference in $\Delta L = 0$ cross section was less than 1%). At forward angles, a strong $\Delta L = 3$ component is unlikely without a strong $\Delta L = 1$ component, so the $\Delta L = 2$ and 4 components were chosen for the final MDA fit. This result supports the conclusion made using the in-flight gamma energy spectrum, which placed an upper limit of 5% on the contributions from the 1_1^- state. The shape of the angular distribution for multipole components with the same ΔL are very similar - so including other $\Delta L = 0$, 2 or 4 components in the fit (including those from the 2_1^+ state) has negligible effect on the

107

$\left[\dfrac{d\sigma}{d\Omega}\right]_{\Delta L=0}$ (mb/sr)	MDA	q=0
Ground State	0.482 ± 0.039	0.684 ± 0.055
2.24 MeV 0_2^+	0.496 ± 0.046	0.796 ± 0.073

Table 6.3: $\Delta L = 0$ cross-sections, from MDA and after extrapolation to $q = 0$.

$\Delta L = 0$ cross-section at zero degrees. This, combined with the 10% limit from the in-flight gamma analysis, justifies the use of only the 0_2^+ $\Delta L = 0, 2,$ and 4 components in the final fit.

It is worth noting that the error in the $\Delta L = 0$ cross-section at zero degrees is dominated by the fit to the first two angular bins (θ_{cm}=0-1.6 degrees), and the second bin (θ_{cm}=0.8-0.16) carries more weight than the first. χ^2/N, however, depends on all ten bins, including those at large angles. Therefore, the addition of higher multipoles like $\Delta L = 2, 3, 4$ (which peak at larger angles) to the MDA fit reduces the χ^2/N value and improves the overall fit, but has very little effect on the ΔL=0 cross-section at zero degrees. This results in the relatively small error bars for the $\Delta L = 0$ component at zero degrees included in Table 6.3.

Since the angular distribution for the ~2 MeV state can be adequately reproduced using only components from the 0_2^+ state in ^{12}Be, and the gamma analysis discussed in Chapter 5 limits the contributions of the 2^+ and 1^- states to 10 and 5%, respectively, in all further discussions of the B(GT) distribution the ~2 MeV state will be referred to as the 2.24 MeV 0_2^+ state, and any contribution from the 2_1^+ or 1_1^- state will be neglected. The zero-degree $\Delta L = 0$ cross-sections found using the MDA are given in Table 6.3. Also included in the table are the $\Delta L = 0$ cross-sections extrapolated to $q = 0$ using the scaling factors of section 3.3.
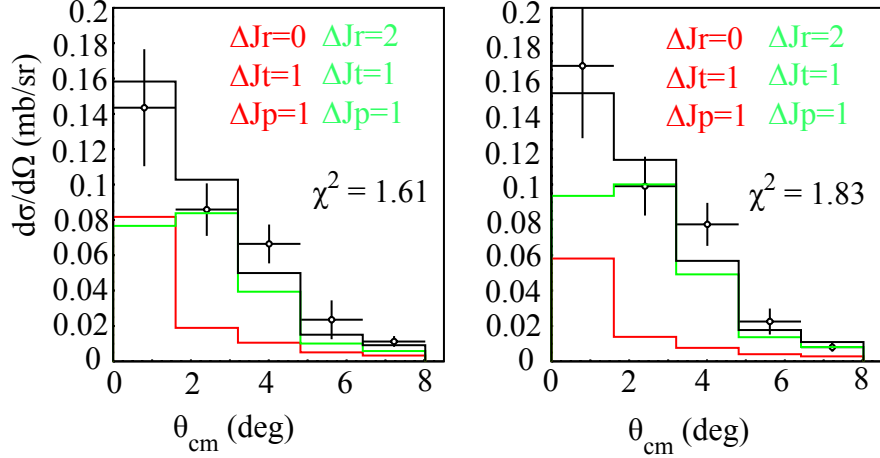
Figure 6.6: MDA fits for the ground state (left panel) and ~ 2 MeV state (right panel), coincidence data.

6.1.2 Extraction of $\Delta L = 0$ cross-section, Coincidence Data

Limited to five angular bins in the coincidence data, at most four theoretical cross-section components could be included in the MDA. However, due to the large statistical errors in this data set, it was impossible to deduce which DWBA cross-sections should be included. Based on the singles data MDA for the ground and excited state, $\Delta L = 0$ and 2 components were selected (see Figure 6.6), but since an independent MDA could not be performed the $\Delta L = 0$ cross-sections at zero degrees for the coincidence data set were not ultimately used to extract Gamow-Teller strengths.

6.2 ^{12}Be B(GT) Distribution

The final step for extracting the B(GT) distribution in ^{12}Be is to calibrate the unit-cross section $\hat{\sigma}$ using the proportionality relationship given in Chapter 1 [13]

$$\frac{d\sigma}{d\Omega}_{q=0} = \hat{\sigma} B(GT) \ . \tag{6.2}$$

$E_x(^{12}\text{Be})$	J^π	B(GT)
0 MeV (g.s)	0^+_1	0.184 ± 0.008
2.24 MeV	0^+_2	0.214 ± 0.051

Table 6.4: B(GT) distribution, ^{12}Be.

This relationship can be calibrated using the ^{12}Be(g.s.) $\rightarrow$ ^{12}B(g.s.) B(GT), calculated from the β-decay ft-value,

$$ft = \frac{C}{B(F) + (g_A/g_V)^2 B(GT)} \ ,$$ (6.3)

where $log(ft)$=3.834±0.017 [105], $B(F)$=0 for a $0^+ \rightarrow 1^+$ transition, C=6143±2 s [11] and g_A/g_V=-1.2694±0.0028 [12]. After taking into account detailed balance

$$B(GT,^{12}\text{B} \rightarrow^{12} \text{Be}) = \frac{(2J_\text{Be} + 1)}{(2J_\text{B} + 1)} B(GT,^{12} \text{Be} \rightarrow^{12} \text{B})$$ (6.4)

this results in a B(GT) of 0.184±0.008. Using this B(GT) and the ground state to ground state $\Delta L = 0$ cross-section at $q = 0$, one obtains a unit cross-section $\hat{\sigma}$=3.722±0.334. Applying this unit-cross section to the 2.24 MeV 0^+_2 state yields a B(GT) of 0.214±0.051. The B(GT) distribution for ^{12}Be is given in Table 6.4. The ground state error consists only of the error in the β-decay log(ft) value, propagated through the B(GT) calculation. The error for the 2.24 MeV state includes: statistical and fitting errors coming from the χ^2 minimization errors on the $\Delta L = 0$ component, propogated through the extrapolation to $q = 0$ and conversion to B(GT) (8% for the ground state, 9% for the excited state); and systematic errors from tensor contributions (11%, see section 3.4), q=0 extrapolation assumptions (1%, see section 3.3), peak-fitting procedure (4%), and smearing of DWBA angular distributions (1%).

6.3 Comparison with Shell Model Predictions

The Gamow-Teller strength for transitions to the 0^+ states in ^{12}Be is very sensitive to the mixing of $0\hbar\omega$ and $2\hbar\omega$ configurations. As discussed in Chapter 2, the ratio of B(GT) for the 0^+ states

$$R = \frac{B(GT)(0_2^+, 2.24 MeV)}{B(GT)(0_1^+, g.s.)} \tag{6.5}$$

can provide information about the $0\hbar\omega$ component of the ground and excited 0^+ state wavefunction. The B(GT) ratio obtained in the current study was 1.162±0.283. This ratio was compared to that predicted by OXBASH shell model calculations, using the WBP interaction in the spsdpf model space. As described in Section 2.3, all $2\hbar\omega$ configurations were manually adjusted by ΔE to account for the effect of $4\hbar\omega$ and higher admixtures. Thirty-one separate calculations were performed, with ΔE varying from -2.0 to -5.0 MeV in increments of 0.1 MeV. Each calculation is one data point in the left (right) panel of Figure 6.7, as a function of the percentage of the ground (excited) state wavefunction that is made up of $0\hbar\omega$ configurations. The ratio found in the current study is indicated by the red line, with the shaded red area representing the error. This ratio indicates the ground state wavefunction is 25.48±5.49% $0\hbar\omega$, and the excited state wavefunction is 59.83±4.78% $0\hbar\omega$.

The B(GT) ratio is plotted as a function of the ratio of $0\hbar\omega$ configurations in the excited state to $0\hbar\omega$ configurations in the ground state in Figure 6.8. As predicted by a two-level mixing scheme, the influence of $2\hbar\omega$ configurations has an opposite effect on the $0\hbar\omega$ percentage of the ground state and excited states. However, it is notable that the $0\hbar\omega$ percentages of the 0^+ wave functions do not sum to 100%.
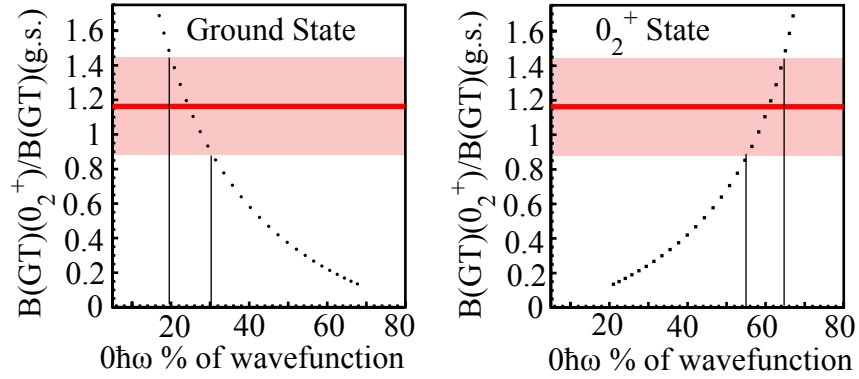
Figure 6.7: Ratio of 0_2^+ to 0_1^+ B(GT) values, plotted as a function of the percentage of the ground (left) and excited (right) state wavefunction that consist of $0\hbar\omega$ configurations. The red line indicates the B(GT) ratio found in the current work; the red shaded area is the error associated with this value.
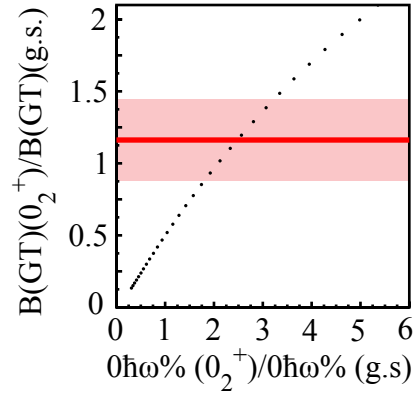
Figure 6.8: Ratio of 0_2^+ to 0_1^+ B(GT) values, plotted as a function of the ratio of $0\hbar\omega$ wavefunction percentage between the two states. The red line indicates the B(GT) ratio found in the current work; the red shaded area is the error associated with this value.

6.4   Discussion

The $0\hbar\omega$ wavefunction percentages obtained in the current work are compared with those extracted from neutron knockout [62, 64] and (d,p) transfer [71] measurements in Table 6.5. Also included in Table 6.5 are the predictions of Barker [68], Fortune and Sherr [69], and Romero-Redondo *et. al* [70]. The differences between these measurements and models was discussed in detail in Chapter 2. The current study predicts $0\hbar\omega$ contributions to the ground and 2.24 MeV 0_2^+ states that are generally consistent with previous measurements and models, with the exception of the recent (d,p) transfer study and the predictions of Barker, both of which under-predict the $0\hbar\omega$ component of the 0_2^+ state wavefunction. The transfer result given is an upper limit for the $0\hbar\omega$ contribution - since the measurement was only sensitive to $(0s)(0p)^6(1s)^2$ component, the exact contribution from other $2\hbar\omega$ configurations is unknown.

One major difference in the current measurement is that the $0\hbar\omega$ fraction of the 0_1^+ and 0_2^+ state's wavefunctions do not sum to 100%. This suggests that models which deduce the configuration of the 0_2^+ state based on the assumption that the 0_2^+ and 0_1^+ state (or vice-versa) should sum to 100% of the $0\hbar\omega$ component are may be relying on flawed assumptions. Nevertheless, the current measurement clearly shows the ground state wavefunction of ^{12}Be is predominantly made up of $2\hbar\omega$ configurations, and the 2.24 MeV 0_2^+ state is predominantly $0\hbar\omega$ in nature, further evidence for the breakdown of the $N = 8$ shell closure and additional fodder for the theoretical disputes of Fortune and Sherr, Barker, Romero-Redondo *et al.*, and those to come.

	^{12}Be(g.s.)	^{12}Be(0_2^+, 2.24 MeV)
Current Work	25.48±5.49	59.83±4.78
Knockout [62,64]	32	N/A
Transfer [71]	≤72	≤27
Barker [68]	31	42
Fortune and Sherr [69]	32	68
Romero-Redondo *et al* [70]	13-19	71-78

Table 6.5: Percentages of ground and excited state wavefunctions that consist of pure $0\hbar\omega$ configurations.

Chapter 7

Conclusion

7.1   Summary

The (^{7}Li, ^{7}Be) charge-exchange reaction has been employed in inverse kinematics to study the Gamow-Teller strength distribution in ^{12}Be. The only (n,p)-type charge-exchange probe currently available for use at intermediate energies with rare isotope beams, the (^{7}Li, ^{7}Be) reaction is a powerful tool, providing detailed structure information in a largely model-independent manner. It has been shown to be especially useful for examining nuclei near neutron shell closures, with the first experiment providing further evidence that the $N = 20$ shell gap is not quenched for ^{34}Si, and the most recent work illuminating the extent of quenching of the $N = 8$ shell gap in ^{12}Be.

The present work describes the second successful application of the (^{7}Li, ^{7}Be) reaction in inverse kinematics. Coupling a high-resolution magnetic spectrometer and a highly segmented germanium array, it was possible to isolate ^{12}Be particles produced in charge-exchange processes from numerous other reaction channels, and to reconstruct their exci-

tation energy and scattering angle. Angular distributions were generated and decomposed into multipole components using theoretical cross-sections produced in Distorted Wave Born Approximation (DWBA) calculations. The $\Delta L = 0$ cross-section at zero degrees was extrapolated to zero momentum transfer and used to extract Gamow-Teller strengths of transitions from the ground state of ^{12}B to the 0^+_1 (ground state) and 0^+_2 (2.24 MeV) state of ^{12}Be. This extraction was possible due to the existence of a well-established proportionality between the $\Delta L = 0$ differential cross-sections at the limit of zero momentum transfer and Gamow-Teller strength [13], calibrated model-independently using the ^{12}Be$\to^{12}$B Gamow-Teller strength from β-decay.

The extent of configuration mixing in the 0^+ states of ^{12}Be has been an open question for decades. The ratio of the Gamow-Teller strength of the 2.24 MeV 0^+_2 state to the 0^+_1 ground state was compared with shell model calculations, and was found to be very sensitive to the $0\hbar\omega$ component of the wavefunction. Exploiting this sensitivity allowed us to pin-down the $0\hbar\omega$ component of the ^{12}Be ground state to 25.48±5.49%, and deduce for the first time the $0\hbar\omega$ component of the 2.24 MeV 0^+_2 state (59.83±4.78%). Both 0^+ states had smaller $0\hbar\omega$ configuration percentages than previous neutron knockout studies had indicated [62, 64] (although they agree with our result within 2σ error limits), and neither the shell-model calculations of Barker [68], nor the Coulomb-shift model of Fortune and Sherr [69], nor the three-body model of Romero-Redondo *et. al* [70] exactly reproduce our observed wavefunctions, although the latter two are quite close.

7.2 Outlook

The future is bright for charge-exchange. In forward kinematics, NSCL continues to lead the way in new probe development, exploring heavier composite probes such as (^{10}Be, ^{10}B$+\gamma$). Similar to (^{7}Li, ^{7}Be), the (^{10}Be, ^{10}B) probe has a gamma transition (1.022 MeV, from the 0^+ state at 1.74 MeV to the 1^+ state at 0.718 MeV) that can be used to isolate non-spin-transfer ($\Delta S = 0$) transitions. This non-spin-transfer selectivity makes the (^{10}Be, ^{10}B) probe particularly useful for studying non-spin-transfer giant resonances such as the Isovector Giant Monopole Resonance (IVGMR). Such an experiment was recently proposed to the NSCL Program Advisory Committee, to run with the new gamma ray tracking system GRETINA.

In inverse kinematics, additional (^{7}Li, ^{7}Be) work has been proposed at NSCL and RIKEN, to investigate areas of the nuclear chart where configuration mixing is not well-understood (such as near shell closures and the Island of Inversion). (p, n) programs are now underway at NSCL, GSI, and RIKEN, in which low-energy recoil neutrons are used to reconstruct excitation energy spectra. These experiments employ a liquid hydrogen target, itself a significant technological achievement. Finally, in the future, a (d, ^{2}He) program in inverse kinematics may be possible using an active target Time Projection Chamber, such as the one currently being built at NSCL.

The (^{7}Li, ^{7}Be) reaction in inverse kinematics has proven useful for studying light and medium-mass nuclei, and the current work has demonstrated that for certain cases, meaningful structure information can be extracted from singles data as well as data requiring a charged particle+gamma coincidence. Despite this success, however, there is always room for improvement, including: the use of a high-efficiency gamma ray detection system (such

as CAESAR) to allow for more coincidence statistics (as high-resolution was not necessary to isolate the 429 keV ^{7}Be gamma from background); and the addition of a neutron detection array to kinematically reconstruct states beyond the neutron decay threshold in ^{12}Be. The shell-model calculations performed could benefit from the use of a more realistic interaction than the modified WBP interaction described here, perhaps a new interaction for the $0s0p1s0d$ shell, fit to data from stable and rare isotopes. If computational capacities continue to expand, in the near future it may be possible to compare these results to *ab initio* calculations as well.

For more than 40 years, nuclear scientists have been debating the extent of configuration mixing in ^{12}Be, in an attempt to understand the evolution of nuclear structure away from stability. This work brings us one step closer to that goal, quantifying the $0\hbar\omega$ component of the 0^{+} states. This may be one small piece placed into a much larger puzzle, but in general, the outlook is good for nuclear science - with new rare isotope facilities coming online and novel experimental techniques being employed everyday, we are inching ever closer to the ultimate goal: a fundamental understanding of the atomic nucleus.

BIBLIOGRAPHY

BIBLIOGRAPHY

[1] Aage Bohr and Ben R. Mottleson. *Nuclear Structure Volume I, Single Particle Motion.* W.A. Benjamin, Inc., New York, 1969.

[2] B.A. Brown, 2010. Nuclear Structure Lecture Notes for PHY-981.

[3] S. Raman, C.W. Nestor Jr., and P. Tikkanen. Transition probability from the ground to the first-excited 2^+ state of even-even nuclides. *At. Data and Nucl. Data Tables*, **78**:1–128, 2001. `http://dx.doi.org/doi:10.1006/adnd.2001.0858`.

[4] Maria Goeppert Mayer. On Closed Shells in Nuclei. II. *Phys. Rev.*, **75**:1969–1970, 1949. `http://link.aps.org/doi/10.1103/PhysRev.75.1969`.

[5] Otto Haxel, J. Hans D. Jensen, and Hans E. Suess. On the "Magic Numbers" in Nuclear Structure. *Phys. Rev.*, **75**:1766, 1949. `http://link.aps.org/doi/10.1103/PhysRev.75.1766.2`.

[6] B.A. Brown, A. Etchegoyen, W.D.M. Rae, N.S. Godwin, W.A. Richter, C.H. Zimmerman, W.E. Ormand, and J.S. Winfield. OXBASH. Report 524, MSU-NSCL, 1985.

[7] W.D.M. Rae. NuShell. `http://knollhouse.org/default.aspx`.

[8] B.A. Brown and W.D.M. Rae. NuShellX. `http://nscl.msu.edu/~brown/resources/resources.html`.

[9] Franz Osterfeld. Nuclear spin and isospin excitations. *Rev. Mod. Phys.*, 64:491–557, 1992. `http://dx.doi.org/doi:10.1103/RevModPhys.64.491`.

[10] J. Rapaport and E. Sugarbaker. Isovector Excitations in Nuclei. *Annu. Rev. Nucl. Part. Sci.*, 44:109–153, 1994. `http://dx.doi.org/doi:10.1146/annurev.ns.44.120194.000545`.

[11] J.C. Hardy and I.S. Towner. Superallowed $0^+ \rightarrow 0^+$ nuclear β decays: A new survey with precision tests of the conserved vector current hypothesis and the standard model. *Phys. Rev. C*, **79**:055502, 2009. `http://dx.doi.org/doi:10.1103/PhysRevC.79.055502`.

[12] K. Nakamura and Particle Data Group. Review of Particle Physics. *J. Phys. G*, **37**:075201, 2010. `http://dx.doi.org/doi:10.1088/0954-3899/37/7A/075021`.

[13] T.N. Taddeucci, C.A. Goulding, T.A. Carey, R.C. Byrd, C.D. Goodman, C. Gaarde, J. Larsen, D. Horen, J. Rapaport, and E. Sugarbaker. The (p,n) reaction as a probe of beta decay strength. *Nucl. Phys. A*, **469**:125–172, 1987. `http://dx.doi.org/doi:10.1016/0375-9474(87)90089-3`.

[14] G. Perdikakis, R.G.T. Zegers, Sam M. Austin, D. Bazin, C. Caesar, J.M. Deaven, A. Gade, D. Galaviz, C.J. Guess, C. Herlitzius, G.W. Hitt, M.E. Howard, R. Meharchand, S. Noji, H. Sakai, Y. Shimbara, E.E. Smith, and C. Tur. Gamow-Teller Unit Cross-Sections for $(t, {}^3\text{He})$ and $({}^3\text{He}, t)$ Reactions. *Phys. Rev. C*, 83:054614, 2011. `http://dx.doi.org/doi:PhysRevC.83.054614`.

[15] M.P. Nakada, J.D. Anderson, C.C. Gardiner, J. McClure, and C. Wong. Neutron Spectrum from $p + d$ Reaction. *Phys. Rev.*, 110:594, 1958. `http://dx.doi.org/doi:10.1103/PhysRev.110.594`.

[16] B.D. Anderson, J.N. Knudson, P.C. Tandy, J.W. Watson, R. Madey, and C.C. Foster. Observation of a $T_>$ Gamow-Teller State in ${}^{48}\text{Ca(p,n)}{}^{48}\text{Sc}$ at 160 MeV. *Phys. Rev. Lett.*, 45:699–702, 1980. `http://dx.doi.org/doi:10.1103/PhysRevLett.45.699`.

[17] D.E. Bainum, J. Rapaport, C.D. Goodman, D.J. Horen, C.C. Foster, M.B. Greenfield, and C.A. Goulding. Observation of Giant Particle-Hole Resonances in ${}^{90}\text{Zr(p,n)}{}^{90}\text{Nb}$. *Phys. Rev. Lett.*, 44:1751–1754, 1980. `http://dx.doi.org/doi:10.1103/PhysRevLett.44.1751`.

[18] D.J. Horen, C.D. Goodman, C.C. Foster, C.A. Goulding, M.B. Greenfield, J. Rapaport, D.E. Bainum, E. Sugarbaker, T.G. Masterson, F. Petrovich, and W.G. Love. Search for Isobaric Analogues in of M1 States and Giant SpinFlip Resonances in the ${}^{208}\text{Pb(p,n)}$ Reaction. *Phys. Lett.*, 95B:27–31, 1980. `http://dx.doi.org/doi:10.1016/0370-2693(80)90391-3`.

[19] D.J. Horen, C.D. Goodman, D.E. Bainum, C.C. Foster, C. Gaarde, C.A. Goulding, M.B. Greenfield, J. Rapaport, T.N. Taddeucci, E. Sugarbaker, T. Masterson, S.M. Austin, A. Galonsky, and W. Sterrenburg. Energy Systematics of the Giant Gamow-Teller Resonances and a Charge-Exchange Dipole Spin-Flip Resonance. *Phys. Lett.*, 99B:383–386, 1981. `http://dx.doi.org/doi:10.1016/0370-2693(81)90553-0`.

[20] C. Gaarde, J. Rapaport, T.N. Taddeucci, C.D. Goodman, C.C. Foster, D.E. Bainum, C.A. Goulding, M.B. Greenfield, D.J. Horen, and E. Sugarbaker. Excitation of Giant Spin-Isospin Multipole Vibrations. *Nucl. Phys. A*, 369:258–280, 1981. `http://dx.doi.org/doi:10.1016/0375-9474(81)90019-1`.

[21] W.P. Alford, R.L. Helmer, R. Abegg, A. Celler, O. Häusser, K. Hicks, K.P. Jackson, C.A. Miller, S. Yen, R.E. Axuma, D. Frekers, R.S. Henderson, H. Baer, and C.D. Zafiratos. Ratio of the Isovector Effective Interaction Strengths $|J_{\sigma\tau}/J_\tau|^2$ Between 200 and 450 MeV from the ^{14}C(p,n)^{14}N Reaction. *Phys. Lett. B*, 179:20–24, 1986. `http://dx.doi.org/doi:10.1016/0370-2693(86)90428-4`.

[22] N.S.P. King, P.W. Lisowski, G.L. Morgan, P.N. Craig, R.G. Jeppensen, D.A. Lind, J.R. Shepard, J.L. Ullmann, C.D. Zafiratos, C. D. Goodman, and C.A. Goulding. Observation of Fermi and Gamow-Teller Strength in the 800 MeV(p,n) Reaction. *Phys. Lett. B*, 175:279–283, 1986. `http://dx.doi.org/doi:10.1016/0370-2693(86)90856-7`.

[23] W.G. Love and M.A. Franey. Effective nucleon-nucleon interaction for scattering at intermediate energies. *Phys. Rev. C*, **24**:1073–1094, 1981. `http://dx.doi.org/doi:10.1103/PhysRevC.24.1073`.

[24] M.A. Franey and W.G. Love. Nucleon-nucleon t-matrix interaction for scattering at intermediate energies. *Phys. Rev. C*, **31**:488–498, 1985. `http://dx.doi.org/doi:10.1103/PhysRevC.31.488`.

[25] K. Ikeda, S. Fujii, and J.I. Fujita. The (p,n) reactions and beta decays. *Phys. Lett.*, 3:271–272, 1963. `http://dx.doi.org/doi:10.1016/0031-9163(63)90255-5`.

[26] C.D. Goodman, C.A. Goulding, M.B. Greenfield, J. Rapaport, D. E. Bainum, C.C. Foster, W.G. Love, and F. Petrovich. Gamow-Teller Matrix Elements from 0deg(p,n) Cross Sections. *Phys. Rev. Lett.*, 44:1755–1759, 1980. `http://dx.doi.org/doi:10.1103/PhysRevLett.44.1755`.

[27] E.R. Flynn and J.D. Garrett. Excitation of the Parent Analogs of the ^{58}Ni Giant M1 Resonance by the Reaction ^{58}Ni(t,h)^{58}Co. *Phys. Rev. Lett.*, 29:1748–1781, 1972. `http://dx.doi.org/doi:10.1103/PhysRevLett.29.1748`.

[28] F.P. Brady, C.M. Castaneda, G.A. Needham, J.L. Ullmann, J.L. Romero, N.S.P. King, C.M. Morris, F. Petrovich, and R.H. Howell. Isovector and Gamow-Teller Strength from Small-Angle (n,p) Reactions at 60 MeV. *Phys. Rev. Lett.*, 48:860–863, 1982. `http://dx.doi.org/doi:10.1103/PhysRevLett.48.860`.

[29] K.P. Jackson, A. Celler, W.P. Alford, K. Raywood, R. Abegg, R.E. Azuma, C.K. Campbell, S. El-Kateb, D. Frekers, P.W. Green, O. Häusser, R. L. Helmer, R.S. Henderson, K.H. Hicks, R. Jeppesen, P. Lewis, C.A. Miller, A. Moalem, M.A. Moinester, R.B. Schubank, G.G. Shute, B.M. Spicer, M.C. Vetterli, A.I. Yavin, and S.Yen. The (n,p) Reaction as a Probe of Gamow-Teller Strength. *Phys. Lett. B*, 201:25–28, 1988. `http://dx.doi.org/doi:10.1016/0370-2693(88)90073-1`.

[30] S. Nakayama, T. Yamagata, K. Yuasa, M. Tanaka, M. Inoue, T. Itahashi, and H. Ogata. Excitation of isovector giant resonances in ^{27}Al by heavy ion charge-exchange reaction. *Phys. Rev. C*, 34:366–369, 1986. `http://dx.doi.org/doi:10.1016/0370-2693(88)90073-1`.

[31] H. Okamura, S. Fujita, Y. Hara, K. Hatanaa, T. Ichihara, S. Ishida, K. Katoh, T. Niizeki, H. ohnuma, H. Otsu, H. Sakai, N. Sakamoto, Y. Satou, T. Uesaka, T. Wakasa, and T. Yamashita. Tensor analyzing power of the (d, ^{2}He) reaction at 270 MeV. *Phys. Lett. B*, 345:1–5, 1995. `http://dx.doi.org/doi:10.1016/0370-2693(94)01607-E`.

[32] H.M. Xu, C.A. Gagliardi, G.K. Ajupova, B. Kokenge, and Y.W. Lui. Gamow-Teller strength of ^{26}Mg. *Phys. Rev. C*, 54:3266–3269, 1996. `http://dx.doi.org/doi:10.1103/PhysRevC.54.3266`.

[33] S. Rakers, F. Ellinghaus, R. Bassini, C. Bäumer, A.M. van den Berg, D. Frekers, D. De Frenne, M. Hagemann, V.M. Hannen, M.N. Harakeh, M. Hartig, R. Henderson, J. Heyse, M.A. de Huu, E. Jacobs, M. Mielke, J.M. Schippers, R. Schmidt, S.Y. van der Werf, and H.J. Wörtche. Measuring the (d,^{2}He) reaction with the focal-plane detection system of the BBS magnetic spectrometer at AGOR. *Nucl. Instr. and Meth. A*, 481:253–261, 2002. `http://dx.doi.org/doi:10.1016/S0168-9002(01)01365-1`.

[34] J. Jänecke, K. Pham, D.A. Roberts, D. Stewart, M.N. Harakeh, G.P.A. Berg, C.C. Foster, J.E. Lisantti, R. Sawafta, E.J. Stephenson, A.M. van den Berg, S.Y. van der Werf, S.E. Muraviev, and M.H. Urin. Fragmentation of Gamow-Teller strength observed in ^{117,120}Sn(^{3}He, t)^{117,120}Sb charge-exchange reactions. *Phys. Rev. C*, 48:2828–2839, 1993. `http://dx.doi.org/doi:10.1103/PhysRevC.48.2828`.

[35] H. Akimune, I. Daito, Y. Fujita, M. Fujiwara, M.B. Greenfield, M.N. Harakeh, T. Inomata, J. Jänece, K. Katori, S. Nakayama, H. Sakai, Y. Sakemi, M. Tanaka, and M. Yosoi. (^{3}He, t) Charge-Exchange Reactions at E(^{3}He)=450 MeV, θ=0deg.

Nucl. Phys. A, 569:245–254, 1994. `http://dx.doi.org/doi:10.1016/0375-9474(94)90115-5`.

[36] R.G.T. Zegers, A.M. van den Berg, S. Brandenburg, F.R. R. Fleurot, M. Fujiwara, J. Guillot, V.M. Hannen, M.N. Harakeh, H. Laurent, K. van der Schaf, S.Y. van der Werf, A. Willis, and H.W. Wilschut. Search for Isovector Giant Monopole Resonances via the Pb(^{3}He, tp) Reaction. *Phys. Rev. Lett.*, 84:3779–3882, 2000. `http://dx.doi.org/doi:10.1103/PhysRevLett.84.3779`.

[37] N. Anantaraman, J.S. Winfield, Sam M. Austin, J.A. Carr, C. Djalali, A. Gillibert, W. Mittig, J.A. Nolen, and Zhan Wen Long. (^{12}C, ^{12}B) and (^{12}C, ^{12}N) reactions at E/A=70 MeV as spin probes: Calibration and application to 1^+ states in^{56}Mg. *Phys. Rev. C*, 44:398–414, 1991. `http://dx.doi.org/doi:10.1103/PhysRevC.44.398`.

[38] C. Bèrat, M. Buènard, J.Y. Hostachy, P. Martin, J. Barrette, B. Berthier, B. Fernandez, A. Miczaïka, A. Villari, H. G. Bohlen, S. Kubono, E. Stiliaris, and W. von Oertzen. Electric isovector nuclear response from ^{13}C induced charge-exchange reactions. *Nucl. Phys. A*, 555:455–476, 1993. `http://dx.doi.org/doi:10.1016/0375-9474(93)90296-A`.

[39] T. Ichihara, M. Ishihara, H. Ohnuma, T. Niizeki, Y. Satou, H. Okamura, S. Kubono, M.H. Tanaka, and Y. Fuchi. Isovector Quadrupole Resonance Observed in the ^{60}Ni(^{13}C, ^{13}N)^{60}Co Reaction at E/A=100 MeV. *Phys. Rev. Lett.*, 89:142501, 2002. `http://dx.doi.org/doi:10.1103/PhysRevLett.89.142501`.

[40] I. Lhenry. Decay of the Isovector Giant Resonances excited in Charge Exchange Reactions. *Nucl. Phys. A*, 599:245–258, 1996. `http://dx.doi.org/doi:10.1016/0375-9474(96)00066-8`.

[41] R.G.T Zegers, R. Meharchand, Y. Shimbara, Sam M. Austin, D. Bazin, B.A. Brown, C. Aa. Diget, A. Gade, C. J. Guess, M. Hausmann, G.W. Hitt, M.E. Howard, M. King, D. Miller, S. Noji, A. Signoracci, K. Starosta, C. Tur, C. Vaman, P. Voss, D. Weisshaar, and J. Yurkon. ^{34}P(^{7}Li, ^{7}Be $+\gamma$) Reaction at 100A MeV in Inverse Kinematics . *Phys. Rev. Lett.*, **104**:212504, 2010. `http://dx.doi.org/10.1103/PhysRevLett.104.212504`.

[42] J. Cook, K.W. Kemper, P.V. Drumm, L.K. Fifield, M.A.C. Hotchkis, T.R. Ophel, and C.L. Woods. ^{16}O(^{7}Li, ^{7}Be)^{16}N reaction at 50 MeV. *Phys. Rev. C*, **30**:1538, 1984. `http://dx.doi.org/doi:10.1103/PhysRevC.30.1538`.

[43] A. Etchegoyen, M.C. Etchegoyen, E.D Izquierdo, D. Abriola, D.E. DiGregorio, J.O. Fernandez Niello, A.M.J. Ferrero, S. Gil, A.O. Macchiavelli, A.J. Pacheco, and

J.E. Testoni. ^{10}B(^{7}Li, ^{7}Be)^{10}Be charge-exchange reaction. *Phys. Rev. C*, **38**:2124–2133, 1988. `http://dx.doi.org/doi:10.1103/PhysRevC.38.2124`.

[44] J.S. Winfield, D. Beaumel, S. Galés, H. Laurent, I. Lhenry, J.M. Maison, G.M. Grawley, S. Danczyk, S.E.Hirzebruch, J.C. Staško, and t. Suomijärvi. The (^{7}Li, ^{7}Be) reaction and isovector spin strength in^{40}Ca. *Phys. Rev. C*, **54**:125–131, 1996. `http://dx.doi.org/doi:10.1103/PhysRevC.54.125`.

[45] T. Annakkage, J. Jänecke, J.S. Winfield, G.P.A. Berg, J.A. Brown, G. Crawley, S. Danczyk, M. Fujiwara, D.J. Mercer, K.Pham, D.A. Roberts, J. Stasko, and G.H. Yoo. Isovector giant resonances in ^{6}He, ^{12}B, ^{90}Y, ^{120}In, and ^{208}Tl observed in the (^{7}Li, ^{7}Be) charge-exchange reaction. *Nucl. Phys. A*, **648**:3–44, 1999. `http://dx.doi.org/doi:10.1016/S0375-9474(99)00015-9`.

[46] S. Nakayama, H. Akimune, I. Daito, H. Fujimura, Y. Fujita, M. Fujiwara, K. Fushimi, T. Inomata, K. Ishibashi, H. Kohri, N. Koori, K. Takahisa, A. Tamii, M. Tanaka, H. Toyokawa, and T. Yamagata. Gamow-Teller transitions in the (^{7}Li, ^{7}Be) reaction at 65 AMeV. *Phys. Rev. C*, **50**:047303, 1999. `http://dx.doi.org/doi:10.1103/PhysRevC.60.047303`.

[47] Angelo Signoracci. *Effective Interactions for Nuclear Structure Calculations*. PhD thesis, Michigan State University, 2011.

[48] Angelo Signoracci and B. Alex Brown. Proton single-particle energies in ^{23}F. *Phys. Rev. C*, **75**:024303, 2007. `http://dx.doi.org/doi:10.1103/PhysRevC.75.024303`.

[49] Takaharu Otsuka, Rintaro Fujimoto, Yutaka Utsuno, B. Alex Brown, Michio Honma, and Takahiro Mizusaki. Magic Numbers in Exotic Nuclei and Spin-Isospin Properties of the NN Interaction. *Phys. Rev. Lett.*, **87**:082502, 2001. `http://dx.doi.org/doi:10.1103/PhysRevLett.87.082502`.

[50] T. Otsuka, T. Suzuki, R. Fujimoto, H. Grawe, and Y. Akaishi. Evolution of nuclear shells due to the tensor force. *Phys. Rev. Lett.*, **95**:232502, 2005. `http://dx.doi.org/doi:10.1103/PhysRevLett.95.232052`.

[51] I. Talmi and I. Unna. Order of levels in the shell model and spin of ^{11}Be. *Phys. Rev. Lett.*, **4**:469–470, 1960. `http://dx.doi.org/doi:10.1103/PhysRevLett.4.469`.

[52] H. Sagawa, B.A. Brown, and H. Esbensen. Parity inversion in the N=7 isotones and the pairing blocking effect. *Phys. Lett. B*, **309**:1–4, 1993. `http://dx.doi.org/doi:10.1016/0370-2693(93)91493-7`.

[53] A.M. Poskanzer, P.L. Reeder, and I. Dostrovsky. New Delayed-Neutron-Emitting Isotope: ^{12}Be. *Phys. Rev.*, **138**:18–20, 1965. `http://dx.doi.org/doi:10.1103/PhysRev.138.B18`.

[54] F.C. Barker. T=2 states of the A=12 nuclei. *J. Phys. G*, **2**:45–49, 1976. `http://dx.doi.org/doi:10.1088/0305-4616/2/4/001`.

[55] D.E. Alburger, D.P. Balamuth, J.M. Lind, L. Mulligan, Jr. K.C. Young, R.W. Zurmühle, and R. Middleton. Core excited T=2 levels in A=12 from studies of ^{12}Be. *Phys. Rev. C*, **17**:1525–1530, 1978. `http://dx.doi.org/doi:10.1103/PhysRevC.17.1525`.

[56] M. Bernas, J.C. Peng, and Nelson Stein. ^{12}Be levels studied with the ^{14}C(^{14}C, ^{12}Be)^{16}O Reaction. *Phys. Lett. B*, **116**:7–10, 1982. `http://dx.doi.org/doi:10.1016/0370-2693(82)90023-5`.

[57] H. Iwasaki, T. Motobayashi, H. Akiyoshi, Y. Ando, N. Fukada, H. Fujiwara, Zs. Fülöp, K.I. Hahn, Y. Higurashi, M. Hirai, I. Hisanaga, N. Iwasa, T. Kijima, A. Mengoni, T. Minemura, T. Nakamura, M. Notani, S. Ozawa, H. Sagawa, H. Sakurai, S. Shimoura, S. Takeuchi, t. Teranishi, Y. Yanagisawa, and M. Ishihara. Low-lying intruder 1^- state in ^{12}Be and the melting of the $N = 8$ shell closure. *Phys. Lett. B*, **491**:8–14, 2000. `http://dx.doi.org/doi:10.1016/S0370-2693(00)01017-0`.

[58] H.T. Fortune, G.-B. Liu, and D.E. Alburger. $(sd)^2$ states in ^{12}Be. *Phys. Rev. C*, **50**:1355–1359, 1994. `http://dx.doi.org/doi:10.1103/PhysRevC.50.1355`.

[59] F.M. Nunes, J.A. Christley, I.J. Thompson, R.C. Johnson, and V.D. Efros. Core excitation in three-body systems: Application to ^{12}Be. *Nucl. Phys. A*, **609**:43–73, 1996. `http://dx.doi.org/doi:10.1016/0375-9474(96)00284-9`.

[60] Toshio Suzuki and Takaharu Otsuka. Gamow-Teller transitions from ^{11}Li and ^{12}Be. *Phys. Rev. C*, **56**:847–856, 1997. `http://dx.doi.org/doi:10.1103/PhysRevC.56.847`.

[61] H. Iwasaki, T. Motobayashi, H. Akiyoshi, Y. Ando, N. Fukada, H. Fujiwara, Zs. Fülöp, K.I. Hahn, Y. Higurashi, M. Hirai, I. Hisanaga, N. Iwasa, T. Kijima, T. Minemura, T. Nakamura, M. Notani, S. Ozawa, H. Sakurai, S. Shimoura, S. Takeuchi, T. Teranishi, Y. Yanagisawa, and M. Ishihara. Quadrupole deformation of ^{12}Be studied by proton inelastic scattering. *Phys. Lett. B*, **481**:7–13, 2000. `http://dx.doi.org/doi:10.1016/S0370-2693(00)00428-7`.

[62] A. Navin, D.W. Anthony, T. Aumann, T. Baumann, D. Bazin, Y. Blumenfeld, B.A. Brown, T. Glasmacher, P.G. Hansen, R.W. Ibbotson, P.A. Lofy, V. Maddalena, K. Miller, T. Nakamura, B.V. Pritychenko, B.M. Sherrill, E. Spears, M. Steiner, J.A. Tostevin, J. Yurkon, and A. Wagner. Direct Evidence for the Breakdown of the N=8 Shell Closure in ^{12}Be. *Phys. Rev. Lett.*, **85**:266–269, 2000. `http://dx.doi.org/doi:10.1103/PhysRevLett.85.266`.

[63] F.M. Nunes, I.J. Thompson, and J.A. Tostevin. Core excitation in ^{12}Be. *Nucl. Phys. A*, **703**:593–602, 2002. `http://dx.doi.org/doi:10.1016/S0375-9474(01)01667-0`.

[64] S.D. Pain, W.N. Catford, N.A. Orr, J.C. Angèlique, N.I. Ashwood, V. Bouchat, N.M. Clarke, N. Curtis, M. Freer, B.R. Fulton, F. Hanappe, M. Labiche, J.L. Lecouey, R.C. Lemmon, D. Mahboub, A. Ninane, G. Normand, N. Soić, L. Stuttge, C.N. Timis, J.A. Tostevin, J.S. Winfield, and V. Ziman. Structure of ^{12}Be: Intruder *d*-Wave Strength at $N = 8$. *Phys. Rev. Lett.*, **96**:032502, 2006. `http://dx.doi.org/doi:10.1103/PhysRevLett.96.032502`.

[65] S. Shimoura, A. Saito, T. Minemura, Y.U. Matsuyama, H. Baba, H. Akiyoshi, N. Aoi, T. Gomi, Y. Higurashi, K. Ieki, N. Imai, N. Iwasa, H. Iwasaki, S. Kanno, S. Kubono, M. Kunibu, S. Michimasa, T. Motobayashi, T. Nakamura, H. Sakurai, M. Serata, E. takeshita, S. takeuchi, T. Teranishi, K. Ue, K. Yamada, Y. Yanagisawa, M. Ishihara, and N. Itagaki. Isomeric 0^+ state in ^{12}Be. *Phys. Lett. B*, **560**:31–36, 2003. `http://dx.doi.org/doi:10.1016/S0370-2693(03)00341-1`.

[66] R. Sherr and H.T. Fortune. Structure of ^{12}Be and ^{12}O ground states. *Phys. Rev. C*, **60**:064323, 1999. `http://dx.doi.org/doi:10.1103/PhysRevC.60.064323`.

[67] H.T. Fortune and R. Sherr. Excited 0^+, T=2 states in ^{12}Be, ^{12}C, ^{12}O. *Phys. Rev. C*, **74**:024301, 2006. `http://dx.doi.org/doi:10.1103/PhysRevC.74.024301`.

[68] F.C. Barker. Comment on Èxcited 0^+, T=2 states in ^{12}Be, ^{12}C, ^{12}O'. *J. Phys. G*, **36**:038001, 2009. `http://dx.doi.org/doi:10.1088/0954-3899/36/3/038001`.

[69] H.T. Fortune and R. Sherr. Reply to Comment on Excited 0^+, T=2 states in ^{12}Be, ^{12}C, ^{12}O'. *J. Phys. G*, **36**:038002, 2009. `http://dx.doi.org/doi:10.1088/0954-3899/36/3/038002`.

[70] C. Romero-Redondo, E. Garrido, D.V. Fedorov, and A.S. Jensen. Three-body structure of low-lying ^{12}Be states. *Phys. Rev. C*, **77**:054313, 2008. `http://dx.doi.org/doi:10.1103/PhysRevC.77.054313`.

[71] R. Kanungo, A.T. Gallant, M. Uchida, C. Andreoiu, R.A. E. Austin, D. Bandyopadhyay, G.C. Ball, J.A. Becker, A.J. Boston, H.C. Boston, B.A. Brown, L. Buchmann, S.J. Colosimo, R.M. Clark, D. Cline, D.S Cross, H. Dare, B. Davids, T.E. Drake, M. Djongolov, P. Finlay, N. Galinski, P.E. Garrett, A.B. Garnsworth, K.L. Green, S. Grist, G. Hackman, L.J. Harkness, A.B. Hayes, D. Howell, A.M. Hurst, H.B. Jeppesen, K.G. Leach, A.O. Macchiavelli, D. Oxley, C.J. Pearson, B. Pietras, A.A. Phillips, S.V. Rigby, C. Ruiz, G. Ruprecht, F. Sarazin, M.A. Schmaker, A.C. Shotter, C.S. Sumitharachichi, C.E. Svensson, I. Tanihata, S. Triambak, C. Unsworth, S.J. Williams, P. Walden, J. Wong, and C.Y. Wu. Structure of states in ^{12}Be via the ^{11}Be(d,p) reaction. *Phys. Lett. B*, **682**:391–395, 2010. `http://dx.doi.org/doi:10.1016/j.physletb.2009.11.025`.

[72] H.T. Fortune and R. Sherr. Structure of 2^{+}, T=2 states in A=12 nuclei. *Phys. Rev. C*, **83**:044313, 2011. `http://dx.doi.org/doi:10.1103/PhysRevC.83.044313`.

[73] E.K. Warburton and B.A. Brown. Effective interactions for the 0p1s0d nuclear shell-model space. *Phys. Rev. C*, **46**:923–944, 1992. `http://dx.doi.org/doi:10.1103/PhysRevC.46.923`.

[74] E.K. Warburton, B.A. Brown, and D.J. Millener. Large-basis shell-model treatment of A=16. *Phys. Lett. B*, **293**:7–12, 1992. `http://dx.doi.org/doi:10.1016/0370-2693(92)91472-L`.

[75] C.J. Guess, R.G.T. Zegers, B.A. Brown, Sam M. Austin, D. Bazin, C. Caesar, J.M. Deaven, G.F. Grinyer, C. Herlitzius, G.W. Hitt, S. Noji, R. Meharchand, G. Perdikakis, H. Sakai, Y. Shimbara, and C. Tur. Spectroscopy of ^{13}B via the ^{13}C$(t, ^{3}$He$)$ reaction at $115A$ MeV. *Phys. Rev. C*, **80**:024305, 2009. `http://dx.doi.org/doi:10.1103/PhysRevC.80.024305`.

[76] W.-T. Chou, E.K. Warburton, and B.A. Brown. Gamow-Teller beta-decay rates for A$\leqq$18 nuclei. *Phys. Rev. C*, **47**:163–177, 1993. `http://dx.doi.org/doi:10.1103/PhysRevC.47.163`.

[77] Ian J. Thompson and Filomena M. Nunes. *Nuclear Reactions for Astrophysics*. Cambridge University Press, New York, 2009.

[78] J.J. Sakurai. *Modern Quantum Mechanics Revised Edition*. Addison-Wesley, New York, 1994.

[79] J. Cook and J. Carr. Computer program FOLD. Florida State University (unpublished); based on F. Petrovich and D. Stanley, *Nucl. Phys. A* 275:487, 1977; modified

as described in J. Cook *et al.*, *Phys. Rev. C* 30:1538, 1984; R.G.T. Zegers (2005), unpublished.

[80] B.A. Brown. New Skyrme interaction for normal and exotic nuclei. *Phys. Rev. C*, **58**:220–231, 1998. `http://dx.doi.org/doi:10.1103/PhysRevC.58.220`.

[81] S. Cohen and D. Kurath. Effective interactions for the 1p shell. *Nucl. Phys.*, **73**:1–24, 1965. `http://dx.doi.org/doi:10.1016/0029-5582(65)90148-3`.

[82] J.Jänecke, T. Annakage, G.P.A. Berg, B.A. Brown, J.A. Brown, G. Crawley, S. Danczyk, M. Fujiwara, D.J. Mercer, K. Pham, D.A. Roberts, J. Stasko, J.S. Winfield, and G.H. Yoo. Study of the neutron-halo nucleus ^{6}He. *Phys. Rev. C*, **54**:1070–1083, 1996. `http://dx.doi.org/doi:10.1103/PhysRevC.54.1070`.

[83] A. Nadasen, J. Brusoe, J. Farhat, T. Stevens, J. Williams, L. Nieman, J.S. Winfield, R.E. Warner, F.D. Becchetti, J.W. Jänecke, T. Annakkage, J. Bajema, D. Roberts, and H.S. Govinden. Unique potentials for the elastic scattering of 350 MeV ^{7}Li from ^{12}C and ^{28}Si. *Phys. Rev. C*, **52**:1894–1899, 1995. `http://dx.doi.org/doi:10.1103/PhysRevC.52.1894`.

[84] A. Negret, T. Adachi, B.R. Barrett, C. Bäumer, A.M. van den Berg, G.P.A. Berg, P. von Brentano, D. Frekers, D. De Frenne, H. Fujita, K. Fujita, Y. Fujita, E.W. Grewe, P. Haefner, M.N. Harakeh, K. Hatanaka, K. Heyde, M. Hunyadi, E. Jacobs, Y. Kalmykov, A. Korff, K. Nakanishi, P. Navrátil, P. von Neumann-Cosel, L. Popescu, S. Rakers, A. Richter, N. Ryezayeva, Y. Sakemi, A. Shevchenko, Y. Shimbara, Y. Shimizu, Y. Tameshige, A. Tamii, M. Uchida, J. Vary, H.J. Wörtche, M. Yosoi, and L. Zamick. Gamow-Teller Strengths in the A=14 Multiplet: A Challenge to the Shell Model. *Phys. Rev. Lett.*, **97**:062502, 2006. `http://dx.doi.org/doi:10.1103/PhysRevC.97.062502`.

[85] P. A. Záavodszky, B. Arend, D. Cole, J. DeKamp, , M. Doleans, G. Machicoane, F. Marti, P. Miller, J. Moskalik, W. Nurnberger, J. Ottarson, J. Vincent, X. Wu, and A. Zeller. Design, construction and first commissioning results of superconducting source for ions at NSCL/MSU. *Rev. Sci. Instrum.*, **79**:02A302 1–4, 2008. `http://dx.doi.org/10.1063/1.2804863`.

[86] X. Wu, H. Blosser, D. Johnson, F. Marti, and R. C. York. The K500-to-K1200 Coupling Line for the Coupled Cyclotron Facility at the NSCL. In *Proceedings of the 1999 Particle Accelerator Conference, PAC99*, 2007. `http://cdsweb.cern.ch/record/553461/files/tua104.pdf`.

[87] W. Loveland, D. J. Morrissey, and G. T. Seaborg. *Modern Nuclear Chemistry.* John Wiley & Sons, New Jersey, 2006.

[88] D. J. Morrissey, B. M. Sherrill, M. Steiner, A. Stolz, and I Wiedenhöver. Commissioning the A1900 projectile fragment separator. *Nucl. Instr. and Meth. B*, **204**:90–96, 2003. `http://dx.doi.org/10.1016/S0168-583X(02)01895-5`.

[89] Glenn F. Knoll. *Radiation Detection and Measurement.* John Wiley & Sons, New York, 2000.

[90] D. Bazin, J.A. Caggiano, B.M Sherrill, J. Yurkon, and A. Zeller. The S800 Spectrograph. *Nucl. Instr. and Meth. B*, **204**:629–633, 2003. `http://dx.doi.org/10.1016/S0168-583X(02)02142-0`.

[91] W.F. Mueller, J.A. Church, T. Glasmacher, D. Gutknecht, G. Hackman, P.G. Hansen, Z. Hu, K.L. Miller, and P. Quirin. Thirty-two-fold segmented germanium detectors to identify γ-rays from intermediate-energy exotic beams. *Nucl. Instr. and Meth. A*, **466**:492–498, 2001. `http://dx.doi.org/10.1016/S0168-9002(01)00257-1`.

[92] H. Fujita, Y. Fujita, G.P.A. Berg, A.D. Bacher, C.C. Foster, K. Hara, K. Hatanaka, T.Kawabata, T. Noro, H. Sakaguchi, Y. Shimbara, T. Shinada, E.J. Stephenson, H. Ueno, and M. Yosoi. Realization of matching conditions for high-resolution spectrometers. *Nucl. Instr. and Meth. A*, **484**:17–26, 2002. `http://dx.doi.org/10.1016/S0168-9002(01)01970-2`.

[93] J. Yurkon, D. Bazin, W. Benenson, D.J. Morrissey, B.M. Sherrill, D. Swan, and R. Swanson. Focal plane detector for the S800 high-resolution spectrometer. *Nucl. Instr. and Meth. A*, **422**:291–295, 1999. `http://dx.doi.org/10.1016/S0168-9002(98)00960-7`.

[94] George Wesley Hitt. *The $^{64}Zn(t,\ ^{3}He)$ charge-exchange reaction at 115 MeV per nucleon and application to ^{64}Zn stellar electron-capture.* PhD thesis, Michigan State University, 2009.

[95] Kyoko Makino and Martin Berz. COSY INFINITY version 8. *Nucl. Instr. and Meth. A*, **427**:338–343, 1999. `http://dx.doi.org/10.1016/S0168-9002(98)01554-X`.

[96] Heather Lynn Crawford. *Evolution of Nuclear Shell Structure: β-decay and Isomeric Properties of Nuclei in and Near the fp Shell.* PhD thesis, Michigan State University, 2010.

[97] NewSpecTcl, 2009. Modified version of NSCL-designed SpecTcl, `http://docs.nscl.msu.edu/daq/spectcl/`.

[98] J. Theuerkauf, S. Esser, S. Krink, M. Luig, N. Nicolay, O. Stuch, and H. Wolters, 1993. http://www.ikp.uni-koeln.de.

[99] PAW version 2.14/04, 2004. http://paw.web.cern.ch/paw.

[100] International Atomic Energy Agency Nuclear Data Service, 2005. X-ray and Gamma-ray Decay Data Standards for Detector Calibration and Other Applications, `http://www-nds.iaea.org/xgamma_standards/genergies1.htm`.

[101] J.H. Hubbell and S.M. Seltzer. Tables of X-Ray Mass Attentuation Coefficients and Mass Energy-Absorption Coefficients (version 1.4).

[102] O.B. Tarasov and D. Bazin. LISE++: Radioactive beam production with in-flight separators. *Nucl. Instr. and Meth. B*, **266**:4657–4664, 2008. `http://dx.doi.org/doi:10.1016/j.nimb.2008.05.110`.

[103] A.H. Wapstra, G. Audi, and C. Thibault. The AME2003 atomic mass evaluation (I). Evaluation of input data, adjustment procedures. *Nucl. Phys. A*, **729**:129–336, 2003. `http://dx.doi.org/doi:10.1016/j.nuclphysa.2003.11.002`.

[104] F. Ajzenberg-Selove. Energy levels of light nuclei A=5-10. *Nucl. Phys. A*, **490**:1–225, 1988. `http://dx.doi.org/doi:10.1016/0375-9474(88)90124-8`.

[105] F. Ajzenberg-Selove. Energy levels of light nuclei A=11-12. *Nucl. Phys. A*, **506**:1–158, 1990. `http://dx.doi.org/doi:10.1016/0375-9474(90)90271-M`.